THESIS FOR THE DEGREE OF DOCTOR OF PHILOSOPHY

Investigation of a discrete ordinates method for neutron noise simulations in the frequency domain

HUAIQIAN YI

Department of Physics
CHALMERS UNIVERSITY OF TECHNOLOGY
Gothenburg, Sweden 2021

Investigation of a discrete ordinates method for neutron noise simulations in the frequency domain

HUAIQIAN YI
ISBN 978-91-7905-606-3

Doktorsavhandlingar vid Chalmers tekniska högskola
Ny serie nr 5072
ISSN 0346-718X
Technical report CTH-NT-346

Department of Physics
Chalmers University of Technology
SE-412 96 Gothenburg
Sweden
Telephone + 46 (0)31-772 1000

Cover:
Neutron noise induced by an absorber of variable strength in the C5G7 system. Simulation is performed with S16 approximation and ray effects are mitigated using a fictitious source method. First-energy group amplitude (left) and phase (right). For more information, see Section 5.4, page 51.

Chalmers Digital Print
Gothenburg, Sweden 2021

Investigation of a discrete ordinates method for neutron noise simulations in the frequency domain
HUAIQIAN YI
Division of Subatomic, High Energy and Plasma Physics
Department of Physics
Chalmers University of Technology

Abstract

During normal operations of a nuclear reactor, neutron flux measurements show small fluctuations around mean values, the so-called neutron noise. These fluctuations may be driven by a variety of perturbations, e.g., mechanical vibrations of core components. From the analysis of the neutron noise, anomalous patterns can be identified at an early stage and corrected before they escalate. For this purpose, the modelling of the reactor transfer function, which describes the core response to a possible perturbation and is based on the neutron transport equation, is often required. In this thesis a discrete ordinate method is investigated to solve the neutron noise transport equation in the frequency domain. When applying the method, two main issues need to be considered carefully, i.e., the performance of the numerical algorithm and possible numerical artifacts arising from the discretization of the equation. For an efficient numerical scheme, acceleration techniques are tested, namely, the synthetic diffusion acceleration and various forms of the coarse mesh finite difference method. To reduce the possible numerical artifacts, the impact of the order of discrete ordinates and the use of a fictitious source method are studied. These analyses serve to develop the higher-order neutron noise solver NOISE-SN. The solver is compared with different solvers and used to simulate neutron noise experiments carried out in the research reactor CROCUS (at EPFL). The solver NOISE-SN is shown to provide results that are consistent with the results obtained from other higher-order codes and can reproduce features observed in neutron noise experiments.

Keywords: Neutron noise, Deterministic neutron transport, Discrete ordinates method, Numerical acceleration, Ray effects

List of Publications

Papers included in the thesis:

PAPER I

H. Yi, P. Vinai, and C. Demazière, "On the simulation of neutron noise using a discrete ordinates method," *Annals of Nuclear Energy*, Volume 164, 15 December 2021, 108570. https://doi.org/10.1016/j.anucene.2021.108570

PAPER II

P. Vinai, H. Yi, A. Mylonakis, C. Demazière, B. Gasse, A. Rouchon, A. Zoia, A. Vidal-Ferràndiz, D. Ginestar, G. Verdú, and T. Yamamoto, "Comparison of neutron noise solvers based on numerical benchmarks in a 2-D simplified UOX fuel assembly," International Conference on Mathematics and Computational Methods Applied to Nuclear Science and Engineering – M&C 2021.

PAPER III

H. Yi, P. Vinai, and C. Demazière, "Acceleration of a 2-dimensional, 2-energy group neutron noise solver based on a discrete ordinates method in the frequency domain", PHYSOR2020 – International Conference on Physics of Reactors: Transition to a Scalable Nuclear Future, EPJ Web Conf., Volume 247, 2021. https://doi.org/10.1051/epjconf/202124721005

PAPER IV

H. Yi, P. Vinai, and C. Demazière, "A discrete ordinates solver with diffusion synthetic acceleration for simulations of 2-D and 2-energy group neutron noise problems," International Conference on Mathematics and Computational Methods applied to Nuclear Science and Engineering, M&C 2019, Portland, Oregon USA, August 25-29, 2019. https://doi.org/10.5281/zenodo.3567612

PAPER V

A. Mylonakis, H. Yi, P. Vinai and C. Demazière, "Neutron noise simulations in a heterogeneous system: A comparison between a diffusion-based and a discrete ordinates solver," International Conference on Mathematics and Computational Methods applied to Nuclear Science and Engineering, M&C 2019, Portland, Oregon USA, August 25-29, 2019. https://doi.org/10.5281/zenodo.3567577

The author’s contribution to the included papers:

PAPER I: Huaiqian Yi (HY) developed the discrete ordinates neutron noise solver NOISE-SN, performed the simulation work regarding the mitigation of ray effects, interpreted the results, and wrote the paper together with the co-authors.

PAPER II: HY developed the model for the discrete ordinates solver and performed the simulations with the solver, prepared the plots about the comparison between the different simulators, contributed to the interpretation of the results, and was involved in the review of the paper.

PAPER III: HY developed the discrete ordinates solver, performed the simulation work for the comparison of different acceleration methods, interpreted the results, and wrote the paper together with the co-authors.

PAPER IV: HY developed the discrete ordinates solver, performed the theoretical and the simulation work for the convergence analysis of the solver, interpreted the results, and wrote the paper together with the co-authors.

PAPER V: HY developed the model for the discrete ordinates solver and performed the simulations with the solver, prepared the plots about the comparison between the discrete ordinates solver and CORE SIM, contributed to the interpretation of the results, and was involved in the review of the paper.

Papers not related to the thesis subject and not included in the thesis:

H. Yi, C. Demazière, P. Vinai and J. Leppänen, “Development and Test of a Hybrid Probabilistic-Deterministic Framework Based on The Interface Current Method,” *International Conference on Mathematics and Computational Methods applied to Nuclear Science and Engineering, M&C 2019*, Portland, Oregon USA, August 25-29, 2019.

Technical reports not appended in the thesis:

P. Vinai (Chalmers), A. Brighenti (CEA), C. Demazière (Chalmers), B. Gasse (CEA), D. Ginestar (UPV), A. Mylonakis (Chalmers), A Rouchon (CEA), S.Santandrea (CEA), A. Tatidis (Chalmers), A. Vidal-Ferràndiz (UPV), G. Verdú (UPV), T. Yamamoto (KyotoU), H. Yi (Chalmers), I Zmijarevic (CEA), A. Zoia (CEA) , "CORTEX D1.4: Development and comparison of highorder solvers for reactor noise analysis," 2021.
https://cortex-h2020.eu/wp-content/uploads/2021/09/CORTEX_D1_4_Development_and_comparison_of_highorder_solvers_for_reactor_noise_analysis_V1.pdf

P. Vinai (Chalmers), K. Ambrozic (EPFL), A. Brigenti (CEA), C. Demazière (CHALMERS), B. Gasse (CEA), D. Ginestar (UPV), M. Hursin (EPFL), S. Hübner (TUD), A. Knospe (TUD), Vincent LAMIRAND (EPFL), C. Lange (TUD), A. Laureau (EPFL), R. Macian (TUM), A. Mylonakis (CHALMERS), O. Pakari (EPFL), A. Rais (EPFL), A. Rouchon (CEA), S. Santandrea (CEA), Z. Stankovski (CEA), G. Verdú (UPV), A. Vidal-Ferràndiz (UPV), T. Yamamoto (KyotoU), H. Yi (CHALMERS), S. Yum (TUM), I. Zmijarevic (CEA), A. Zoia (CEA), "CORTEX D2.5: Final validation report," 2021.
https://cortex-h2020.eu/wp-content/uploads/2021/09/CORTEX_D2_5_Final_validation_report_V1.pdf

Acknowledgements

First and foremost, I would like to express my deepest gratitude to my supervisor Assoc. Prof. Paolo Vinai for his continuous support, patience, and encouragement. His consistent and navigational guidance has been essential in every phase of the research work, and in the writing of the thesis.

I would like to thank my co-supervisor and examiner Prof. Christophe Demazière for his insightful comments and suggestions that enabled me to improve greatly my research and the thesis.

I would like to thank Dr. Antonios Mylonakis for the pleasant, friendly, and stimulating collaboration, including both technical and non-technical discussions.

Many thanks to all the partners involved in the CORTEX project for the inspiring discussions on the many aspects of neutron noise. I would like to thank in particular: the CROCUS team at EPFL for providing the COLIBRI experimental data and helping with the modelling of the CROCUS reactor; and Dr. Andrea Zoia and Dr. Amélie Rouchon at CEA for their help with the neutron noise benchmark based on the simplified UOX fuel assembly.

I would like to thank the main opponent Prof. Jean Ragusa and members of the grading committee Assoc. Prof. Danny Lathouwers, Prof. Eugene Shwageraus, Prof. Janne Wallenius, Prof. Paul Erhart, for accepting to review the thesis and participate in my doctoral defense.

The research leading to this thesis has received funding from the Euratom research and training program 2014-2018 under the grant agreement No. 754316.

Part of the computations were enabled by resources provided by the Swedish National Infrastructure for Computing (SNIC) at C3SE and at UPPMAX, partially funded by the Swedish Research Council through grant agreement no. 2018-05973.

Finally, I would like to thank my parents and my wife for their unconditional support and care throughout the years of my studies and research.

Nomenclature

$\boldsymbol{r}$	Position vector
$\boldsymbol{\Omega}$	Vector in the direction of motion
E	Neutron energy
t	General time coordinate
i	Imaginary unit
ω	Angular frequency
v	Neutron speed
Σ_t	Macroscopic total cross section
Σ_s	Macroscopic scattering cross section
Σ_f	Macroscopic fission cross section
ν	Average total fission neutron yield
χ_p	Prompt fission neutron spectrum
χ_d	Delayed fission neutron spectrum
λ	Neutron precursor decay constant
D	Neutron diffusion coefficient
ψ	Angular neutron flux
ϕ	Scalar neutron flux
$\delta\psi$	Angular neutron noise
$\delta\phi$	Scalar neutron noise
C	Concentration of neutron precursor
ρ	Reactivity
Λ	Mean neutron generation time
k_{eff}	Effective multiplication factor
g	Energy group
q	Delayed neutron precursor family

Contents

Chapter 1

Introduction

The general background and the objectives of the doctoral research are discussed together with the structure of the thesis.

1.1 Nuclear Power Reactors

Nuclear power provides around 10% of the world's electricity. Despite the disadvantages such as the production of harmful radioactive waste and the high cost for the construction of nuclear power plants, nuclear energy can facilitate the reduction of carbon dioxide emissions and contribute to an energy transition towards a more sustainable society. In fact, electricity generation from nuclear power plants is essentially free of direct greenhouse gas emissions and the indirect emissions are limited [1].

At present, most commercial reactors are Light Water Reactors (LWRs), which are further divided into Pressurized Water Reactors (PWRs) and Boiling Water Reactors (BWRs). The thermal energy is generated in the so-called reactor core via nuclear fission reactions, in which fissile atoms, e.g., of uranium-235 are split by means of neutrons. Each fission also emits new neutrons that can cause other fissions and thus a steady reaction chain can be maintained. Light water is used to remove and transport away from the core the energy released from the fissions. The light water also has the function of neutron moderator, i.e., it slows down the neutrons to increase the probability of fission events. The neutron moderation is needed because the typical nuclear fuel in these systems consists of natural uranium with a relatively low (about 3-5%) enrichment in uranium-235. In the case of PWRs, a primary cooling system, where the water is kept liquid, is used to transfer the heat from the core to steam generators in which steam is obtained for the secondary system of the plant. The steam is then sent to the turbines that are connected to an electrical generator to produce electricity. In the case of BWRs, the steam for the turbines is directly generated in the reactor core.

A commercial LWR core is loaded with hundreds of nuclear fuel assemblies, see Fig. 1.1. A fuel assembly includes fuel pins arranged in a square lattice (a typical lattice may be 17×17 for PWRs and 8×8 for BWRs). A fuel pin consists of a metal tube (the cladding, which is usually a zirconium alloy) containing pellets of nuclear fuel (e.g., uranium dioxide). The diameter of a LWR fuel pin is about 1 cm and the nuclear active length is about 3.5 meters. Control rods made of neutron absorption material can be inserted between fuel assemblies to control the neutron population in the core, and to stop the fission reactions and thus the power production.

Calculations are crucial to design and operate nuclear power plants in a safe and efficient manner. For this purpose, mathematical models and numerical methods have been developed to reproduce the reactor core behavior under a variety of conditions, with a high level of detail and accuracy. Such a task is complex since it requires the modelling of different field of physics (e.g., neutron transport and fluid dynamics) and phenomena at different spatial and time scales.

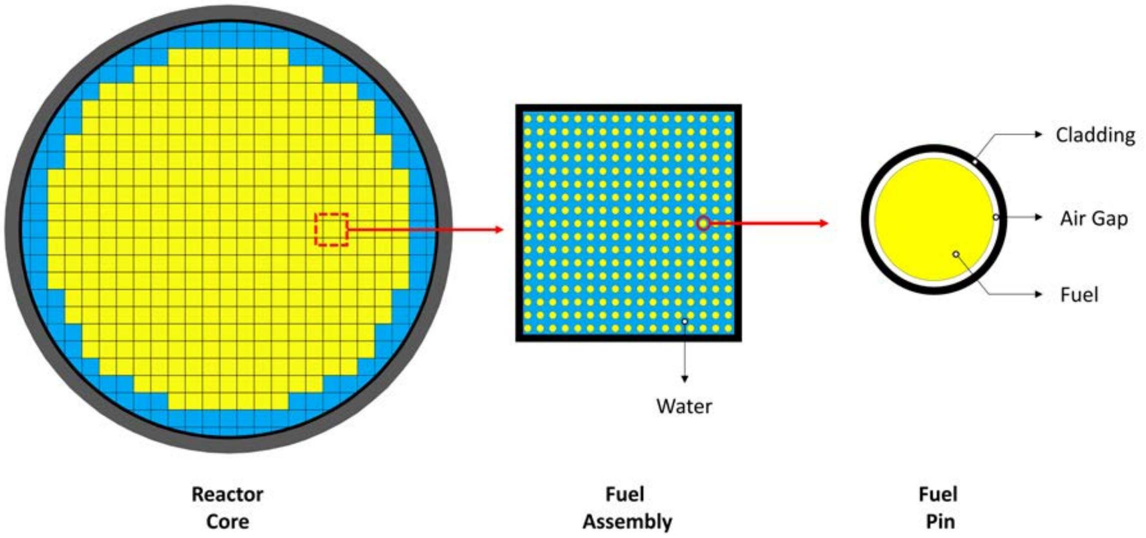

Figure 1.1 Schematic of the radial cross section of a nuclear reactor core, fuel assembly and fuel pin

1.2 Neutron noise

In nuclear power reactors, it is desired to maintain a steady operation so that a large amount of power can be produced in a stable manner. From an operational and safety viewpoint, the spatial distribution of the neutron population in the reactor and its time evolution are important to monitor since it drives the reactor power output. Therefore, nuclear reactors are equipped with detectors for neutron flux measurements.

The time-dependent signals of the neutron detectors show small fluctuations around mean values, even under normal, steady-state operation. Such fluctuations are referred to as neutron noise, and, in the case of reactors operating at a high-power level, power reactor noise.

Power reactor noise mainly arises from the perturbations in the neutron population induced by mechanical vibrations of core components and fluctuations of the properties of the coolant flow through the core. These types of phenomena need to be monitored carefully because they can escalate into more severe problems and challenge the safety of the plant. For example, vibrations of fuel assemblies and fluctuations of coolant flow (via local overheating) may lead to failures of the cladding of the fuel pins with possible leakage of radioactive material. Then the analysis of the neutron noise can provide important information about the core conditions and help to identify and localize anomalous patterns, so that appropriate actions can be taken promptly [2, 3]. The approach also has the advantage to be applicable online, without interfering with reactor operation, since it relies on neutron flux measurements using the existing instrumentation.

To retrieve an anomaly from neutron noise measurements, an inversion procedure (also denoted as unfolding procedure) is necessary [4], as shown in Fig. 1.2. Such a procedure is often based on the modelling of the reactor transfer function, which describes the response of the neutron flux in the reactor core to a perturbation, and simulations of neutron noise.

The process of using neutron noise to backtrack core perturbations is known as neutron noise diagnostics, and it has successfully been applied in the past, e.g., to study control rod vibrations [5] and core barrel vibrations [6], and to estimate in-core coolant velocity [7].

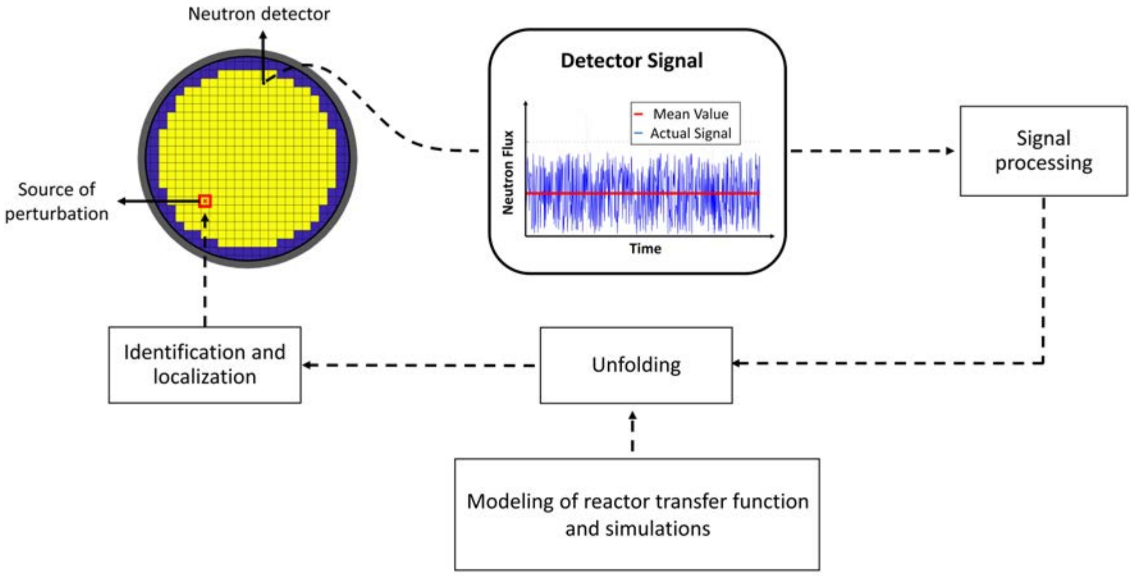

Figure 1.2 Illustration of using reactor neutron noise for core monitoring and diagnostics

1.3 Objective of the thesis

As discussed in [8], a coarser estimation of the reactor transfer function may be sufficient for reactor diagnostics, and most of the work in the field of reactor neutron noise relies on neutron diffusion theory, e.g., see [9, 10]. The advantage of this coarser modelling is that simulations of neutron noise problems in relatively large systems such as nuclear power reactors can be performed without too heavy computational efforts. Nevertheless, recent efforts also focus on higher-order deterministic [11,12] or stochastic [13, 14, 15] methods for solving the transport neutron noise equation. Although these methods are more computationally expensive, they can provide more detailed analyses and be used to assess the limitations of lower-order approximations.

The current thesis investigates a higher-order deterministic method for the simulation of neutron noise problems in the frequency domain, i.e., the discrete ordinates (S_N) method.

The discrete ordinates method has been studied for static and time-dependent reactor calculations. When it is applied, two main issues must be considered carefully. Firstly, the discrete ordinates method uses an iterative procedure for the numerical solution. This algorithm can be computationally very expensive because of the high number of iterations needed for convergence. Secondly, results obtained from the S_N method may suffer from numerical artifacts, known as ray effects. According to the S_N method, a limited, discrete number of angular directions is taken to model the neutrons travelling in the system. If the discretization with respect to the angular variable is too coarse (in relation to the spatial grid used), ray effects may arise and lead to inaccurate or even incorrect results.

In the research presented in this doctoral thesis, the two issues are addressed for the case of neutron noise calculations in the frequency domain. Therefore, acceleration methods to improve the numerical efficiency of the scheme, and ray effects together with strategies for their mitigation are analyzed. Following these studies, the neutron noise solver NOISE-SN is developed. To verify the correct implementation and explore the capability of the method, numerical benchmark problems and neutron noise experiments are simulated.

1.4 Structure of the thesis

The thesis is built from the contents of Paper I to Paper V and is structured as follows. In Chapter 2, the neutron noise equations in the frequency domain are derived and the zero-power reactor transfer function is introduced. In Chapter 3, the formulation of the S_N method and the basic calculation procedure used in NOISE-SN is described. In Chapter 4, two acceleration methods, i.e., the Diffusion Synthetic Acceleration method and the Coarse Mesh Finite Difference method, are studied for neutron noise calculations. In Chapter 5, ray effects and possible mitigation strategies are discussed. In Chapter 6, results calculated with NOISE-SN for numerical problems and neutron noise experiments are presented. In Chapter 7, the work is summarized and an outlook for future research is provided.

Chapter 2

Frequency-domain neutron noise equation and reactor transfer function

The time-dependent neutron balance equations and the static neutron transport equation are introduced in Section 2.1 and Section 2.2, respectively. The transport neutron noise equation in the frequency domain is derived in Section 2.3. The zero-power reactor transfer function is discussed in Section 2.4.

2.1 Neutron kinetics

In a nuclear reactor, neutrons induce nuclear fission reactions in the nuclear fuel that contains, for example, uranium-235. When an atom of uranium-235 undergoes fission, two fission fragments are produced and neutrons that can induce further fissions are released. A fraction of these neutrons (the prompt neutrons) is emitted immediately, while a fraction (the delayed neutrons) is emitted with a delay from the beta decay of the fission fragments (the precursors of the delayed neutrons). Therefore, the neutron population of the reactor is described by the time-dependent Boltzmann transport equation coupled to a set of equations for the precursors of delayed neutrons. The precursors of delayed neutrons are usually grouped into several families according to their decay constants, and a balance equation is given for each family. Then the neutron kinetics equations read, as:

$$\begin{aligned}
&\left[\frac{1}{v(E)}\frac{\partial}{\partial t} + \boldsymbol{\Omega}\cdot\nabla + \Sigma_t(\boldsymbol{r},E,t)\right]\psi(\boldsymbol{r},\boldsymbol{\Omega},E,t)\\
&= \int_{4\pi}\int \Sigma_s(\boldsymbol{r},E'\to E,\boldsymbol{\Omega}'\to\boldsymbol{\Omega},t)\psi(\boldsymbol{r},\boldsymbol{\Omega}',E',t)dE'\\
&+\frac{1}{4\pi k_{eff}}\left[\chi_p(\boldsymbol{r},E)\left(1-\sum_q \beta_q(\boldsymbol{r})\right)\int v\Sigma_f(\boldsymbol{r},E',t)\phi(\boldsymbol{r},E',t)dE' + \sum_q \chi_{d,q}(\boldsymbol{r},E)\lambda_q C_q(\boldsymbol{r},t)\right]
\end{aligned}\tag{2.1}$$

$$\frac{\partial C_q(\boldsymbol{r},t)}{\partial t} = \beta_q(\boldsymbol{r})\int v\Sigma_f\left(\boldsymbol{r},E',t\right)\phi\left(\boldsymbol{r},E',t\right)dE' - \lambda_q C_q(\boldsymbol{r},t) \tag{2.2}$$

Equation (2.1) describes the neutron balance through the angular neutron flux $\psi(\boldsymbol{r},\boldsymbol{\Omega},E,t)$, which depends on the space vector $\boldsymbol{r}$, the direction of neutron motion $\boldsymbol{\Omega}$, the energy E and the time t. The terms on the left-hand side of this equation represent the time variation of the neutron density, the streaming of neutrons, and the disappearance of neutrons in the unit phase space. The right-hand side contains the contributions from scattering events and prompt and delayed neutrons emitted from the fission reactions. For the prompt fission contribution, the scalar neutron flux $\phi(\boldsymbol{r},E,t)$ estimated from the integration of the angular flux over all the angular directions is used. By normalizing the fission-related terms with the effective multiplication factor k_{eff}, the criticality condition is met even after the discretization of the equation. In addition, it is assumed that the small perturbations considered in neutron noise problems do not change k_{eff}.

Equation (2.2) gives the rate of change in the concentration $C_q(\boldsymbol{r},t)$ of the q-th family of delayed neutron precursors as the difference between the precursors created by fission and the precursors disappearing because of decay. The fraction of delayed neutrons and the decay constants for each precursor group are given by β_q and λ_q, respectively.

2.2 Static neutron transport equation

The steady-state spatial distribution of the neutron flux in a critical system is determined by solving the static neutron transport equation. The equation is derived from the kinetic equations (2.1) and (2.2) by setting the time derivatives to zero and assuming that all the terms are time-independent, and it reads as:

$$\begin{aligned}\left[\boldsymbol{\Omega}\cdot\nabla+\Sigma_{t,0}(\boldsymbol{r},E)\right]\psi_0(\boldsymbol{r},\boldsymbol{\Omega},E) &= \int_{4\pi}\int \Sigma_{s,0}(\boldsymbol{r},E'\to E,\boldsymbol{\Omega}'\to\boldsymbol{\Omega})\psi_0(\boldsymbol{r},\boldsymbol{\Omega}',E')dE' \\ &+\frac{1}{4\pi k_{eff}}\left[\chi_p(\boldsymbol{r},E)\left(1-\sum_q\beta_q(\boldsymbol{r})\right)+\sum_q\chi_{d,q}(\boldsymbol{r},E)\beta_q(\boldsymbol{r})\right]\int \nu\Sigma_{f,0}(\boldsymbol{r},E')\phi_0(\boldsymbol{r},E')dE' \qquad (2.3)\end{aligned}$$

The static quantities are denoted by the subscript “0”.

2.3 Frequency domain transport neutron noise equation

The perturbations that drive the neutron noise in a nuclear reactor can be described through variations of the macroscopic nuclear cross sections, which lead to spatial and temporal change in the neutron flux. In this work, the perturbations and thus the variations in the macroscopic nuclear cross sections are assumed to be small and stationary fluctuations around expected mean values. Then, the time-dependent fluxes, macroscopic cross sections, and precursor densities can be split into a time-independent term and a fluctuating part:

$$\psi(\boldsymbol{r},\boldsymbol{\Omega},E,t) = \psi_0(\boldsymbol{r},\boldsymbol{\Omega},E) + \delta\psi(\boldsymbol{r},\boldsymbol{\Omega},E,t) \tag{2.4}$$

$$\phi(\boldsymbol{r},E,t) = \phi_0(\boldsymbol{r},E) + \delta\phi(\boldsymbol{r},E,t) \tag{2.5}$$

$$\Sigma_x(\boldsymbol{r},E,t) = \Sigma_{x,0}(\boldsymbol{r},E) + \delta\Sigma_x(\boldsymbol{r},E,t) \tag{2.6}$$

$$C_q(\boldsymbol{r},t) = C_{q,0}(\boldsymbol{r}) + \delta C_q(\boldsymbol{r},t) \tag{2.7}$$

The fluctuation $\delta\Sigma_x$ is associated with the generic macroscopic cross section Σ_x and is used to model the driving perturbations. The quantities $\delta\psi(\boldsymbol{r},\boldsymbol{\Omega},E,t)$ and $\delta\phi(\boldsymbol{r},E,t)$ are the induced angular and scalar neutron noise, respectively.

The first order neutron noise equation in the frequency domain can be derived as follows. Equations (2.4) to (2.7) are introduced into Eqs. (2.1) to (2.2). The two resulting equations are combined, and Eq. (2.3) is subtracted. The second order perturbation terms ($\delta\psi\delta\Sigma_x$ and $\delta\phi\delta\Sigma_x$) are neglected, and a temporal Fourier transform is performed. This gives:

$$\left[\hat{\Omega}\cdot\nabla + \Sigma_{t,0}(\boldsymbol{r},E) + \frac{i\omega}{v(E)}\right]\delta\psi(\boldsymbol{r},\boldsymbol{\Omega},E,\omega) = \int\limits_{4\pi}\int \Sigma_{s,0}(\boldsymbol{r},E'\to E,\boldsymbol{\Omega}'\to\boldsymbol{\Omega})\delta\psi(\boldsymbol{r},\boldsymbol{\Omega}',E',\omega)dE'$$
$$+\frac{1}{4\pi k_{eff}}\left[\chi_p(\boldsymbol{r},E)\left(1-\sum_q \beta_q(\boldsymbol{r})\right)+\sum_q \chi_{d,q}(\boldsymbol{r},E)\frac{\lambda_q\beta_q(\boldsymbol{r})}{i\omega+\lambda_q}\right]\int \nu\Sigma_f(\boldsymbol{r},E',t)\delta\phi(\boldsymbol{r},E',t)dE'$$
$$+S(\boldsymbol{r},\boldsymbol{\Omega},E,\omega) \tag{2.8}$$

The noise source $S(\boldsymbol{r},\boldsymbol{\Omega},E,\omega)$ has the following expression:

$$S(\boldsymbol{r},\boldsymbol{\Omega},E,\omega) = -\delta\Sigma_t(\boldsymbol{r},E,\omega)\psi_0(\boldsymbol{r},\boldsymbol{\Omega},E) + \int\limits_{4\pi}\int \delta\Sigma_s(\boldsymbol{r},E'\to E,\boldsymbol{\Omega}'\to\boldsymbol{\Omega},\omega)\psi_0(\boldsymbol{r},\boldsymbol{\Omega}',E')dE'$$
$$+\frac{1}{4\pi k_{eff}}\left[\chi_p(\boldsymbol{r},E)\left(1-\sum_q \beta_q(\boldsymbol{r})\right)+\sum_q \chi_{d,q}(\boldsymbol{r},E)\frac{\lambda_q\beta_q(\boldsymbol{r})}{i\omega+\lambda_q}\right]\int \nu\delta\Sigma_f(\boldsymbol{r},E',\omega)\phi_0(\boldsymbol{r},E')dE' \tag{2.9}$$

In Eqs. (2.8) and (2.9), $\omega = 2\pi f$ is the angular frequency of the driving perturbation and i is the imaginary unit. Thus, the calculated neutron noise quantities take complex values and their amplitude and phase which bring a more intuitive physical meaning can be determined in a post-processing step.

The frequency-domain calculations have the advantage over time-domain calculations that the computational burden is reduced since the equations are solved for the characteristic frequency of the noise source and not for a time interval. However, the solution of the neutron noise equation in the frequency domain with complex values can still be challenging, as discussed in the following chapters.

2.4 Zero-power reactor transfer function

The transfer function of a nuclear reactor describes how a perturbation influences the reactor state variables such as the neutron flux. To illustrate some basic features of the neutron noise in reactors, the zero-power or open loop reactor transfer function is taken. This provides the system response in the case of small perturbations that do not lead to any reactivity feedback effect (so the power variation induced by the perturbation is small and has no relevant impact on the neutron multiplicity). In this section, the point-kinetic approximation is used for the modelling. Such an approximation is valid if the spatial distribution of the neutron flux remains identical to the one of the initial static neutron flux.

The point kinetics equations are derived from Eqs. (2.1) to (2.3) following a standard procedure (e.g., see [16]) and are based on the separation of the space- and time-dependent neutron flux into an amplitude factor $P(t)$ and a normalized shape function $\Psi(\boldsymbol{r},\boldsymbol{\Omega},E;t)$, i.e.:

$$\psi(\boldsymbol{r},\boldsymbol{\Omega},E,t) = P(t)\Psi(\boldsymbol{r},\boldsymbol{\Omega},E;t) \tag{2.10}$$

Under the assumption that the spatial shape function does not change in time, the resulting equation may be written as (using only one family of delayed neutron precursor):

$$\frac{dP(t)}{dt} = \frac{\rho(t) - \bar{\beta}}{\Lambda(t)} P(t) + \lambda C(t) \tag{2.11}$$

$$\frac{dC(t)}{dt} = \frac{\bar{\beta}}{\Lambda(t)} P(t) - \lambda C(t) \tag{2.12}$$

where $\rho(t)$ is the reactivity, $\Lambda(t)$ is the mean neutron generation time, $\bar{\beta}$ is the effective fraction of delayed neutrons, and λ is related to the decay of delayed-neutron precursors. The expressions of the quantities in Eqs. (2.11)-(2.12) can be found in [16].

A critical system initially operating in steady state at power P_0 is considered. The initial reactivity ρ_0 is thus equal to zero. The kinetics equations (2.11) and (2.12) have time-independent solutions P_0 and C_0 and their relationship is:

$$\frac{\bar{\beta}}{\Lambda} P_0 = \lambda C_0 \tag{2.13}$$

When the reactivity is perturbed by a small amount $\delta\rho$, small perturbations are caused in both the amplitude factor $P(t)$ and the delayed neutron precursor density $C(t)$. The reactivity, the amplitude factor and the delayed neutron precursor density are split into their mean values and fluctuating parts:

$$\rho(t) = \rho_0 + \delta\rho(t) \tag{2.14}$$

$$P(t) = P_0 + \delta P(t) \tag{2.15}$$

$$C(t) = C_0 + \delta C(t) \tag{2.16}$$

The relationship between the response of the system δP and the perturbation $\delta \rho$ may be obtained by inserting Eqs. (2.14) to (2.16) into Eqs. (2.11) and (2.12), neglecting the second-order terms, subtracting Eq. (2.13) from the results, and performing a temporal Fourier transform, and reads as:

$$\delta P(\omega) = P_0 G_0(\omega) \delta \rho(\omega) \tag{2.17}$$

The function $G_0(\omega)$ is the zero-power reactor transfer function in the frequency domain and has the following expression:

$$G_0(\omega) = \frac{1}{i\omega\left(\Lambda + \frac{\bar{\beta}}{i\omega + \lambda}\right)} \tag{2.18}$$

The quantity i is the imaginary unity, so $G_0(\omega)$ takes complex values. The quantity ω is the angular frequency of the perturbation.

Equation (2.18) indicates that the amplitude factor oscillates with an amplitude that is proportional to the amplitude of $G_0(\omega)$, at the same frequency of the perturbation, but with a phase shift given by the phase of $G_0(\omega)$. In Fig. 2.1, the amplitude and phase of $G_0(\omega)$ is plotted with respect to the angular frequency with $\bar{\beta} = 0.0075$, $\lambda = 0.08\, s^{-1}$ and $\Lambda = 6 \times 10^{-5}\, s$. The so-called plateau region, where the amplitude is nearly constant (approximately equal to $1/\beta$) and the phase is close to zero, is observed for $\lambda \ll \omega \ll \beta/\Lambda$.

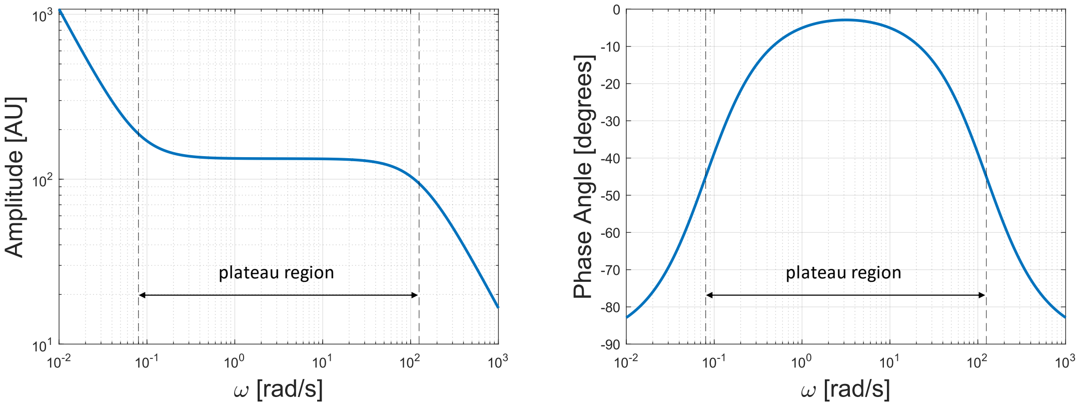

Figure 2.1 Amplitude (left) and phase (right) of the zero-power reactor transfer function $G_0(\omega)$

Chapter 3

The solver NOISE-SN

The solver NOISE-SN is developed in MATLAB to explore algorithms based on the discrete ordinates method for the solution of the frequency-domain neutron noise equations. In Section 3.1, the overall calculation scheme of the solver is provided. In Section 3.2, the energy, angular and spatial discretization schemes are introduced. In Section 3.3, the transport sweeps, and the iterative procedure for solving the discretized equations are discussed.

3.1 Calculation scheme

Equations (2.8) and (2.9) require the static neutron flux and the effective multiplication factor k_{eff}. Therefore, NOISE-SN consists of a static and a dynamic module. For every new system considered, the static module first solves the static equation (2.3). The dynamic module solves Eqs. (2.8) and (2.9) provided the necessary information about the static configuration (static flux and k_{eff}) and the perturbation (position, amplitude, and frequency). The two modules can be used independently, so static calculations do not need to be repeated for neutron noise problems based on the same static, critical system.

3.2 Discretization of the transport equation

For the numerical solution, the continuous equations (2.3) and (2.8)-(2.9) are discretized with respect to the energy E, the angular direction $\boldsymbol{\Omega}$ and the spatial position $\boldsymbol{r}$. The discretization of the static and noise equations follows the same approach. In this section, the details are given only for the neutron noise equation (2.8)-(2.9).

3.2.1 Multi-energy group formalism

The continuous energy dependence is treated with the multi-energy-group formalism. The range of all possible neutron energy is divided into G energy bins as:

$$[E_{min}: E_{max}] = \bigcup_{g=G}^{1} [E_g: E_{g-1}] \tag{3.1}$$

Conventionally, the first group ($g = 1$) contains the neutrons with highest energies and the lowest energy neutrons belong to the last group ($g = G$). The multi-energy-group transport neutron noise equation can then be obtained by integrating Eqs. (2.8)-(2.9) over each of the predefined energy bins, and this results in:

$$\left[\boldsymbol{\Omega}\cdot\nabla+\Sigma_{t,g,0}(\boldsymbol{r})+\frac{i\omega}{v_g(\boldsymbol{r})}\right]\delta\psi_g(\boldsymbol{r},\boldsymbol{\Omega},\omega)=\int_{4\pi}\sum_{g'=1}^{G}\Sigma_{s,0g'\to g}(\boldsymbol{r},\boldsymbol{\Omega}'\to\boldsymbol{\Omega})\delta\psi_{g'}(\boldsymbol{r},\boldsymbol{\Omega}',\omega)$$
$$+\frac{1}{4\pi k_{eff}}\left[\chi_{p,g}(\boldsymbol{r})\left(1-\sum_q\beta_q(\boldsymbol{r})\right)+\sum_q\chi_{d,q,g}(\boldsymbol{r})\frac{\lambda_q\beta_q(\boldsymbol{r})}{i\omega+\lambda_q}\right]\sum_{g'=1}^{G}\nu\Sigma_{f,g'}(\boldsymbol{r},t)\delta\phi_{g'}(\boldsymbol{r},t)$$
$$+S_g(\boldsymbol{r},\boldsymbol{\Omega},\omega) \tag{3.2}$$

and

$$\mathrm{S_g}(\boldsymbol{r},\boldsymbol{\Omega},\omega)=-\delta\Sigma_{t,g}(\boldsymbol{r},\omega)\psi_{g,0}(\boldsymbol{r},\boldsymbol{\Omega})+\int_{4\pi}\sum_{g'}\delta\Sigma_{s,g'\to g}(\boldsymbol{r},\boldsymbol{\Omega}'\to\boldsymbol{\Omega},\omega)\,\psi_{g',0}(\boldsymbol{r},\boldsymbol{\Omega}')d\boldsymbol{\Omega}'$$
$$+\frac{1}{k_{eff}}\left[\chi_{p,g}(\mathbf{r})\left(1-\sum_q\beta_q(\mathbf{r})\right)+\sum_q\chi_{d,q,g}(\mathbf{r})\frac{\lambda_q\beta_q(\mathbf{r})}{\mathrm{i}\omega+\lambda_q}\right]\sum_{g'}\nu\delta\Sigma_{f,g'}(\mathbf{r},\omega)\phi_{g',0}(\mathbf{r}) \tag{3.3}$$

The multi-group velocity becomes space-dependent because of the procedure for preparing the group constants [17].

3.2.2 Discrete ordinates method

Equations (3.2)-(3.3) are discretized with respect to the angular variable according to the discrete ordinates ($\mathrm{S_N}$) method. The $\mathrm{S_N}$ method has been widely used to solve both the static and time-dependent neutron transport equation because of its simplicity in the derivation process and its good computational efficiency while avoiding excessive computer memory consumption [18]. The multi-group neutron noise equation (3.2) has the same integro-differential form as the static equation. The application of the $\mathrm{S_N}$ method to this equation is thus straightforward and is briefly presented in the following.

The principle of this method assumes that the transport equation, e.g., Eq. (3.2), holds for a number N_0 of discrete angular directions, i.e., $\boldsymbol{\Omega_1},\dots,\boldsymbol{\Omega_n},\dots\boldsymbol{\Omega_{N_0}}$. In three dimensional cartesian geometry, the discrete angular directions $\boldsymbol{\Omega_n}$ is given by the direction cosines along the orthogonal x, y and z directions:

$$\boldsymbol{\Omega}_n=\boldsymbol{\Omega}(\mu_n,\eta_n,\xi_n) \tag{3.4}$$

The integration over angle is approximated by performing a weighted sum of the discrete angular points. The associated weights w_n are positive, and in this work, they are normalized by:

$$\sum_n w_n = 1 \tag{3.5}$$

The discrete ordinate points $\boldsymbol{\Omega_n}$ together with the associated weights w_n form a quadrature set for the S_N approximation.

There exist many techniques for generating the quadrature sets, see e.g. [19]. The Level-symmetric (LQ_N) [18] and Legendre-Chebyshev (P_N-T_N) [20] quadrature sets are the most used and are implemented in NOISE-SN. Both quadrature sets contain symmetric directions over the unit sphere. In the 3-dimensional case, for a S_N approximation of order N, they both contain $N(N+2)/8$ ordinates per octant and thus a total of $N_0 = N(N+2)$ number of ordinates. However, the LQ_N set is limited to $N < 20$ to avoid negative weights. Then, both quadrature sets are suitable for problems where a low order SN approximation is sufficient for an accurate solution. If high orders of S_N are required, the P_N-T_N set is used.

In NOISE-SN, the scattering term is approximated by an L-order real spherical harmonics expansion, in a way similar to the static case, as presented in [21].

The discrete ordinates formalism of Eq. (3.2)-(3.3) can be written as:

$$\begin{aligned}
&\left[\mu_n \frac{\partial}{\partial x} + \eta_n \frac{\partial}{\partial y} + \xi_n \frac{\partial}{\partial z} + \Sigma_{t,g,0}(\boldsymbol{r}) + \frac{i\omega}{v_g(\vec{r})}\right] \delta\psi_{g,n}(\vec{r},\omega) \\
&= \sum_{g'} \sum_{l=0}^{L} (2l+1) \Sigma_{sl,g'\to g,0}(\boldsymbol{r}) \sum_{m=-l}^{l} R_l^m(\boldsymbol{\Omega_n}) \delta\phi_{l,g'}^m(\boldsymbol{r},\omega) \\
&\qquad + \frac{1}{k_{eff}} \chi_g^{dyn}(\boldsymbol{r}) \sum_{g'} \nu\Sigma_{f,g',0}(\boldsymbol{r}) \delta\phi_{g'}(\boldsymbol{r},\omega) + S_{g,n}(\boldsymbol{r},\omega)
\end{aligned} \tag{3.6}$$

and

$$\begin{aligned}
S_{g,n}(\boldsymbol{r},\omega) = &-\delta\Sigma_{t,g}(\boldsymbol{r},\omega)\psi_{g,n,0}(\boldsymbol{r}) + \sum_{g'} \sum_{l=0}^{L} (2l+1) \delta\Sigma_{sl,g'\to g}(\boldsymbol{r},\omega) \sum_{m=-l}^{l} R_l^m(\boldsymbol{\Omega_n}) \phi_{l,g',0}^m(\boldsymbol{r}) \\
&+ \frac{1}{k_{eff}} \chi_g^{dyn}(\boldsymbol{r}) \sum_{g'} \nu\delta\Sigma_{f,g'}(\boldsymbol{r},\omega) \phi_{l=0,g',0}^{m=0}(\boldsymbol{r})
\end{aligned} \tag{3.7}$$

The multiplication of $1/(4\pi)$ in the fission term is eliminated due to the normalization condition of the weighting factor, i.e., Eq. (3.5). The moments of the neutron noise $\delta\phi_{l,g}^m$, are computed with the quadrature summation:

$$\delta\phi_{l,g}^m(\omega,\boldsymbol{r}) = \sum_n w_n \, R_l^m(\boldsymbol{\Omega_n}) \delta\psi_{g,n}(\omega,\boldsymbol{r}) \tag{3.8}$$

The fission spectrum term is given by:

$$\chi_g^{dyn}(\boldsymbol{r}) = \left[\chi_{p,g}(\boldsymbol{r})\left(1-\sum_q \beta_q(\boldsymbol{r})\right)+\sum_q \chi_{d,q,g}(\boldsymbol{r})\frac{\lambda_q\beta_q(\boldsymbol{r})}{i\omega+\lambda_q}\right] \tag{3.9}$$

3.2.3 Diamond finite difference scheme

In this work, the discretization with respect to the spatial variable is based on the diamond finite difference scheme. The spatial differencing scheme is again consistent for both the static and dynamic module, and the description is given only for the neutron noise equations.

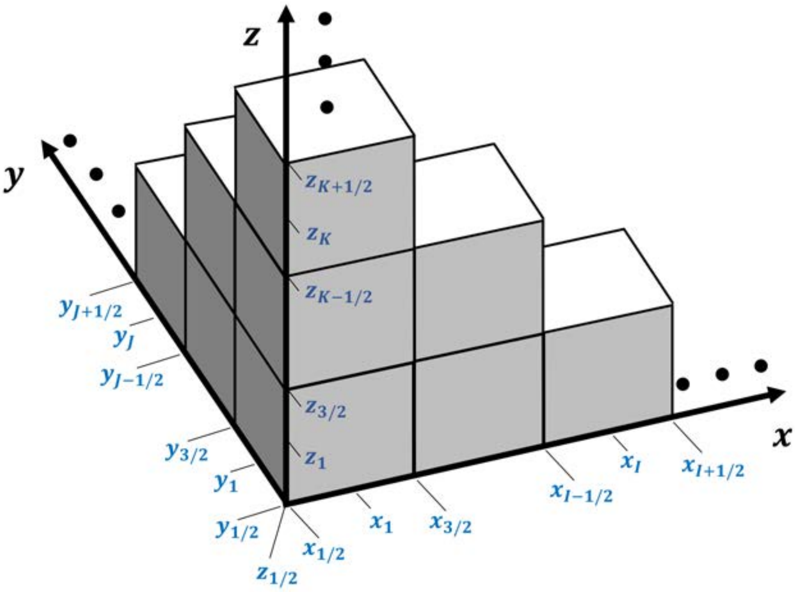

Figure 3.1 Spatial discretization of a 3-D system into cuboids

A 3-D system is considered and is divided into rectangular cuboids, as shown in Fig. 3.1. The cuboids are bounded by the surfaces perpendicular to the three axes. The position coordinates of the surfaces are $x_{1/2}, x_{3/2}, \cdots, x_{I_{max}+1/2}$ in the x direction, $y_{1/2}, y_{3/2}, \cdots, y_{J_{max}+1/2}$ in the y direction and $z_{1/2}, z_{3/2}, \cdots, z_{K_{max}+1/2}$ in the z direction. The side length of each cuboid is thus $\Delta x_I = x_{I+1/2} - x_{I-1/2}$, $\Delta y_J = y_{J+1/2} - y_{J-1/2}$ and $\Delta z_K = z_{K+1/2} - z_{K-1/2}$. In each cuboid, the system parameters take constant values and change only at the surfaces denoted by the half-integers.

The fully discretized neutron noise equation is obtained by integrating Eqs. (3.6)-(3.7) over the generic cell (I, J, K) and dividing by the cell volume $V_{I,J,K} = \Delta x_I \Delta y_J \Delta z_K$. This results in:

$$\frac{\mu_n}{\Delta x_I}\left[\delta\psi_{g,n,I+1/2,J,K}(\omega)-\delta\psi_{g,n,I-1/2,J,K}(\omega)\right]+\frac{\eta_n}{\Delta y_J}\left[\delta\psi_{g,n,I,J+1/2,K}(\omega)-\delta\psi_{g,n,I,J-1/2,K}(\omega)\right]$$
$$+\frac{\xi_n}{\Delta z_K}\left[\delta\psi_{g,n,I,J,K+1/2}(\omega)-\delta\psi_{g,n,I,J,K-1/2}(\omega)\right]+\left[\Sigma_{t,g,0,I,J,K}+\frac{i\omega}{v_{g,I,J,K}}\right]\delta\psi_{g,n,I,J,K}(\omega)$$
$$=\sum_{g'}\sum_{l=0}^{L}(2l+1)\Sigma_{sl,g'\to g,0,I,J,K}\sum_{m=-l}^{l}R_l^m(\boldsymbol{\Omega_n})\delta\phi_{l,g',I,J,K}^m(\omega)$$
$$+\frac{1}{k_{eff}}\chi_{g,I,J,K}^{dyn}\sum_{g'}\nu\Sigma_{f,g',0,I,J,K}\delta\phi_{g',I,J,K}(\omega)+S_{g,n,I,J,K}(\omega) \qquad (3.10)$$

and

$$S_{g,n,I,J,K}(\omega)=-\delta\Sigma_{t,g,I,J,K}(\omega)\psi_{g,n,I,J,K,0}+\sum_{g'}\sum_{l=0}^{L}(2l+1)\delta\Sigma_{sl,g'\to g,I,J,K}(\omega)\sum_{m=-l}^{l}R_l^m(\boldsymbol{\Omega_n})\phi_{l,g',I,J,K,0}^m$$
$$+\frac{1}{k_{eff}}\chi_{g,I,J,K}^{dyn}\sum_{g'}\nu\delta\Sigma_{f,g',I,J,K}(\omega)\phi_{l=0,g',I,J,K,0}^{m=0} \qquad (3.11)$$

The neutron noise with half-integer position indices represents surface-averaged quantities and the neutron noise with integer position indices represents volume-averaged quantities, e.g.:

$$\delta\psi_{g,n,I+\frac{1}{2},J,K}=\frac{1}{\Delta y_J\Delta z_K}\int\int\delta\psi_{g,n}\left(x_{I+\frac{1}{2}},y_J,z_K\right)dydz \qquad (3.12)$$

$$\delta\psi_{g,n,I,J,K}=\frac{1}{V_{I,J,K}}\int\int\int\delta\psi_{g,n}(x_I,y_J,z_K)\,dxdydz \qquad (3.13)$$

The diamond relationships are then introduced between the volume-averaged and surface-averaged quantities, i.e.:

$$\delta\psi_{g,n,I,J,K}(\omega)=\frac{1}{2}\left(\delta\psi_{g,n,I+\frac{1}{2},J,K}(\omega)+\delta\psi_{g,n,I-\frac{1}{2},J,K}(\omega)\right) \qquad (3.14)$$

$$\delta\psi_{g,n,I,J,K}(\omega)=\frac{1}{2}\left(\delta\psi_{g,n,I,J+\frac{1}{2},K}(\omega)+\delta\psi_{g,n,I,J-\frac{1}{2},K}(\omega)\right) \qquad (3.15)$$

$$\delta\psi_{g,n,I,J,K}(\omega)=\frac{1}{2}\left(\delta\psi_{g,n,I,J,K+\frac{1}{2}}(\omega)+\delta\psi_{g,n,I,J,K-\frac{1}{2}}(\omega)\right) \qquad (3.16)$$

3.3 Transport calculation

The solution of both the fully discretized static neutron transport equation and the transport neutron noise equation is based on the conventional inner-outer iterative scheme. The scheme is described for the dynamic module. The solution procedure in the static module is similar and the differences are briefly discussed at the end of the section.

For the inner iterations, each energy group is considered separately, starting from the first energy group. Within each inner iteration for one energy group, a process referred to as the transport sweep is performed. In the transport sweep, the angular quantities are sequentially calculated in each cell by following the direction of neutron travel. Thus, the order of the spatial sweep depends on the angular direction.

The sweeping process for a direction in the first octant ($\mu_n > 0, \eta_n > 0, \xi_n > 0$) is given as an example. The sweep starts from the cell ($I = 1, J = 1, K = 1$) and proceeds in the direction of increasing I, J and K, assuming that the surface-averaged quantities on the $I = 1/2, J = 1/2$ and $K = 1/2$ plane are known from previous calculation or from the boundary condition. Then for a generic cell (I, J, K), the volume-averaged angular neutron noise is calculated from:

$$\overline{\delta\psi}_{g,n,I,J,K}(\omega) = \frac{\left[2\frac{\mu_n}{\Delta x_I}\delta\psi_{g,n,I-\frac{1}{2},J,K}(\omega) + 2\frac{\eta_n}{\Delta y_J}\delta\psi_{g,n,I,J-\frac{1}{2},K}(\omega) + 2\frac{\xi_n}{\Delta z_K}\delta\psi_{g,n,I,J,K-\frac{1}{2}}(\omega) + q_{g,n,I,J,K}\right]}{\left[\Sigma_{t,g,0,I,J,K} + \frac{i\omega}{v_{g,I,J,K}} + 2\frac{\mu_n}{\Delta x_I} + 2\frac{\eta_n}{\Delta y_J} + 2\frac{\xi_n}{\Delta z_K}\right]} \tag{3.17}$$

Equation (3.17) is derived by eliminating the angular quantities $\delta\psi_{g,n,I+\frac{1}{2},J,K}$, $\delta\psi_{g,n,I,J+\frac{1}{2},K}$ and $\delta\psi_{g,n,I,J,K+\frac{1}{2}}$ on the exiting surfaces (i.e., the values on the surfaces through which neutrons leave the cell) from Eq. (3.10), using Eqs. (3.14) to (3.16). The angular quantities $\delta\psi_{g,n,I-\frac{1}{2},J,K}$, $\delta\psi_{g,n,I,J-\frac{1}{2},K}$ and $\delta\psi_{g,n,I,J,K-\frac{1}{2}}$ on the three incoming surfaces are either known from previous calculations or from the boundary condition. The source term $q_{g,n,I,J,K}$ is also known from previous iterations and from the prescribed noise source. Then the exiting-surface values are computed according to:

$$\delta\psi_{g,n,I+\frac{1}{2},J,K}(\omega) = 2\delta\psi_{g,n,I,J,K}(\omega) - \delta\psi_{g,n,I-\frac{1}{2},J,K}(\omega) \tag{3.18}$$

$$\delta\psi_{g,n,I,J+\frac{1}{2},K}(\omega) = 2\delta\psi_{g,n,I,J,K}(\omega) - \delta\psi_{g,n,I,J-\frac{1}{2},K}(\omega) \tag{3.19}$$

$$\delta\psi_{g,n,I,J,K+\frac{1}{2}}(\omega) = 2\delta\psi_{g,n,I,J,K}(\omega) - \delta\psi_{g,n,I,J,K-\frac{1}{2}}(\omega) \tag{3.20}$$

The sweep for the directions in the other octants is performed in an analogous manner by following the direction of neutron travel.

After the sweep along all the directions has been completed, the volume averaged quantities $\delta\psi_{g,n,I,J,K}(\omega)$ are obtained for all n, I, J and K, and they are used to calculate the moments in each cell, according to:

$$\delta\phi^{m}_{l,g,I,J,K}(\omega) = \sum_{n} w_n\, R^{m}_{l}(\boldsymbol{\Omega_n})\delta\psi_{g,n,I,J,K}(\omega) \tag{3.21}$$

The moments are then used to update the with-in group scattering source term in each computational cell, and one inner iteration for one energy group is completed. The inner iterations can be performed for multiple N_I times based on the need.

The down-scattering term, i.e., scattering from higher energy groups to lower energy groups, is automatically updated in the process by performing the inner iterations from the first to the last energy group. When the inner iterations are completed for all energy groups, the fission source term and the full scattering term are updated, and an outer iteration is concluded.

The inner-outer iterative process is given in Algorithm 1, and it is referred to as the unaccelerated scheme since no numerical acceleration is applied. The accelerated version is presented in the next chapter.

Algorithm 1: Unaccelerated scheme for the dynamic module

```
1:   Begin with $\delta\phi^{m}_{l,g,I,J,K} = 0$ and $\delta\psi_{g,n,I,J,K} = 0$
2:       while $\Re^{err}$ $or\, \Im^{err} > \varepsilon$
3:           for $g$=1 to $g = G$ do
4:               for inner iteration count $\leq N_I$ do
5:                   Sweep through the angular directions and spatial domain
6:                   Update moments and self-scattering term
7:               end for
8:           end for
9:           Update fission source term and scattering terms
10:      end while
```

In line 2 of Algorithm 1, the convergence criterion is given. A convergence criterion based on the residuals of the S_N solutions would be very time-consuming because of the size of the numerical problem. Then the convergence is checked on the relative differences computed between the last two iterations (ITE and $ITE-1$), for both the real and imaginary part of the scalar neutron noise, as:

$$\Re^{err} = \left\| \frac{\Re\left(\delta\phi^{m=0,ITE}_{l=0,g,I,J,K} - \delta\phi^{m=0,ITE-1}_{l=0,g,I,J,K}\right)}{\Re\left(\delta\phi^{m=0,ITE}_{l=0,g,I,J,K}\right)} \right\|_{\infty} < \varepsilon \tag{3.22}$$

$$\Im^{err} = \left\| \frac{\Im\left(\delta\phi^{m=0,ITE}_{l=0,g,I,J,K} - \delta\phi^{m=0,ITE-1}_{l=0,g,I,J,K}\right)}{\Im\left(\delta\phi^{m=0,ITE}_{l=0,g,I,J,K}\right)} \right\|_{\infty} < \varepsilon \tag{3.23}$$

For slowly converging iteration schemes, the use of Eqs. (3.22)-(3.23) may lead to false convergence. To avoid this issue, the value of the convergence tolerance ε must be selected very small. In this work, calculations are usually performed with ε equal to 10^{-6}, which was found to provide satisfactory results.

The same iterative scheme is applied in the static module with the following difference:

- The initial guess is given as $\psi_{g,n,I,J,K} = 1$ for all g, n, I, J, K, and the moments $\phi^{m}_{l,g,I,J,K}$ are calculated in an analogous way to Eq. (3.21).
- In the outer iterations, the update of the fission source term includes both the update of the scalar flux $\phi^{m=0}_{l=0,,I,J,K,0}$ and the update of the effective multiplication factor k_{eff}, using the power iteration method [18].
- The diamond difference scheme may yield negative static angular flux values on the exiting surfaces in the transport sweep process, so a negative-flux fixup is performed. If the calculated surface angular flux is negative, it is set to zero and the volume averaged angular flux is re-evaluated.
- The convergence is checked for the scalar flux in a point-wise manner and for the effective multiplication factor.

Chapter 4

Acceleration

In the development of the solver NOISE-SN, the Diffusion Synthetic Acceleration (DSA) is first considered due to its advantage in providing an unconditionally stable scheme, see Section 4.1. A significant acceleration effect is achieved, but a large number of iterations is still required. Then, the Coarse Mesh Finite Difference (CMFD) method is studied to accelerate the calculations further, see Section 4.2. The two methods are used to solve a neutron noise problem based on a benchmark configuration and their performances are compared, see Section 4.3. The discussion is based on Paper I, Paper III and Paper IV.

4.1 Diffusion Synthetic Acceleration

The DSA method has been mainly used to accelerate static calculations and has proven to be very efficient [22,23]. The biggest advantage of the DSA method is the unconditionally stable convergence behavior, given that the DSA equations are properly derived.

Hence, the DSA method is investigated in the case of the discrete ordinates method applied to the solution of the neutron noise equations in the frequency domain. It is implemented and tested in both the static and dynamic module of NOISE-SN.

The DSA method is presented for the specific case of calculations in 2-dimensional systems, with 2-energy groups. The convergence of both the unaccelerated and DSA schemes is analyzed. The method is mainly described for the neutron noise calculations.

The DSA method can be used to accelerate both the inner and the outer iterations. Accordingly, two sets of low-order diffusion-like equations are solved to provide corrections for the scalar and angular quantities calculated from the transport sweep process, and thus to make convergence faster. The discretization of the DSA equations needs to follow the transport equation to guarantee a stable convergence behavior. The derivation process of the DSA equations for neutron noise calculations are identical to the static case [24]; only the final equations implemented in NOISE-SN are given below.

For convenience, the outer iteration number and the inner iteration number are denoted by n_o and n_i, respectively, and the inner iterations are performed a maximum of N_I times. The transport sweep at the n_i-th inner iteration, within the $(n_o + 1)$-th outer iteration, is given, in two dimensions, as:

$$\frac{\mu_n}{\Delta x}\left[\overline{\delta\psi}_{n,I+1/2,J}^{(n_o,n_i+1/2)}(\omega) - \overline{\delta\psi}_{n,I-1/2,J}^{(n_o,n_i+1/2)}(\omega)\right] + \frac{\eta_n}{\Delta y}\left[\overline{\delta\psi}_{n,I,J+1/2}^{(n_o,n_i+1/2)}(\omega) - \overline{\delta\psi}_{n,I,J-1/2}^{(n_o,n_i+1/2)}(\omega)\right]$$

$$+\overline{\overline{\Sigma}}_{\mathrm{t},I,J}^{\mathrm{dyn}}\,\overline{\delta\psi}_{n,I,J}^{(n_o,n_i+1/2)}(\omega)$$

$$= \overline{\overline{\Sigma_{ss}}}_{I,J}\,\overline{\delta\phi}_{I,J}^{(n_o,n_i)}(\omega) + \overline{\overline{\Sigma_{sd}}}_{I,J}\,\overline{\delta\phi}_{I,J}^{(n_o,N_I)}(\omega) + \overline{\overline{\chi}}_{\mathrm{I,J}}\,\overline{\overline{\nu\Sigma_{\mathrm{f}}}}_{I,J}^{T}\,\overline{\delta\phi}_{I,J}^{(n_o,0)}(\omega) + \bar{S}_{n,I,J}(\omega) \qquad (4.1)$$

The vectors and matrices in Eq. (4.1) are defined as:

$$\overline{\delta\psi}_{n,I,J}^{(n_o,n_i+1/2)} = \begin{bmatrix} \delta\psi_{1,n,I,J}^{(n_o,n_i+1/2)} \\ \delta\psi_{2,n,I,J}^{(n_o,n_i+1/2)} \end{bmatrix} \qquad (4.2)$$

$$\overline{\delta\phi}_{I,J}^{(n_o,n_i)} = \begin{bmatrix} \delta\phi_{1,I,J}^{(n_o,n_i)} \\ \delta\phi_{2,I,J}^{(n_o,n_i)} \end{bmatrix} \qquad (4.3)$$

$$\bar{S}_{i,j}(\omega) = \begin{bmatrix} S_{1,n,I,J}(\omega) \\ S_{2,n,I,J}(\omega) \end{bmatrix} \qquad (4.4)$$

$$\overline{\overline{\Sigma_{ss}}}_{I,J} = \begin{bmatrix} \Sigma_{s0,1\to 1,0,I,J} & 0 \\ 0 & \Sigma_{s0,2\to 2,0,I,J} \end{bmatrix} \qquad (4.5)$$

$$\overline{\overline{\Sigma_{sd}}}_{I,J} = \begin{bmatrix} 0 & \Sigma_{s,1\to 2,0,I,J} \\ 0 & 0 \end{bmatrix} \qquad (4.6)$$

$$\overline{\overline{\Sigma}}_{\mathrm{t},I,J}^{\mathrm{dyn}} = \begin{bmatrix} \Sigma_{t,1,0,I,J} + \dfrac{i\omega}{v_{1,I,J}} & 0 \\ 0 & \Sigma_{t,2,0,I,J} + \dfrac{i\omega}{v_{2,I,J}} \end{bmatrix} \qquad (4.7)$$

$$\overline{\nu\Sigma_f}_{I,J} = \frac{1}{k_{eff}}\left[\nu\Sigma_{f,1,0,I,J} \quad \nu\Sigma_{f,2,0,I,J}\right]^T \qquad (4.8)$$

$$\bar{\chi}_{I,J} = \begin{bmatrix} \chi_{\mathrm{p},1,I,J}\displaystyle\sum_{\mathrm{q}}\left(1-\beta_{q,I,J}\right) + \sum_{\mathrm{q}}\chi_{\mathrm{d,q},1,I,J}\frac{\lambda_{\mathrm{q}}\beta_{\mathrm{q},I,J}}{i\omega+\lambda_{\mathrm{q}}} \\ \chi_{\mathrm{p},2,I,J}\displaystyle\sum_{\mathrm{q}}\left(1-\beta_{q,I,J}\right) + \sum_{\mathrm{q}}\chi_{\mathrm{d,q},2,I,J}\frac{\lambda_{\mathrm{q}}\beta_{\mathrm{q},I,J}}{i\omega+\lambda_{\mathrm{q}}} \end{bmatrix} \qquad (4.9)$$

The angular neutron noise is then used to compute the scalar flux:

$$\overline{\delta\phi}_{I,J}^{(n_o,n_i+1/2)}(\omega) = \sum_{\mathrm{n=1}}^{\mathrm{N_0}} w_n \overline{\delta\psi}_{n,I,J}^{\left(n_o,n_i+\frac{1}{2}\right)}(\omega) \tag{4.10}$$

Before moving to the next inner iteration, the DSA method is applied in each energy group. The correction quantity δf for the inner iteration is obtained by solving:

$$\begin{aligned}
&\frac{2}{\Delta x_I}\left(\Delta y_J D_{g,I,J} + \Delta y_{J+1} D_{g,I,J+1}\right)\left(\delta f_{g,I+1/2,J+1/2}^{(n_o,n_i+1)} - \delta f_{g,I-1/2,J+1/2}^{(n_o,n_i+1)}\right) \\
&-\frac{2}{\Delta x_{I+1}}\left(\Delta y_J D_{g,I+1,J} + \Delta y_{J+1} D_{g,I+1,J+1}\right)\left(\delta f_{g,I+3/2,J+1/2}^{(n_o,n_i+1)} - \delta f_{g,I+1/2,J+1/2}^{(n_o,n_i+1)}\right) \\
&+\frac{2}{\Delta y_J}\left(\Delta x_I D_{g,I,J} + \Delta x_{I+1} D_{g,I+1,J}\right)\left(\delta f_{g,I+1/2,J+1/2}^{(n_o,n_i+1)} - \delta f_{g,I+1/2,J-1/2}^{(n_o,n_i+1)}\right) \\
&-\frac{2}{\Delta y_{J+1}}\left(\Delta x_I D_{g,I,J+1} + \Delta x_{I+1} D_{g,I+1,J+1}\right)\left(\delta f_{g,I+1/2,J+3/2}^{(n_o,n_i+1)} - \delta f_{g,I+1/2,J+1/2}^{(n_o,n_i+1)}\right) \\
&+\left[\sum_{I'=I}^{I+1}\sum_{J'=J}^{J+1}\left(\Sigma_{R,g,I',J'} V_{I',J'}\right)\right]\delta f_{g,I+1/2,J+1/2}^{(n_o,n_i+1)} = \sum_{I'=I}^{I+1}\sum_{J'=J}^{J+1}\Sigma_{ss,g,I',J'} V_{I',J'}\left(\delta\phi_{g,I',J'}^{(n_o,n_i+1/2)} - \delta\phi_{g,I',J'}^{(n_o,n_i)}\right)
\end{aligned} \tag{4.11}$$

where

$$D_{g,I,J} = \frac{1}{3\left(\Sigma_{t,g,0,I,J} + \frac{i\omega}{v_{g,I,J}}\right)} \tag{4.12}$$

$$\Sigma_{R,g,I,J} = \Sigma_{t,g,0,I,J} + \frac{i\omega}{v_{g,I,J}} - \Sigma_{s0,g\rightarrow g,0,I,J} \tag{4.13}$$

Eq. (4.11) represents a fixed source problem, and the linear system of equations is solved with the LU factorization method. The solution of Eq. (4.11) provides the correction quantity δf at cell vertices, and they are used to update the cell-center scalar neutron noise:

$$\delta\phi_{g,I,J}^{(n_o,n_i+1)} = \delta\phi_{g,I,J}^{\left(n_o,n_i+\frac{1}{2}\right)} + \frac{1}{4}\sum_{I'=I}^{I+1}\sum_{J'=J}^{J+1}\delta f_{g,I'-\frac{1}{2},J'-\frac{1}{2}}^{(n_o,n_i+1)} \tag{4.14}$$

The adjusted values given by Eq. (4.14) are then used to update the self-scattering term.

After the inner iterations are performed for all the energy groups, the correction quantities $\overline{\delta F}$ for the (n_o+1)-th outer iteration are computed for the two energy groups by solving the outer DSA equation, i.e.:

$$\begin{aligned}
&\frac{2}{\Delta x_I}\left(\Delta y_J \overline{\overline{D}}_{I,J} + \Delta y_{J+1}\overline{\overline{D}}_{I,J+1}\right)\left(\overline{\delta F}^{(n_o+1)}_{I+1/2,J+1/2} - \overline{\delta F}^{(n_o+1)}_{I-1/2,J+1/2}\right)\\
&-\frac{2}{\Delta x_{I+1}}\left(\Delta y_J \overline{\overline{D}}_{I+1,J} + \Delta y_{J+1}\overline{\overline{D}}_{I+1,J+1}\right)\left(\overline{\delta F}^{(n_o+1)}_{I+3/2,J+1/2} - \overline{\delta F}^{(n_o+1)}_{I+1/2,J+1/2}\right)\\
&+\frac{2}{\Delta y_J}\left(\Delta x_I \overline{\overline{D}}_{I,J} + \Delta x_{I+1}\overline{\overline{D}}_{I+1,J}\right)\left(\overline{\delta F}^{(n_o+1)}_{I+1/2,J+1/2} - \overline{\delta F}^{(n_o+1)}_{I+1/2,J-1/2}\right)\\
&-\frac{2}{\Delta y_{J+1}}\left(\Delta x_I \overline{\overline{D}}_{I,J+1} + \Delta x_{I+1}\overline{\overline{D}}_{I+1,J+1}\right)\left(\overline{\delta F}^{(n_o+1)}_{I+1/2,J+3/2} - \overline{\delta F}^{(n_o+1)}_{I+1/2,J+1/2}\right)\\
&+\left[\sum_{I'=I}^{I+1}\sum_{J'=J}^{J+1}\left(\overline{\overline{\Sigma}}_{R,I',J'}V_{I',J'}\right)\right]\overline{\delta F}^{(n_o+1)}_{I+1/2,J+1/2}\\
&-\left[\sum_{I'=I}^{I+1}\sum_{J'=J}^{J+1}\left(\overline{\overline{\Sigma}}_{sd,I',J'}V_{I',J'}\right)\right]\overline{\delta F}^{(n_o+1)}_{I+\frac{1}{2},J+\frac{1}{2}} = \sum_{I'=I}^{I+1}\sum_{J'=J}^{J+1}\overline{\overline{\chi}}_{\mathrm{I}',\mathrm{J}'}\,\overline{\overline{\nu\Sigma}}_{\mathrm{f}\,\mathrm{I}',\mathrm{J}'}V_{I',J'}\left(\overline{\delta\phi}^{(n_o,N_I)}_{I',J'} - \overline{\delta\phi}^{(n_o)}_{I',J'}\right)
\end{aligned} \tag{4.15}$$

where

$$\overline{\overline{\Sigma}}_{R,I,J} = \begin{bmatrix} \Sigma_{t,1,0,I,J} + \dfrac{i\omega}{v_{1,I,J}} - \Sigma_{s0,1\to1,0,I,J} & 0 \\ 0 & \Sigma_{t,2,0,I,J} + \dfrac{i\omega}{v_{2,I,J}} - \Sigma_{s0,2\to2,0,I,J} \end{bmatrix} \tag{4.16}$$

$$\overline{\overline{D}}_{I,J} = \begin{bmatrix} \dfrac{1}{3\left(\Sigma_{t,1,0,I,J} + \dfrac{i\omega}{v_{1,I,J}}\right)} & 0 \\ 0 & \dfrac{1}{3\left(\Sigma_{t,2,0,I,J} + \dfrac{i\omega}{v_{2,I,J}}\right)} \end{bmatrix} \tag{4.17}$$

and

$$\overline{\delta F}^{(n_o+1)}_{I+\frac{1}{2},J+\frac{1}{2}} = \begin{bmatrix} \delta F^{(n_o+1)}_{1,I+\frac{1}{2},J+\frac{1}{2}} \\ \delta F^{(n_o+1)}_{2,I+\frac{1}{2},J+\frac{1}{2}} \end{bmatrix} \tag{4.18}$$

Equation (4.15) also represents a fixed source problem, where the two energy groups are coupled. The calculated $\overline{\delta F}^{(n_o+1)}_{I+1/2,J+1/2}$ are used to correct the scalar neutron noise at cell centers, according to:

$$\overline{\delta\phi}^{(n_o+1)}_{I,J} = \overline{\delta\phi}^{(n_o,N_I)}_{I,J} + \frac{1}{4}\sum_{I'=I}^{I+1}\sum_{J'=J}^{J+1}\overline{\delta F}^{(n_o+1)}_{I'-\frac{1}{2},J'-\frac{1}{2}} \tag{4.19}$$

The new values of $\overline{\delta\phi}_{I,J}^{(n_o+1)}$ obtained at the end of (n_o+1)-th outer iteration are used to update the fission term for the next outer iteration. The DSA scheme for neutron noise calculations is summarized in Algorithm 2.

Algorithm 2: DSA scheme for the dynamic module

```
Begin with $\delta\phi_{l,g,I,J,K}^{m}=0$ and $\delta\psi_{g,n,I,J,K}=0$
    while $\Re^{err}$ $or$ $\Im^{err}$ $>\varepsilon$
        for $g$=1 to $g=2$ do
            for inner iteration count $\leq N_I$ do
                Sweep through the angular directions and spatial domain
                Solve Eq. (4.11) for $\delta f_{g,I+1/2,J+1/2}$
                Adjust scalar noise according to Eq. (4.14) and update self-scattering term
            end for
        end for
        Solve Eq. (4.15) for $\overline{\delta F}_{I+1/2,J+1/2}$
        Adjust scalar noise according to Eq. (4.19) and update both scattering and fission
        source terms
    end while
```

4.1.1 Theoretical convergence rates

The convergence rate of iterative schemes can be studied analytically through the Fourier convergence analysis method. This method has been widely applied to study the convergence behavior of static neutron transport calculations [25], and, to some extent, of time-dependent calculations [26]. In this section, the analytical convergence rate of both the unaccelerated and the DSA scheme is presented for frequency-domain neutron noise calculations. Only the final expression is shown, and more details of the derivation can be found in Paper IV and in [27].

The aim is to derive an error transition matrix, denoted as ς, that describes how fast the error in the approximated solution is reduced between two consecutive iterations and that can be used to estimate the convergence rate, denoted as ϱ. If the predicted ϱ is smaller than 1, the scheme is convergent, otherwise the scheme does not converge. In addition, the smaller ϱ is, the faster the convergence becomes.

The derivation is based on the fully discretized equations (4.1), (4.11) and (4.15). For the unaccelerated scheme, the error transition matrix ς is equal to:

$$\varsigma(\omega,N_I,\boldsymbol{\Theta})=\left[\bar{\bar{I}}-\left(\bar{\bar{I}}-\bar{\bar{P}}\right)^{-1}\left(\bar{\bar{I}}-\bar{\bar{P}}^{N_I}\right)\bar{\bar{Q}}\right]^{-1}\left[\bar{\bar{P}}^{N_I}+\left(\bar{\bar{I}}-\bar{\bar{P}}\right)^{-1}\left(\bar{\bar{I}}-\bar{\bar{P}}^{N_I}\right)\bar{\bar{R}}\right] \qquad (4.20)$$

The matrix depends on the angular frequency of the perturbation ω, the Fourier mode $\boldsymbol{\Theta}$, and the number N_I of inner iterations. The Fourier mode consists of two components Θ_1 and Θ_2 in the x and y directions, respectively, and the two components can take any values in the interval $[-\infty, +\infty]$. In Eq. (4.20), $\bar{\bar{I}}$ is the identity matrix and the other matrix quantities have the following expressions:

$$\bar{\bar{P}} = \bar{\bar{T}}\,\overline{\overline{\Sigma_t^{dyn}}}^{-1}\,\overline{\overline{\Sigma_{ss}}} \tag{4.21}$$

$$\bar{\bar{Q}} = \bar{\bar{T}}\,\overline{\overline{\Sigma_t^{dyn}}}^{-1}\,\overline{\overline{\Sigma_{sd}}} \tag{4.22}$$

$$\bar{\bar{R}} = \bar{\bar{T}}\,\overline{\overline{\Sigma_t^{dyn}}}^{-1}\,\bar{\bar{\chi}}\,\overline{\overline{\nu\Sigma_{\mathrm{f}}}} \tag{4.23}$$

and

$$\bar{\bar{T}} = \sum_{\mathrm{n}=1}^{\mathrm{N_0}} \frac{1}{4}\mathrm{w_n}\left\{\left[2i\frac{\mu_{\mathrm{n}}}{\Delta\mathrm{x}}\tan\left(\Theta_1\frac{\Delta x}{2}\right) + 2i\frac{\eta_{\mathrm{n}}}{\Delta\mathrm{y}}\tan\left(\Theta_2\frac{\Delta y}{2}\right)\right]\overline{\overline{\Sigma_t^{dyn}}}^{-1} + \bar{\bar{I}}\right\}^{-1} \tag{4.24}$$

The convergence rate ϱ of the unaccelerated scheme is determined by taking the largest absolute eigenvalue of the matrix ς, for all possible error modes, i.e.:

$$\varrho(\omega, N_I) = \max_{-\infty<\Theta_1,\Theta_2<+\infty}\left\{abs\left[eig\left(\varsigma(\omega, N_I, \boldsymbol{\Theta})\right)\right]\right\} \tag{4.25}$$

The convergence rate of the DSA scheme for neutron noise calculations is obtained in a similar manner. The error transition matrix is expressed as:

$$\varsigma^{DSA}(\omega, N_I, \boldsymbol{\Theta}) = \left[\bar{\bar{I}} - \left(\bar{\bar{I}} - \overline{\overline{P^D}}\right)^{-1}\left(\bar{\bar{I}} - \overline{\overline{P^D}}\right)\overline{\overline{Q^D}}\right]^{-1}\left[\overline{\overline{P^D}}^{M} + \left(\bar{\bar{I}} - \overline{\overline{P^D}}\right)^{-1}\left(\bar{\bar{I}} - \overline{\overline{P^D}}^{M}\right)\overline{\overline{R^D}}\right] \tag{4.26}$$

with

$$\overline{\overline{P^D}} = \bar{\bar{T}}\,\overline{\overline{\Sigma_t^{dyn}}}^{-1}\,\overline{\overline{\Sigma_{ss}}} + \frac{a^2}{2}\bar{\bar{L}}\left(\bar{\bar{T}}\,\overline{\overline{\Sigma_t^{dyn}}}^{-1}\,\overline{\overline{\Sigma_{ss}}} - \bar{\bar{I}}\right) \tag{4.27}$$

$$\overline{\overline{Q^D}} = \bar{\bar{T}}\,\overline{\overline{\Sigma_t^{dyn}}}^{-1}\,\overline{\overline{\Sigma_{sd}}} + \frac{a^2}{2}\bar{\bar{L}}\bar{\bar{T}}\,\overline{\overline{\Sigma_t^{dyn}}}^{-1}\,\overline{\overline{\Sigma_{sd}}} \tag{4.28}$$

$$\overline{\overline{R^D}} = \bar{\bar{T}}\,\overline{\overline{\Sigma_t^{dyn}}}^{-1}\,\bar{\bar{\chi}}\,\overline{\overline{\nu\Sigma_{\mathrm{f}}}} + \frac{a^2}{2}\bar{\bar{L}}\bar{\bar{T}}\,\overline{\overline{\Sigma_t^{dyn}}}^{-1}\,\bar{\bar{\chi}}\,\overline{\overline{\nu\Sigma_{\mathrm{f}}}} \tag{4.29}$$

and

$$\bar{\bar{L}} = \Delta x\Delta y\left[4\frac{\Delta y}{\Delta x}\bar{\bar{D}}(1 - \cos\Theta_1\Delta x) + 4\frac{\Delta x}{\Delta y}\bar{\bar{D}}(1 - \cos\Theta_2\Delta y) + 2\overline{\overline{\Sigma_R}}\Delta x\Delta y\right]^{-1}\overline{\overline{\Sigma_{ss}}} \tag{4.30}$$

$$a = \cos\left(\frac{\Theta_1\Delta x}{2} + \frac{\Theta_2\Delta y}{2}\right) + \cos\left(\frac{\Theta_1\Delta x}{2} - \frac{\Theta_2\Delta y}{2}\right) \tag{4.31}$$

The convergence rate of the DSA scheme ϱ^{DSA} is estimated by:

$$\varrho^{DSA}(\omega, N_I) = \max_{-\infty<\Theta_1,\Theta_2<+\infty}\left\{abs\left[eig\left(\varsigma^{DSA}(\omega, N_I, \boldsymbol{\Theta})\right)\right]\right\} \tag{4.32}$$

4.1.2 Convergence analysis

The convergence properties of the unaccelerated and DSA algorithms are investigated with respect to the number of inner iterations and the frequency of the neutron noise source. In addition, the theoretical and numerical values of the convergence rates are compared. The comparison can also serve as a verification of the correct implementation of the algorithms.

A problem that consists of a neutron noise source (namely, an absorber of variable strength) in a two-dimensional homogeneous system is used. The amplitude of the noise source is arbitrarily chosen equal to unity since it does not influence the convergence, but the frequency may vary. The two-energy group neutron cross sections and the kinetics parameters of the system are taken from [14]. The spatial domain is discretized using a 30×30 square mesh, in which the size of one computational cell is such that $\Delta x = \Delta y = 1\ cm$. For the angular discretization, S_8 level symmetric quadrature set is used. The boundary conditions are reflective, so the system can be considered infinite.

The theoretical predictions of the convergence rates are calculated with Eqs. (4.25) and (4.32). The numerical convergence rates ϱ^{num} are obtained from the calculations of NOISE-SN using:

$$\varrho^{num} = \frac{\left\|\overline{\overline{\delta\phi}}^{(n_o+1)} - \overline{\overline{\delta\phi}}^{(n_o)}\right\|_2}{\left\|\overline{\overline{\delta\phi}}^{(n_o)} - \overline{\overline{\delta\phi}}^{(n_o-1)}\right\|_2} \tag{4.33}$$

where $\|\cdot\|_2$ is the Euclidean norm, and $\overline{\overline{\delta\phi}}^{(n_o+1)}$, $\overline{\overline{\delta\phi}}^{(n_o)}$ and $\overline{\overline{\delta\phi}}^{(n_o-1)}$ are column-vectors that contain the simulated scalar neutron noise in all spatial points for both energy groups, at iterations $(n_o + 1)$, (n_o) and $(n_o - 1)$.

Dependence of the convergence rate on the number of inner iterations

The change in convergence rate with different numbers of inner iterations is analyzed with a perturbation frequency of 1 Hz. For both DSA-based and unaccelerated schemes, the convergence rates are calculated analytically and numerically with varying numbers of N_I and are compared in Fig. 4.1.

The numerical performances of the two algorithms are consistent with the theoretical predictions. As expected, the unaccelerated scheme converges faster (fewer number of outer iterations required) with more inner iterations performed, but its values of ϱ are very close to one, indicating extremely slow convergence. On the other hand, the convergence rate for the accelerated scheme is lower and is not influenced by N_I, even though it does not differ significantly from unity. Similar results are found at other frequencies, as discussed in Paper IV.

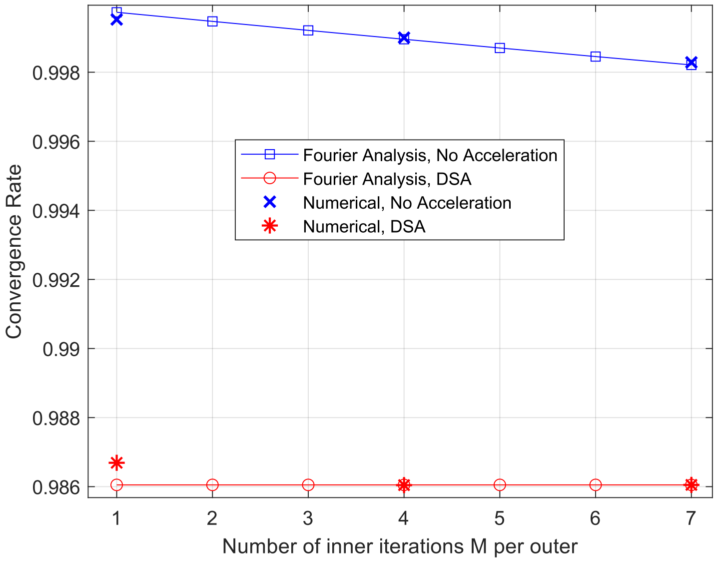

Figure 4.1 Convergence rate as a function of the number of inner iterations N_I for the unaccelerated and DSA schemes

Dependence of the convergence rate on the frequency of the neutron noise source

The convergence rate is studied by varying the frequency of the perturbation and fixing the number of inner iterations N_I to 1. In Fig. 4.2, the convergence rate is plotted against the frequency.

The theoretical prediction agrees well with the numerical values. A plateau region is found between ~0.1 Hz and ~100 Hz, where the convergence is rather insensitive to the frequency. This finding is consistent with the properties of the zero-power reactor transfer function, whose amplitude and phase are approximately constant in the plateau region (see Section 2.4). Below the frequencies of the plateau region, the convergence rate increases largely with decreasing frequency, and the convergence becomes slow. Above the frequencies of the plateau region, the convergence rate decreases with increasing frequency, and the decreasing trend is more remarkable for the accelerated scheme. For other values of N_I, the same behavior of ϱ with respect to frequency is observed, see details in Paper IV. According to the convergence analysis, DSA improves the numerical performances of the computational scheme. However, the number of iterations required for convergence might still be high.

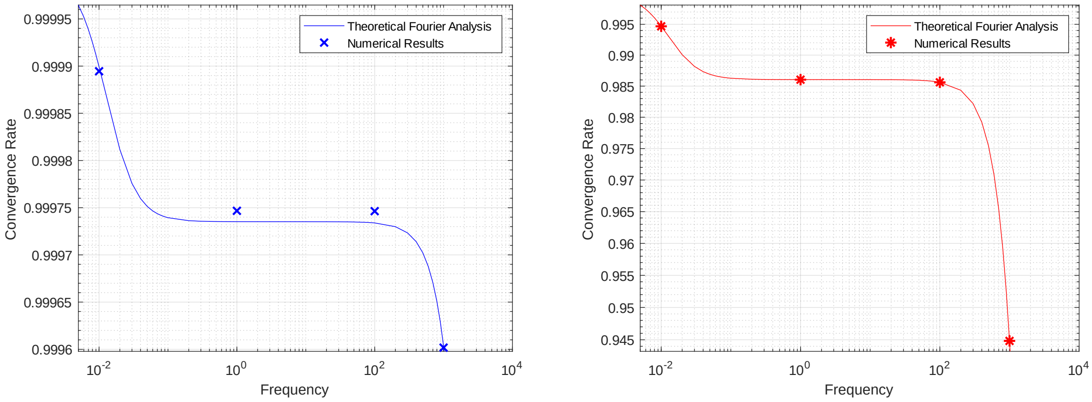

Figure 4.2 Convergence rate as a function of frequency for the unaccelerated scheme (left) and for the DSA scheme (right)

4.2 Coarse Mesh Finite Difference Acceleration

The CMFD method has been demonstrated to accelerate both higher-order deterministic [28,29] and Monte Carlo transport calculations [30]. It is mainly used for static eigenvalue calculations and, to some extent, for static fixed source problems [31], and time-dependent transient calculations [32]. In this work, the CMFD acceleration is investigated for frequency-domain neutron noise calculations.

The CMFD method updates the quantities obtained from the transport sweep via the solution of a low-order equation, usually over a coarser mesh. The low-order equation is derived such that the heterogenous transport solution is preserved.

The CMFD method is very efficient to remove slow converging components of the numerical error, but its biggest drawback is related to the conditional convergence property. In problems where the coarse mesh size and the value of total cross section are relatively large, numerical instabilities may occur and lead to failure in convergence [33, 34].

Variants of the original CMFD method have been developed to obtain unconditional convergence behavior. An example of such variants is, for instance, pCMFD, i.e., the partial current-based CMFD [35]. Compared to the normal method, pCMFD solves a slightly different set of low-order linear equations, which leads to stable convergence properties. However, for specific problems, pCMFD may need more iterations to converge. More recently, based on the Fourier convergence analysis, the artificial diffusion CMFD (adCMFD) [36] and the optimally diffusive CMFD (odCMFD) [37] methods were proposed. Both methods modify the diffusion coefficient with an additional term. In adCMFD the additional term is fixed, while in odCMFD it may vary depending on the mesh and the problem to be solved. They have shown better convergence properties than the original CMFD method and the pCMFD method. Another variant of the CMFD method is the Linear Prolongation CMFD (lpCMFD) method [38], in which the update process is modified. In NOISE-SN, the regular CMFD, adCMFD and lpCMFD methods are implemented.

4.2.1 CMFD formulation for neutron noise calculation

The basic CMFD-accelerated scheme developed in NOISE-SN for frequency-domain, 3-dimensional, multi-energy group neutron noise calculations is described. The scheme is also discussed in Paper I.

A full iteration consists of the transport inner-outer iterative process (discussed in Section 3.3) together with the solution of the lower-order CMFD equation. The neutron noise estimated in a sequence of inner-outer iterations is used to construct the CMFD equation over a coarser grid. The solution of the low-order problem then provides a correction of the neutron noise for the next full iteration.

One generic full iteration is identified by the index $ITE+1$, while the associated inner-outer transport iteration by $ITE+1/2$. In the fine mesh used for the transport problem, one cell is characterized by its position indices (I,J,K). In the coarse mesh for the CMFD equation, the position indices of a cell are (IC,JC,KC).

The CMFD equation can be derived from Eq. (3.10) by applying the operations $\sum_n w_n(\cdot)$ and $\sum_{(I,J,K)\in(IC,JC,KC)} V_{I,J,K}(\cdot)$ to both sides of the equation. The operation $\sum_n w_n(\cdot)$ represents an integration over the angular variable using a quadrature set and the operation $\sum_{(I,J,K)\in(IC,JC,KC)} V_{I,J,K}(\cdot)$ represents a homogenization process from the fine mesh (used for the transport calculation) to a coarser mesh. Then, the CMFD equation discretized over the coarse mesh and solved within the full $ITE+1$-th iteration is:

$$\begin{aligned}
&\frac{1}{\Delta X_{IC}}\left(J^{x,ITE+1}_{g,IC+1/2,JC,KC}-J^{x,ITE+1}_{g,IC-1/2,JC,KC}\right)+\frac{1}{\Delta Y_{JC}}\left(J^{y,ITE+1}_{g,IC,JC+1/2,KC}-J^{y,ITE+1}_{g,IC,JC-1/2,KC}\right)\\
&+\frac{1}{\Delta Z_{KC}}\left(J^{z,ITE+1}_{g,IC,JC,KC+1/2}-J^{z,ITE+1}_{g,IC,JC,KC-1/2}\right)+\Sigma^{dyn,ITE+1}_{t,g,IC,JC,KC}\delta\Phi^{CMFD,ITE+1}_{g,IC,JC,KC}\\
&=\sum_{g'}\Sigma^{ITE+1}_{s,g'\to g,IC,JC,KC}\delta\Phi^{CMFD,ITE+1}_{g',IC,JC,KC}\\
&+\frac{1}{k_{eff}}\chi^{dyn,ITE+1}_{g,IC,JC,KC}\sum_{g'}\nu\Sigma^{ITE+1}_{f,g',IC,JC,KC}\delta\Phi^{CMFD,ITE+1}_{g',IC,JC,KC}+S_{g,IC,JC,KC}
\end{aligned}\tag{4.34}$$

The unknown to be determined from the CMFD equation is the scalar quantity $\delta\Phi^{CMFD,ITE+1}_{g,IC,JC,KC}$.

To obtain a CMFD solution that can accelerate the discrete ordinates scheme, the treatment of the current and the calculations of the group constants appearing in Eq. (4.34) need to preserve the heterogeneous transport solution. The currents related to the surfaces of the coarse cells, $J^{x,ITE+1}_{g}$, $J^{y,ITE+1}_{g}$ and $J^{z,ITE+1}_{g}$ are approximated using the Fick's Law with a transport correction term. For instance, the current in the x-direction is given as:

$$\begin{aligned}
J^{x,ITE+1}_{g,IC+1/2,JC,KC}=&-\widetilde{D}_{g,IC+1/2,JC,KC}\left(\delta\Phi^{CMFD,ITE}_{g,IC+1,JC,KC}-\delta\Phi^{CMFD,ITE}_{g,IC,JC,KC}\right)\\
&-\widehat{D}_{g,IC+1/2,JC,KC}\left(\delta\Phi^{CMFD,ITE}_{g,IC+1,JC,KC}+\delta\Phi^{CMFD,ITE}_{g,IC,JC,KC}\right)
\end{aligned}\tag{4.35}$$

Similar relationships are written for the other directions. Following the standard CMFD formulation, the coupling coefficient $\widetilde{D}$ and the correction factor $\widehat{D}$ in Eq. (4.35) are respectively expressed as:

$$\widetilde{D}_{g,IC+1/2,JC,KC} = \frac{2D_{g,IC+1,JC,KC}D_{g,IC,JC,KC}}{\Delta X_{IC+1}D_{g,IC,JC,KC} + \Delta X_{IC}D_{g,IC+1,JC,KC}} \tag{4.36}$$

$$\widehat{D}_{g,IC+1/2,JC,KC} = -\frac{J^{x,ITE+1/2}_{g,IC+1/2,JC,KC} + \widetilde{D}_{g,IC+1/2,JC,KC}\left(\delta\Phi^{ITE+1/2}_{g,IC+1,JC,KC} - \delta\Phi^{ITE+1/2}_{g,IC,JC,KC}\right)}{\delta\Phi^{ITE+1/2}_{g,IC+1,JC,KC} + \delta\Phi^{ITE+1/2}_{g,IC,JC,KC}} \tag{4.37}$$

The coarse mesh diffusion coefficients in Eq. (4.36) are calculated using the fine mesh static fluxes $\phi^{m=0}_{l=0,g,I,J,K,0}$, i.e.:

$$D_{g,IC,JC,KC} = \frac{\sum_{(I,J,K)\in(IC,JC,KC)} \phi^{m=0}_{l=0,g,I,J,K,0}V_{I,J,K}}{3\sum_{(I,J,K)\in(IC,JC,KC)} \Sigma_{t,g,0,I,J,K}\phi^{m=0}_{l=0,g,I,J,K,0}V_{I,J,K}} \tag{4.38}$$

In Eq. (4.37), the quantities $J^{x,ITE+1/2}_{g,IC+1/2,JC,KC}$ and $\delta\Phi^{ITE+1/2}_{g,IC+1,JC,KC}$ are computed based on the transport estimation obtained from the $ITE+1/2$-th inner-outer iteration within the full $ITE+1$-th iteration. The coarse mesh scalar neutron noise $\delta\Phi^{ITE+1/2}_{g,IC+1,JC,KC}$ is homogenized according to:

$$\delta\Phi^{ITE+\frac{1}{2}}_{g,IC+1,JC,KC} = \frac{\sum_{(I,J,K)\in(IC,JC,KC)} \delta\phi^{m=0,ITE+\frac{1}{2}}_{l=0,g,I,J,K}V_{I,J,K}}{\sum_{(I,J,K)\in(IC,JC,KC)} V_{I,J,K}} \tag{4.39}$$

The current on the surface of the coarser mesh $J^{x,ITE+1/2}_{g,IC+1/2,JC,KC}$ is computed by:

$$J^{x,ITE+\frac{1}{2}}_{g,IC+\frac{1}{2},JC,KC} = \frac{\sum_{(J,K)\in(JC,KC)} \sum_{n'} \left(w_{n'}\mu_{n'}\delta\psi^{ITE+\frac{1}{2}}_{g,n',I+\frac{1}{2},J,K}\Delta y_J\Delta z_K\right)}{\sum_{(J,K)\in(JC,KC)} \Delta y_J\Delta z_K} \tag{4.40}$$

The coarse mesh group constants are also evaluated on the fly during each iteration, using the scalar neutron noise $\delta\phi^{m=0,ITE+1/2}_{l=0,g,I,J,K}$, i.e.:

$$\Sigma^{dyn,ITE+1}_{t,g,IC,JC,KC} = \frac{\sum_{(I,J,K)\in(IC,JC,KC)} \left(\Sigma_{t,g,0,I,J,K} + \frac{i\omega}{v_{g,I,J,K}}\right)\delta\phi^{m=0,ITE+1/2}_{l=0,g,I,J,K}V_{I,J,K}}{\sum_{(I,J,K)\in(IC,JC,KC)} \delta\phi^{m=0,ITE+1/2}_{l=0,g,I,J,K}V_{I,J,K}} \tag{4.41}$$

$$\Sigma^{ITE+1}_{s,g\to g',IC,JC,KC} = \frac{\sum_{(I,J,K)\in(IC,JC,KC)} \Sigma_{s0,g\to g',0,I,J,K}\delta\phi^{m=0,ITE+1/2}_{l=0,g,I,J,K}V_{I,J,K}}{\sum_{(I,J,K)\in(IC,JC,KC)} \delta\phi^{m=0,ITE+1/2}_{l=0,g,I,J,K}V_{I,J,K}} \tag{4.42}$$

$$\nu\Sigma_{f,g,IC,JC,KC}^{ITE+1} = \frac{\sum_{(I,J,K)\in(IC,JC,KC)} \nu\Sigma_{f,g,0,I,J,K}\,\delta\phi_{l=0,g,I,J,K}^{m=0,ITE+1/2} V_{I,J,K}}{\sum_{(I,J,K)\in(IC,JC,KC)} \delta\phi_{l=0,g,I,J,K}^{m=0,ITE+1/2} V_{I,J,K}} \qquad (4.43)$$

The preparation of fission spectrum term is more involved and is given as:

$$\bar{\chi}_{g,IC,JC,KC}^{dyn,ITE+1} = \frac{\sum_{(I,J,K)\in(IC,JC,KC)} \sum_{g'=1}^{G} \chi_{g,I,J,K}^{dyn} \nu\Sigma_{f,g',0,I,J,K} V_{I,J,K}\,\delta\phi_{l=0,g,I,J,K}^{m=0,ITE+\frac{1}{2}}}{\sum_{(I,J,K)\in(IC,JC,KC)} \sum_{g'=1}^{G} \nu\Sigma_{f,g',0,I,J,K} V_{I,J,K}\,\delta\phi_{l=0,g,I,J,K}^{m=0,ITE+\frac{1}{2}}} \qquad (4.44)$$

The source term is calculated in the scalar form:

$$S_{g,I,J,K}(\omega) = -\delta\Sigma_{t,g,I,J,K}(\omega)\phi_{l=0,g',I,J,K,0}^{m=0} + \sum_{g'} \delta\Sigma_{s0,g'\to g,I,J,K}(\omega)\phi_{l=0,g',I,J,K,0}^{m=0}$$

$$+\frac{1}{k_{eff}}\chi_{g,I,J,K}^{dyn} \sum_{g'} \nu\delta\Sigma_{f,g',I,J,K}(\omega)\phi_{l=0,g',I,J,K,0}^{m=0} \qquad (4.45)$$

Then the homogenization over the coarser mesh is performed:

$$S_{g,IC,JC,KC} = \frac{\sum_{(I,J,K)\in(IC,JC,KC)} S_{g,I,J,K} V_{I,J,K}}{\sum_{(I,J,K)\in(IC,JC,KC)} V_{I,J,K}} \qquad (4.46)$$

An equivalent CMFD equation to the transport equation is thus derived and takes the form of a finite differenced diffusion equation. From the spatial discretization, a system of linear equations is constructed and solved using a suitable numerical method, e.g., LU decomposition. The results of the CMFD problem are used to update the fine-mesh noise moments $\delta\phi_{l,g,I,J,K}^{m}$ in the inner-outer iterations, as:

$$\delta\phi_{l,g,I,J,K}^{m,ITE+1} = \delta\phi_{l,g,I,J,K}^{m,ITE+\frac{1}{2}} \frac{\delta\Phi_{g,IC,JC,KC}^{CMFD,ITE+1}}{\delta\Phi_{g,IC,JC,KC}^{ITE+\frac{1}{2}}} \qquad for\ (I,J,K) \in (IC,JC,KC) \qquad (4.47)$$

When reflective conditions are specified at the boundaries of the system, the incoming angular neutron noise is also updated. For instance, if a reflective boundary condition is imposed at the surface with $x = 1/2$, then the angular flux for incoming directions is updated according to:

$$\delta\psi_{g,n_{in},\frac{1}{2},J,K}^{ITE+1} = \delta\psi_{g,n_{out},\frac{1}{2},J,K}^{ITE+\frac{1}{2}} \frac{\delta\Phi_{g,1,JC,KC}^{CMFD,ITE+1}}{\delta\Phi_{g,1,JC,KC}^{ITE+\frac{1}{2}}} \qquad for\ (J,K) \in (JC,KC) \qquad (4.48)$$

The inward direction n_{in} is the reflected direction of the outward direction n_{out} at the surface.

In this framework, the neutron noise quantities are calculated as complex values and they can be expressed in terms of amplitude and phase. The update process based on Eqs. (4.47) and

(4.48) is equivalent to rescale the amplitude of the noise and adjust linearly the phase. For instance, Eq. (4.47) can be rewritten as:

$$\left|\delta\phi^{m,ITE+1}_{l,g,I,J,K}\right| e^{i\cdot arg\left(\delta\phi^{m,ITE+1}_{l,g,I,J,K}\right)} = \left|\delta\phi^{m,ITE+\frac{1}{2}}_{l,g,I,J,K}\right| \frac{\left|\delta\Phi^{CMFD,ITE+1}_{g,IC,JC,KC}\right|}{\left|\delta\Phi^{ITE+\frac{1}{2}}_{g,IC,JC,KC}\right|} e^{i\cdot\left[arg\left(\delta\phi^{m,ITE+\frac{1}{2}}_{l,g,I,J,K}\right)+arg\left(\delta\Phi^{CMFD,ITE+1}_{g,IC,JC,KC}\right)-arg\left(\delta\Phi^{ITE+\frac{1}{2}}_{g,IC,JC,KC}\right)\right]} \quad (4.49)$$

where $|\cdots|$ and $arg(\cdots)$ denote the amplitude and the phase of the complex neutron noise, respectively.

The overall performance of the CMFD-accelerated scheme can be further improved as follows:

- For the initial transport iteration, a diffusion guess can be obtained from the solution of the CMFD equation with the correction factor $\widehat{D}$ equal to zero and with the coarse-mesh group constants evaluated from the static flux.
- The CMFD equation can be solved over the fine transport mesh (at the expense of requiring larger computational resources) instead of choosing a coarser mesh. This is beneficial since, according to the convergence analysis, a finer mesh can result in a more rapid and, in some cases, a more stable convergence of the CMFD calculation.

The CMFD-accelerated scheme for neutron noise calculations is summarized in Algorithm 3.

Algorithm 3: CMFD scheme for frequency-domain neutron noise calculations

```
Begin with initial CMFD guess by solving Eq. (4.34) with $\widehat{D} = 0$
    while $\Re^{err}$ or $\Im^{err} > \varepsilon$
        for outer iteration count ≤ $N_O$ do
            for $g$=1 to $g = G$ do
                for inner iteration count ≤ $N_I$ do
                    Sweep through the angular directions and spatial domain
                    Update moments and self-scattering term
                end for
            end for
            Update fission source term
        end for
        Solve Eq. (4.34) for $\delta\Phi^{CMFD}_{g',IC,JC,KC}$
        Adjust noise moments and incoming angular flux according to Eqs. (4.47) and
        (4.48), update both the scattering and fission source term
    end while
```

4.2.2 Artificial Diffusion CMFD

The artificial diffusion CMFD (adCMFD) method is a modified version of the regular CMFD method, which aims at obtaining an unconditional stable behavior [36]. This method is implemented in NOISE-SN and tested for neutron noise calculations in the frequency domain. The method is such that the coupling coefficient $\widetilde{D}$ given in Eq. (4.36) is artificially increased by 1/4, i.e.:

$$\widetilde{D}_{g,IC+1/2,JC,KC} = \frac{2D_{g,IC+1,JC,KC}D_{g,IC,JC,KC}}{\Delta X_{IC+1}D_{g,IC,JC,KC} + \Delta X_{IC}D_{g,IC+1,JC,KC}} + \frac{1}{4} \tag{4.50}$$

The standard CMFD equations with these modified coupling coefficients are algebraically equivalent to the pCMFD equations, and the stable convergence behavior of the pCMFD method may be emulated.

4.2.3 Linear Prolongation CMFD method

The lpCMFD method is another available option to improve the stability of the convergence of CMFD [38]. The implementation in NOISE-SN is such that the method can only be applied to two-dimensional problems and to the calculation of the scalar neutron noise, i.e., the zeroth moment neutron noise $\delta\phi_{l=0,g,I,J,K}^{m=0,ITE+1}$.

According to this method, the update process is modified using a linear additive approach similar to DSA. Eq. (4.47) is then replaced with:

$$\delta\phi_{l=0,g,I,J}^{m=0,ITE+1} = \delta\phi_{l,g,I,J}^{m,ITE+\frac{1}{2}} + \delta\phi_{g,I,J}^{CORR,ITE+\frac{1}{2}} \tag{4.51}$$

The correction quantity at the centers of the fine cells $\delta\phi_{g,I,J}^{CORR,ITE+\frac{1}{2}}$ is obtained by bilinear interpolation of the differences between the CMFD solution and the homogenized transport solution at the vertices of the coarser mesh. These differences are calculated, e.g., as:

$$\delta\phi_{g,I+\frac{1}{2},J+\frac{1}{2}}^{DIFF,ITE+\frac{1}{2}} = \frac{1}{4}\sum_{IC=IC}^{IC+1}\sum_{JC=JC}^{JC+1}\left(\delta\Phi_{g,IC,JC}^{CMFD,ITE+1} - \delta\Phi_{g,IC,JC}^{ITE+\frac{1}{2}}\right) \tag{4.52}$$

The details of the bilinear interpolation and the treatment of reflective boundaries are given in [38].

4.2.4 Stabilization of the CMFD algorithm

To better stabilize the CMFD algorithm, two procedures are used in this work. The first is to increase the number of inner and outer transport iterations before each CMFD calculation. The second is to under-relax the CMFD update of the fine-mesh transport solutions.

Following the under-relaxation approach, a factor θ that can vary between zero and unity is introduced in Eq. (4.47) and Eq. (4.48). For example, Eq. (4.47) is modified as:

$$\delta\phi_{l,g,I,J,K}^{m,ITE+1} = (1-\theta)\delta\phi_{l,g,I,J,K}^{m,ITE+\frac{1}{2}} + \theta\delta\phi_{l,g,I,J,K}^{m,ITE+\frac{1}{2}} \frac{\delta\Phi_{g,IC,JC,KC}^{CMFD,ITE}}{\delta\Phi_{g,IC,JC,KC}^{ITE+\frac{1}{2}}} \tag{4.53}$$

The unaccelerated scheme is obtained when $\theta = 0$. The standard CMFD update is recovered when $\theta = 1$.

4.3 Comparison of the acceleration methods

The convergence of the iterative schemes implemented in NOISE-SN is compared based on two neutron noise problems defined in the C3 and C4V benchmark configurations. In this section, only the convergence properties are presented, following the discussion in Paper III. The numerical results of both problems can be found in, e.g., Paper IV and Paper V.

Both C3 and C4V systems consist of a 2×2 assembly arrangement. Two UO2 assemblies are located North-West and South-East and two MOX assemblies are located North-East and South-West [39]. Each fuel assembly contains 17×17 squares that represent homogenized fuel cells or guide tubes. The C3 test case has reflective boundary conditions on all sides of the system, while the C4V test case has both reflective and vacuum boundary conditions. The macroscopic cross sections are given for two-energy groups.

In both the C3 and C4V systems, the neutron noise source is assumed to be a stationary fluctuation of the capture cross section in both energy groups. The source is placed at the fuel cell with position indexes (16,19), in the North-East MOX fuel assembly. The amplitude of the perturbation is taken equal to 5% of the nominal values of the capture cross section in each energy group. The frequency of the perturbation is set to 1 Hz. In addition, a homogeneous β value equal to 0.0049 and a λ value equal to 0.0797 s^{-1} are chosen. The layout of the benchmark problems with the location of the noise source shown in red is given in Fig. 4.3.

In the calculations presented in this section, the transport sweeps are carried out over a fine mesh in which each fuel cell of size 1.26×1.26 cm is discretized with 3×3 equally sized squares, and a Level-symmetric S8 quadrature set is applied. Numerical tests with other orders of discrete ordinates such as S16 and S20, lead to similar convergence behavior. For the CMFD calculations, the coarse mesh size corresponds to the size of each fuel cell. The convergence tolerance ε is set to 10^{-6} for both static and neutron noise calculations.

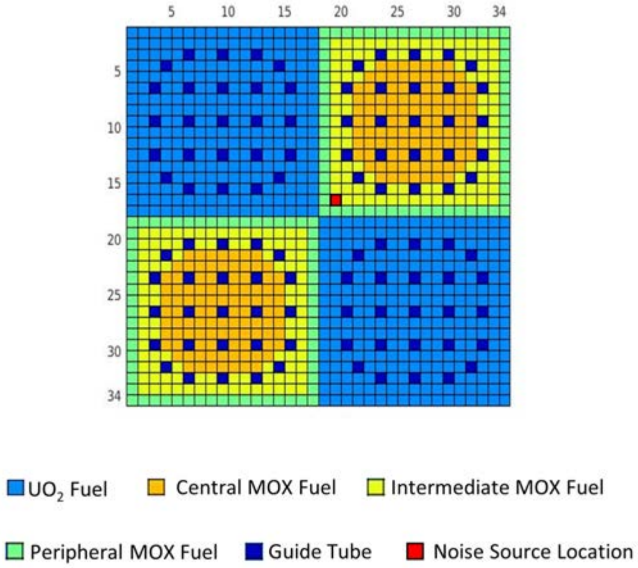

Figure 4.3 System configuration of C3 and C4V benchmark problems and location of the neutron noise source (in red)

4.3.1 Static calculations

The static calculations in C4V configuration are performed with the unaccelerated scheme, the DSA method, and the adCMFD method with one inner-one outer transport iteration (denoted as adCMFD(1)). For the C3 configuration, an additional one inner-two outer adCMFD(2) calculation is performed. The effective multiplication factor k_{eff} obtained from the different simulations are compared with the reference values (taken from [39]) in Table 4.1. The algorithms estimate similar results and the differences with the reference are small, i.e., a maximum difference of 23 pcm is found for the C3 configuration and a maximum of 24 pcm for the C4V system. The static fluxes computed by the different schemes are also in good agreement and the maximum difference between the results is less than 0.3%.

Table 4.1 effective multiplication factor k_{eff} calculated by the static module

Problem	No Acceleration	DSA	adCMFD(1)	adCMFD(2)	Reference
C4V	0.91744	0.91743	0.91734	--	0.91720
C3	1.01801	1.01801	1.01788	1.01772	1.01795

The number of total transport sweeps required for each group to reach the convergence criterion is given in Table 4.2. The maximum relative differences between the scalar flux computed in two consecutive iterations are plotted in Fig. 4.4.

In the C4V system, both DSA and the CMFD methods significantly decrease the iteration number. However, in the C3 system, the adCMFD scheme suffers from some instabilities when approaching the convergence criterion. As observed in Table 4.2 and Fig. 4.4, the convergence of the adCMFD scheme can be improved by performing more transport sweeps before the CMFD calculation and update step.

Table 4.2 Number of transport sweeps in each group required for convergence of the static C3 and C4V calculations

Problem	No Acceleration	DSA	adCMFD(1)	adCMFD(2)
C4V	473	58	15	--
C3	384	34	212	86

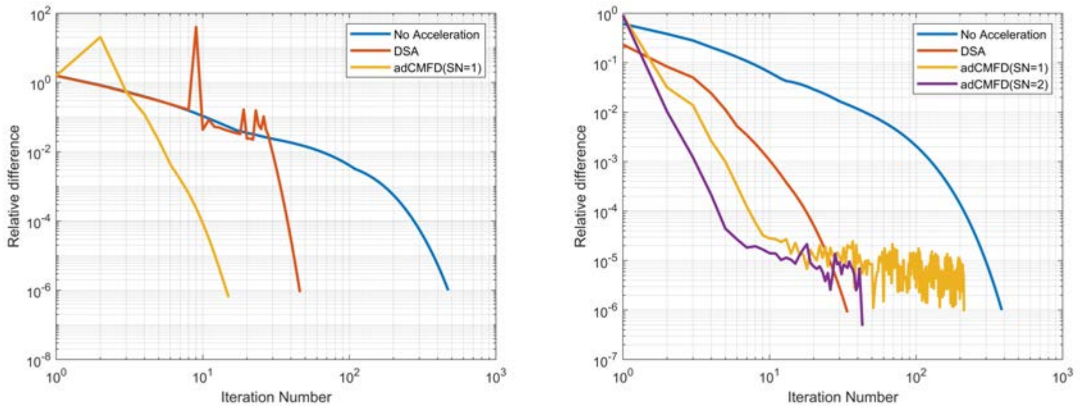

Figure 4.4 Convergence of the static calculation for C4V (left) and C3 (right) systems

4.3.2 Neutron noise calculation in C4V

The frequency-domain neutron noise calculations in the C4V system are accelerated by:

- the DSA method with one inner iteration,
- the original CMFD method with one inner-one outer iteration (CMFD(1)),
- the original CMFD method with one inner-two outer iteration (CMFD(2)),
- the adCMFD method with one inner-one outer iteration (adCMFD),
- the lpCMFD method with one inner-one outer iteration (lpCMFD).

The number of transport sweeps in each group required for convergence is reported in Table 4.3. Compared to the static calculations, the unaccelerated scheme requires a very high number of iterations for the frequency domain neutron noise calculations. The DSA method reduces the iterations by a factor of almost 20, but it still takes more than 1000 iterations to converge. The CMFD methods outperform the DSA method and allow to decrease the number of iterations to less than 50. The maximum pointwise relative difference between the real and imaginary parts of the scalar neutron noise computed in two consecutive iterations is plotted in Fig. 4.5.

Table 4.3 C4V system - Acceleration of frequency domain neutron noise calculation with DSA and CMFD methods

Acceleration Method	No Acceleration	DSA	CMFD (1)	CMFD (2)	adCMFD (1)	lpCMFD
Number of transport sweeps	22655	1262	12	14	18	44

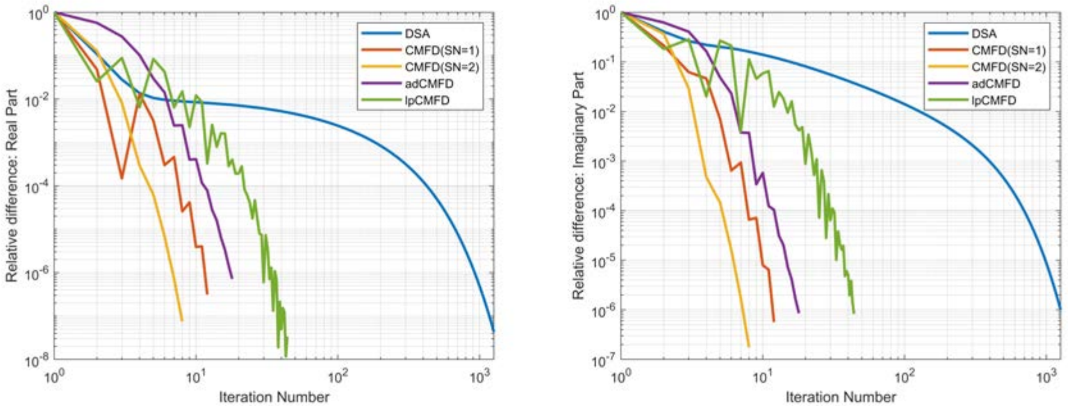

Figure 4.5 C4V system - Convergence of the real (left) and imaginary (right) part of the calculated neutron noise

4.3.3 Neutron noise calculation in C3

Instabilities in the simulation of the C3 system are observed. Thus, additional calculations are performed in which the update process in CMFD(1) is under-relaxed, with θ being 0.5 and 0.18. The number of total transport sweeps required for each group to reach the convergence criterion is given in Table 4.4. The convergence of the real and imaginary parts for this case is shown in Fig. 4.6.

Similar to the static calculations, due to the different boundary conditions, the CMFD methods suffer from instabilities in the C3 system when approaching the convergence criterion of 10^{-6}. The stability can be enhanced using stabilization techniques and methods.

Despite the instabilities, the neutron noise calculated in both the C3 and C4V systems with different schemes provided consistent results. A maximum difference of less than 0.1% is found for both systems.

Table 4.4 C3 system - Acceleration of frequency-domain neutron noise calculation with DSA and CMFD methods

Acceleration Method	Number of transport sweeps
No Acceleration	22877
DSA	1228
CMFD (1)	242
CMFD (2)	180
adCMFD	298
lpCMFD	51
CMFD ($\theta = 0.5$)	116
CMFD ($\theta = 0.18$)	73

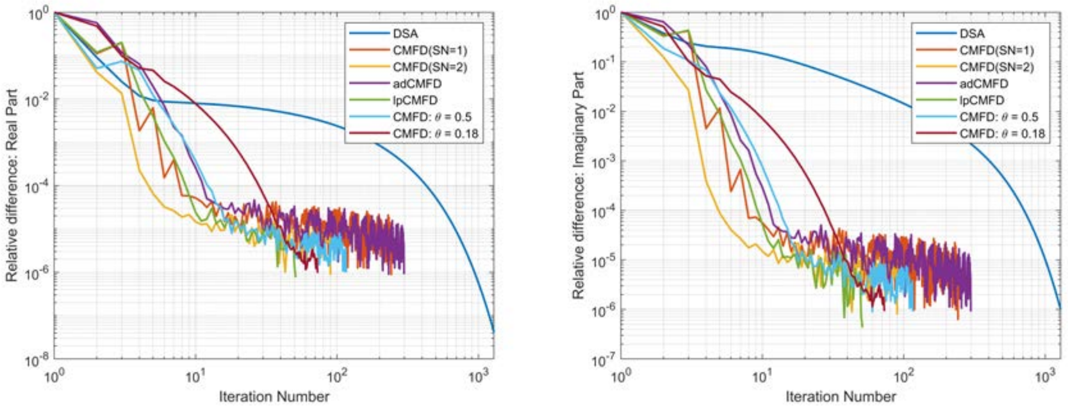

Figure 4.6 C3 system - Convergence of the real (left) and imaginary (right) part of the calculated neutron noise

4.3.4 Dependence on the frequency of the perturbation

As discussed in Section 4.1, the convergence rate of the unaccelerated and DSA schemes is affected by the frequency of the noise source. Therefore, the behavior of the CMFD methods is also investigated for different values of this parameter. For the C4V system, the original CMFD(1) calculation is selected, while for the C3 system, the lpCMFD is used since it leads to the fastest convergence rate. The total number of transport sweeps necessary for convergence are summarized in Table 4.5.

Table 4.5 Number of transport sweeps of the CMFD method for different frequencies of the noise source

Frequency [Hz]	0.001	0.01	1	100	1000
C4V	16	12	12	12	18
C3	640	51	51	118	--

For the C4V system, the acceleration effect provided by the standard CMFD method is merely influenced by the frequency of the noise source. A good performance is also obtained at extremely low frequencies, which have been found to be numerically challenging for the DSA method. For example, the DSA method would require more than 3000 iterations at 0.001 Hz.

In the C3 case, the lpCMFD method performs well in the plateau region with frequencies ranging from 0.01 to 100 Hz. However, when the frequency is outside the plateau region, the acceleration deteriorates. For very high frequencies (e.g., 1000 Hz), all CMFD methods failed to converge.

Chapter 5

Ray effects in neutron noise calculations

In Section 5.1, the issue of ray effect in the discrete ordinates method is introduced. In Section 5.2, the fictitious source method implemented in NOISE-SN for the mitigation of ray effect is described. In Section 5.2 and Section 5.3, two neutron noise problems are used to investigate the impact of the order of discrete ordinates and of the fictitious source method on the mitigation of possible ray effects. The discussion is based on Paper I.

5.1 Ray effect

The ray effect is a well-known numerical issue of the discrete ordinates method. It may cause unphysical distortions of the calculated spatial distribution of the scalar and angular flux. The cause of ray effect is due to the discrete ordinates formulation itself. Although the neutrons can travel in all possible directions within a system, the discrete ordinates method is such that the neutron flux is only evaluated along a discrete number of directions. If the number of discrete directions is taken too small as compared to the number of spatial regions, the angular and scalar fluxes may not be accurate or even correct. Previous analyses (e.g., [40]) has shown that ray effects are most severe for problems where localized sources are present or where the effect of scattering is small.

The possible distortions can be reduced without the modification of the basic S_N equations. One strategy is to increase the number of discrete directions used in the S_N calculations, but it may lead to a significant increase in the computational effort. Alternatively, the angular flux can be computed by averaging or interpolating differently oriented, relatively low-ordered quadrature sets to obtain more accurate solutions [41, 42]. Mitigation of ray effect can also be achieved using advanced quadrature sets [43].

Another approach that can be followed to minimize the issue of ray effect is to solve a different version of the S_N equations. Previous works explored the use of an angular discretization based on the angular finite element method [44] or the addition of a fictious source term in the equations. In the second case, the fictitious source term is designed to transform the S_N equations to spherical harmonic-like equations that preserve the rotational invariance of the transport equation [45, 46, 47]. This method can be integrated into the standard sweeping procedure without significant changes, but the resulting calculations usually require significantly more iterations to converge.

The investigation of ray effect and its mitigation has been mainly focused on real-valued static and time-dependent calculations. In the current research, the impact of the order of discrete ordinates and the application of a fictitious source method is studied for complex-valued neutron noise calculations.

5.2 Fictitious source method in NOISE-SN

The two-dimensional fully discretized S_N equation with a fictitious source for ray effect mitigation can be written as:

$$
\begin{aligned}
&\frac{\mu_n}{\Delta x_I}\left[\delta\psi_{g,n,I+1/2,J}(\omega) - \delta\psi_{g,n,I-1/2,J}(\omega)\right] + \frac{\eta_n}{\Delta y_J}\left[\delta\psi_{g,n,I,J+1/2}(\omega) - \delta\psi_{g,n,I,J-1/2}(\omega)\right] \\
&\qquad + \left[\Sigma_{t,g,0,I,J} + \frac{i\omega}{v_{g,I,J}}\right]\delta\psi_{g,n,I,J}(\omega) = \sum_{g'}\sum_{l=0}^{L}(2l+1)\Sigma_{sl,g'\to g,0,I,J}\sum_{m=-l}^{l} R_l^m(\boldsymbol{\Omega_n})\,\delta\phi^m_{l,g',I,J}(\omega) \\
&\qquad\qquad + \frac{1}{k_{eff}}\chi^{dyn}_{g,I,J}\sum_{g'}\nu\Sigma_{f,g',0,I,J}\,\delta\phi_{g',I,J}(\omega) + S_{g,n,I,J}(\omega) + \gamma S^{Fict}_{g,n,I,J}(\omega)
\end{aligned}
\tag{5.1}
$$

The fictitious source is denoted as $S^{Fict}_{g,n,I,J}$ and is multiplied by a factor γ which can take values between 0 and 1. The choice of the factor γ allows to tune the strength of the fictitious source and improve the convergence properties of the iterative scheme by choosing values for γ that are less then unity. If $\gamma = 0$, the original discrete ordinate equation is solved. If $\gamma = 1$, the mitigation of ray effects is expected to be maximum, but the convergence rate is the worst.

The construction of the fictitious source is based on the “Miller-Reed Source” proposed in [47]. The introduction of such a term into the discrete ordinates equations allows to obtain a set of spherical-harmonics-like equations. The complete fictitious source contains four terms. However, it is found through numerical tests that this source causes convergence problems of the unaccelerated or CMFD-accelerated schemes. Hence, in NOISE-SN, the fictitious source contains only the following two terms:

$$
\begin{aligned}
&S^{Fict}_{g,n,I,J}(\omega) = \\
&\sum_{m=1}^{N/2}\left[\left(\sum_{l'=0}^{N-1}\sum_{m'}^{l'} Y_{l'}^{m'}(\boldsymbol{\Omega_n})\sum_{n'}^{N(N+2)/2} a^{m'}_{n',l'}\mu_{n'}Y_N^{2m-1}(\boldsymbol{\Omega_{n'}})\right)\left(\frac{\partial}{\partial x}\delta\varphi^{2m-1}_{g,N}(\omega)\right)_{I,J}\right] \\
&\qquad + \sum_{m=1}^{N/2}\left[\left(\sum_{l'=0}^{N-1}\sum_{m'}^{l'} Y_{l'}^{m'}(\boldsymbol{\Omega_n})\sum_{n'}^{N(N+2)/2} a^{m'}_{n',l'}\eta_{n'}Y_N^{2m-1}(\boldsymbol{\Omega_{n'}})\right)\left(\frac{\partial}{\partial y}\delta\varphi^{2m-1}_{g,N}(\omega)\right)_{I,J}\right]
\end{aligned}
\tag{5.2}
$$

This source is algebraically equivalent to the source developed by Lathrop [46], but its formulation and implementation follow the procedure proposed by Miller and Reed [47].

The parameter N is the order of S_N chosen for each numerical calculation. The terms Y_l^m are the spherical harmonics, and they are related to the real spherical harmonics R_l^m through:

$$Y_l^m = \sqrt{\frac{(2l+1)}{2\pi}} R_l^m \tag{5.3}$$

The spatial derivatives in Eq. (5.2) are computed with a central finite difference scheme in each computational cell:

$$\left(\frac{\partial}{\partial x}\delta\varphi_{g,N}^{2m-1}(\omega)\right)_{I,J} = \frac{\delta\varphi_{g,N,I+1/2,J}^{2m-1}(\omega) - \delta\varphi_{g,N,I-1/2,J}^{2m-1}(\omega)}{\Delta x_I} \tag{5.4}$$

$$\left(\frac{\partial}{\partial y}\delta\varphi_{g,N}^{2m-1}(\omega)\right)_{I,J} = \frac{\delta\varphi_{g,N,I,J+1/2}^{2m-1}(\omega) - \delta\varphi_{g,N,I,J-1/2}^{2m-1}(\omega)}{\Delta y_J} \tag{5.5}$$

The moments at the surfaces are computed according to a quadrature formula, i.e.:

$$\delta\varphi_{g,N,I\pm1/2,J}^{2m-1}(\omega) = \sum_{\mathrm{n}'}^{\mathrm{N(N+2)/2}} a_{n',N}^{2m-1}\delta\psi_{g,n',I\pm1/2,J}(\omega) \tag{5.6}$$

The coefficients $a_{n,l}^m$ in both Eqs. (5.2) and (5.6) are related to the quadrature selected for the calculation. According to Eq. (5.2), the coefficients should be evaluated for all directions specified in the quadrature set. In one of the directions, a total number of N_0 moments for each coefficient need to be calculated. For instance, the moments of the n-th direction are arranged in a column vector:

$$\bar{a}_n = \left[a_{n,0}^0, a_{n,1}^0, a_{n,1}^1, \dots, a_{n,l}^m, \dots, a_{n,N}^{N-1}\right]^T \tag{5.7}$$

Then they are determined by solving the following linear system of equations:

$$\bar{\bar{Y}}\bar{a}_n = \bar{b}_n \tag{5.8}$$

The $N_0 \times N_0$ matrix $\bar{\bar{Y}}$ is given as:

$$\bar{\bar{Y}}= \begin{bmatrix} Y_0^0(\mu_1,\eta_1) & Y_1^0(\mu_1,\eta_1) & \cdots & Y_N^{N-2}(\mu_1,\eta_1) & Y_N^{N-1}(\mu_1,\eta_1) \\ Y_0^0(\mu_2,\eta_2) & Y_1^0(\mu_2,\eta_2) & \cdots & Y_N^{N-2}(\mu_2,\eta_2) & Y_N^{N-1}(\mu_2,\eta_2) \\ \vdots & \ddots & \ddots & \ddots & \vdots \\ Y_0^0(\mu_n,\eta_n) & Y_1^0(\mu_n,\eta_n) & \cdots & Y_N^{N-2}(\mu_n,\eta_n) & Y_N^{N-1}(\mu_n,\eta_n) \\ \vdots & \ddots & \ddots & \ddots & \vdots \\ Y_0^0(\mu_{N_0},\eta_{N_0}) & Y_1^0(\mu_{N_0},\eta_{N_0}) & \cdots & Y_N^{N-2}(\mu_{N_0},\eta_{N_0}) & Y_N^{N-1}(\mu_{N_0},\eta_{N_0}) \end{bmatrix} \tag{5.9}$$

and the column vector $\bar{b}_n$ is given as:

$$\bar{b}_n = \begin{cases} 1, & for\ the\ n-th\ element \\ 0, & elsewhere \end{cases} \tag{5.10}$$

Since the fictitious source given in Eq. (5.2) is computed from the angular neutron noise, it is updated in each group similar to the self-scattering term.

The current selection of the fictitious source is compatible with the CMFD method presented in Chapter 4. The CMDF equation does not need to be modified as the fictitious source term vanishes after angle integration. The only modification required is an additional update for the term using the CMFD solutions before the start of a new full iteration:

$$S_{g,n,I,J}^{Fict,ITE+1}(\omega) = S_{g,n,I,J}^{Fict,ITE}(\omega)\frac{\delta\Phi_{g,IC,JC}^{CMFD,ITE}}{\delta\Phi_{g,IC,JC}^{ITE+\frac{1}{2}}} \qquad for\ (I,J) \in (IC,JC) \tag{5.11}$$

The two-dimensional neutron noise calculation scheme with fictitious source correction can thus be incorporated into the CMFD accelerated scheme with minor modifications, as summarized in Algorithm 4.

Algorithm 4: CMFD scheme with fictitious source correction for the dynamic module

```
Begin with initial CMFD guess by solving Eq. (3.34) with $\hat{D} = 0$
    while $\Re^{err}$ or $\Im^{err} > \varepsilon$
        for outer iteration count $\leq N_O$ do
            for $g$=1 to $g = G$ do
                for inner iteration count $\leq N_I$ do
                    Sweep through the angular directions and spatial domain
                    Update moments and self-scattering term
                    Compute and update fictitious source term
                end for
            end for
            Update fission source term
        end for
        Solve Eq. (4.34) for $\delta\Phi_{g',IC,JC,KC}^{CMFD}$
        Adjust noise moments, incoming angular flux, and fictitious source according to
        Eqs. (4.47), (4.48) and (5.11)
        Update both the scattering and fission source term
    end while
```

5.3 Neutron noise problem in the C4V system

A first test is carried out using the neutron noise problem in the C4V system that is described in Section 4.3. The impact of the order of discrete ordinates on the NOISE-SN neutron noise calculations is investigated. In addition, the correct implementation and the performance of the fictitious source are also verified.

The calculations are performed over a 170×170 grid of square meshes equal in size (i.e., $\Delta x = \Delta y = 0.252\ cm$). Thus, each fuel or guide tube cell of the C4V system is divided into 5×5 identical, homogeneous squares. For acceleration, the original CMFD method is used, and the CMFD equations are discretized over a coarser grid whose computational cells correspond to the size of the fuel and guide tube cells. Each full iteration includes one inner iteration and one outer iteration.

In Fig. 5.1, the neutron noise amplitude and phase are plotted along the right boundary of the system (see Fig. 4.3). The mesh index in the figure is counted from the top to the bottom. The figure is based on calculations with S8 and S32 P_N-T_N quadrature sets without fictitious source, and calculations using S8 P_N-T_N quadrature set with the fictitious source of strength 0.9 and 1.

The neutron noise results in this problem do not suffer from any severe ray effect. Nevertheless, minimal numerical oscillations can be observed in the amplitude and phase of the S8 calculation without any fictitious source. By increasing the order of S_N, the oscillations can be eliminated while almost identical amplitude and phase results can be obtained.

The application of the fictitious source also reduces the small oscillations. While the smoothening effect is similar for both strength of the fictitious source, a minor shift in both the amplitude and phase can be observed. The shift becomes larger as the strength increases since the solution takes more the characteristic of a spherical-harmonic solution. These results thus confirm the correct implementation of the fictitious source.

The calculations shown in Fig. 5.1 are also examined in terms of the efficiency of the iterative schemes. For a convergence criterion of 1×10^{-6}, the number of full iterations required for convergence and the related wall clock time are reported in Table 5.1. The computational work is performed with a 1×10-core Intel Xeon E5-2630v3 processor.

If the strength of the fictitious source is equal to 1.0, the number of iterations is very high, and the computational time is longer than what needed for the S32 calculation. By reducing the strength, such an increase in the number of iterations can be substantially limited.

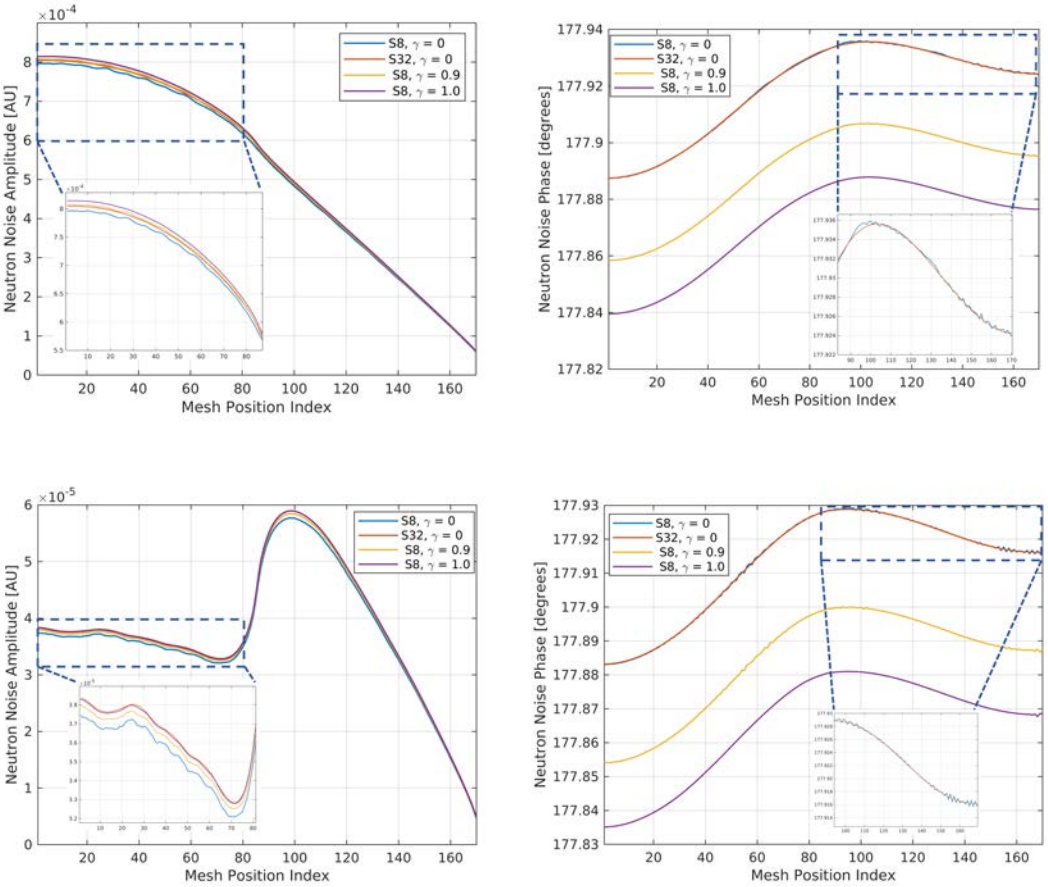

Figure 5.1 Simulation of C4V neutron noise problem; fast noise amplitude (top-left) and phase (top-right), thermal noise amplitude (bottom-left) and phase (bottom-right)

Table 5.1 Number of iterations and wall clock time required for convergence in the C4V neutron noise problem

SN	8			32
γ	0	0.9	1.0	0
Number of iterations	19	55	585	19
Wall clock time [mins]	~7.1	~23	~231	~78

5.4 Neutron noise problem in the C5G7 system

Ray effects are further studied on a neutron noise problem defined in a more complex configuration, i.e., the C5G7 benchmark system [48]. In this case the ray effects are found to be severe, therefore the application of a mitigation strategy is essential.

5.4.1 Problem specifications

The C5G7 configuration is a 2-dimensional system that includes four fuel assemblies arranged in a 2×2 grid and a water reflector/moderator region on the east and south peripheries (see Fig. 5.2). Two UO_2 fuel assemblies are in the north-west and south-east positions of the 2×2 grid, and two MOX fuel assemblies are in the north-east and south-west positions. Each fuel assembly consists of 17×17 square cells that are equal in size and have a side length of 1.26 cm. These physical cells include a central circular region with a radius of 0.54 cm and a surrounding region. The circular region is either a fuel-clad element, a guide tube, or a fission chamber, while the surrounding region is moderator. A set of seven-energy group cross sections is assigned to each kind of composition. The cross sections, the neutron kinetic parameters and the data for eight families of delayed neutron precursors are specified in [49].

The neutron noise source is defined as a perturbation in one of the MOX fuel pins, whose location is shown in Fig. 5.2. The perturbation is a fluctuation of the neutron capture cross section over all the energy groups. Its amplitude is 5% of the static value of the cross section and the frequency is equal to 1 Hz.

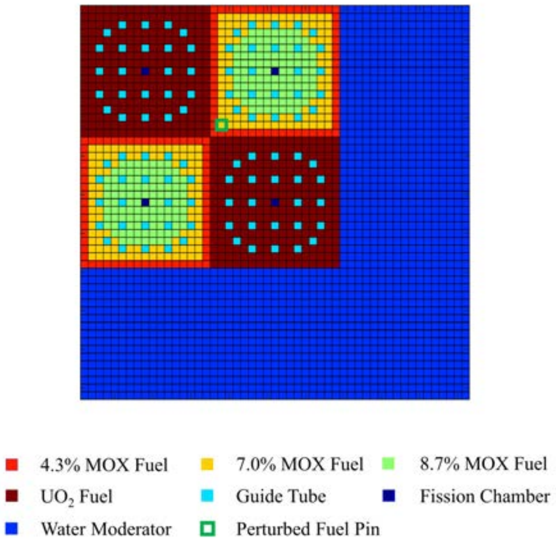

Figure 5.2 C5G7 system configuration with the location of the noise source

5.4.2 Modelling

The transport calculations are accelerated by the CMFD method. Accordingly, a fine grid is used for the transport sweeps and a coarse grid for the CMFD calculation.

In the fine grid for the transport sweeps, a fuel, guide tube, or fission chamber cell is divided into 4×4 computational cells, see Fig. 5.3. The central four computational cells are identical in size, and they approximate the circular fuel pin, guide tube, or fission chamber, preserving the actual area. The same spatial discretization is used for the reflector water region. Therefore, the fine grid for the entire system consists of 204×204 computational cells.

For the CMFD calculation, the coarse grid is given by 51×51 computational cells. The size of the computational cells is equal to the size of the fuel, guide tube and fission chamber cells.

For the static calculations, one inner iteration and one outer iteration are performed before the adCMFD acceleration. For the neutron noise calculations, each full iteration consists of the original CMFD method with two inner iterations and one outer iteration. The convergence criterion is set to 1×10^{-6} for both modules.

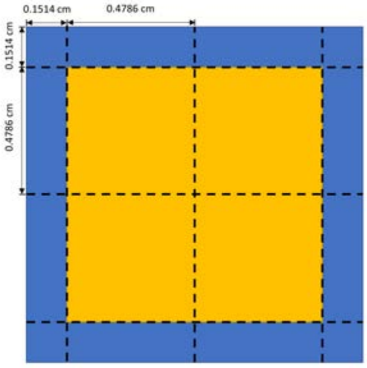

Figure 5.3 Discretization of the fuel, guide tube, or fission chamber; fine mesh for the transport sweeps

5.4.3 Order of discrete ordinates

The neutron noise problem defined in the C5G7 system is first simulated with different orders N of discrete ordinates, i.e., equal to 16, 32 and 64, to analyze the possible impact on the results.

Static calculation

The static solutions are first determined. The results for k_{eff} are given in Table 5.2. Although the circular fuel pins are represented by a relatively coarse mesh, the values of k_{eff} are in good agreement with the reference value [48]. The largest discrepancy with respect to the reference is found for the S64 case to be 105 pcm. In Table 5.2, the number of iterations required for convergence and the wall clock time are also reported. The same number of iterations is required for all calculations while the computational time increases with the higher S_N approximations.

Table 5.2 Effective multiplication factor, number of iterations and wall clock time in the C5G7 static calculations

	Reference	S16	S32	S64
k_{eff}	1.18655	1.18617	1.18723	1.18760
Number of iterations	--	38	38	38
Wall clock time [hours]	--	~2.5	~6.2	~12.6

In Fig. 5.4, the static fluxes computed with S16, S32 and S64 approximations are plotted along the diagonal that crosses the MOX fuel assemblies and that includes the perturbed fuel cell. The x-axis labels of the plot are such that the mesh index counts, along the diagonal, the computational cells starting from the bottom-left corner. The values are taken for the first and the seventh energy group, which are representatives of the fast and thermal energy groups, respectively. In the first group, the solutions agree well, and the largest differences are observed in the computational cells associated with the water surrounding the fuel pins. In the seventh group, the calculations yield consistent static fluxes.

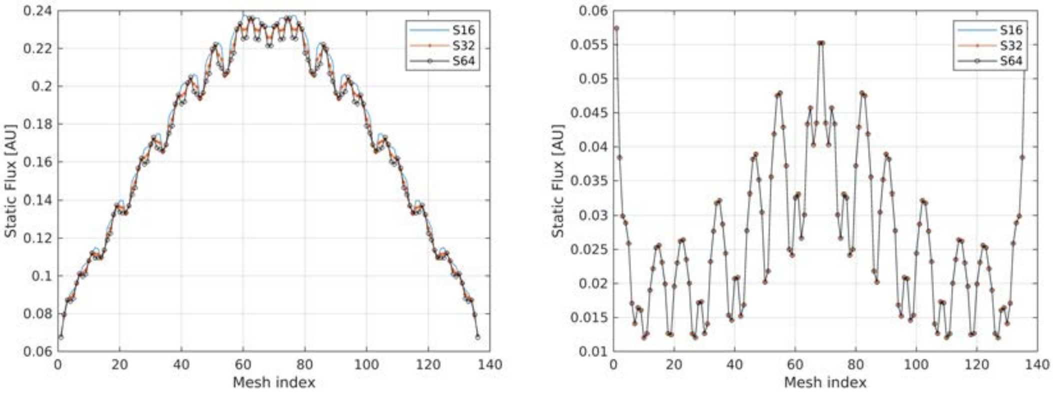

Figure 5.4 Static flux with different orders of discrete ordinates along the diagonal that crosses the MOX fuel assemblies in the C5G7 system; first energy group (left) and seventh energy group (right)

Neutron noise calculation

Figure 5.5 shows the neutron noise amplitude along the diagonal of the MOX fuel assemblies. The results are again taken from the first and seventh groups. The neutron noise amplitude resembles the static flux because the system is small and tends to respond to small perturbations in a point-kinetic manner. Yet, a local effect is found at the location of the neutron noise source. The variation of the amplitude with respect to the S_N order is similar to what is observed for the static fluxes, with the largest differences found for the amplitudes of the first group in the computational cells associated with the water surrounding the fuel pins. The phase along the diagonal is not affected by the S_N order, see Fig. 5.6.

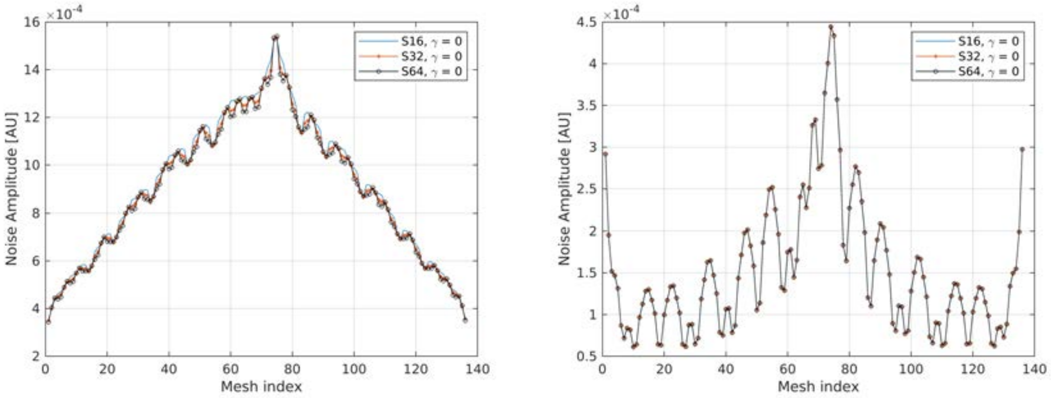

Figure 5.5 Neutron noise amplitude with different orders of discrete ordinates along the diagonal that crosses the MOX fuel assemblies in the C5G7 system; first energy group (left) and seventh energy group (right)

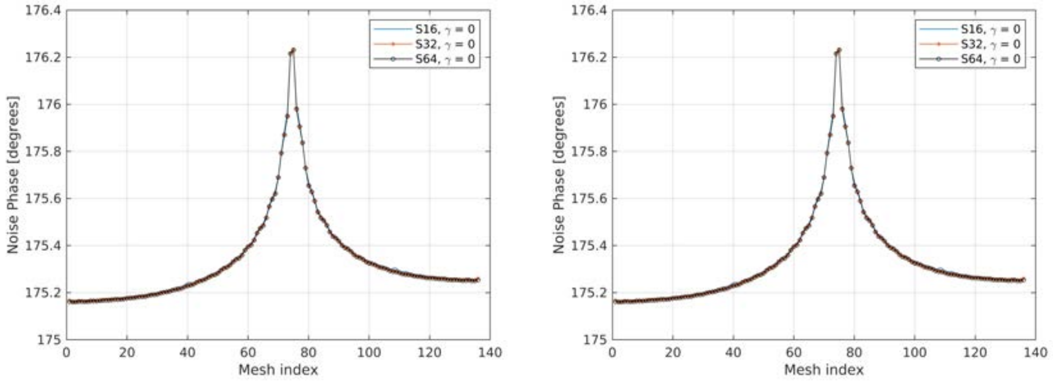

Figure 5.6 Noise phase calculated with different orders of discrete ordinates along the diagonal that crosses the MOX fuel assemblies in the C5G7 system; first energy group (left) and seventh energy group (right)

Although the spatial distributions of the neutron noise calculated with different orders of discrete ordinates are consistent in most of the points of the system, numerical issues are identified in the reflector region. In some cells located in the bottom-right corner, the S16 approximation predicts the noise phase for the first energy group to be equal to 0 degrees, which is unphysical, see top-right plot in Fig. 5.7. The noise phase is expected to be ∼180° because a variation of the number of neutron captures induces an opposite variation in the neutron flux. In the other energy groups, some numerical distortions of the phase are also found, although they are much smaller than those in the first group (for instance, barely visible in Fig. 5.7, the phase in the seventh group has a relatively large deviation in the bottom-right corner cell).

The selection of a higher order of discrete ordinates such as $N = 64$ improves the results, as shown in Fig. 5.8. In this case, a similar spatial distribution of the amplitude and qualitatively correct phase values in the first group can be obtained. Nevertheless, small distortions can still be identified in the bottom-right corner of the system. The improvement indicates that the unphysical values predicted by S16 calculations are due to ray effects. The localized noise source and the small scattering in the first energy group contribute to these ray effects. To obtain more accurate results, higher orders of S_N or a fictitious method should be considered.

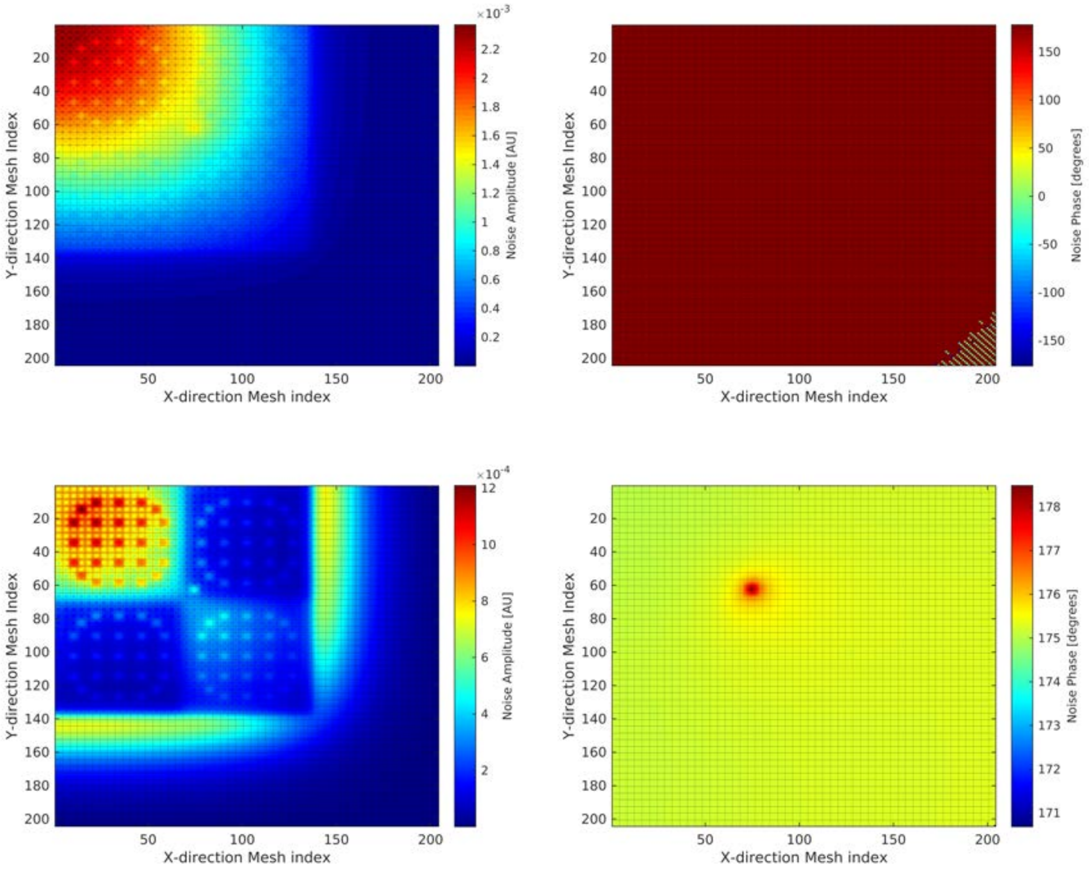

Figure 5.7 Neutron noise calculated with the S16 approximation in the C5G7 system: first-energy group amplitude (top-left) and phase (top-right) and seventh-energy group amplitude (bottom-left) and phase (bottom-right)

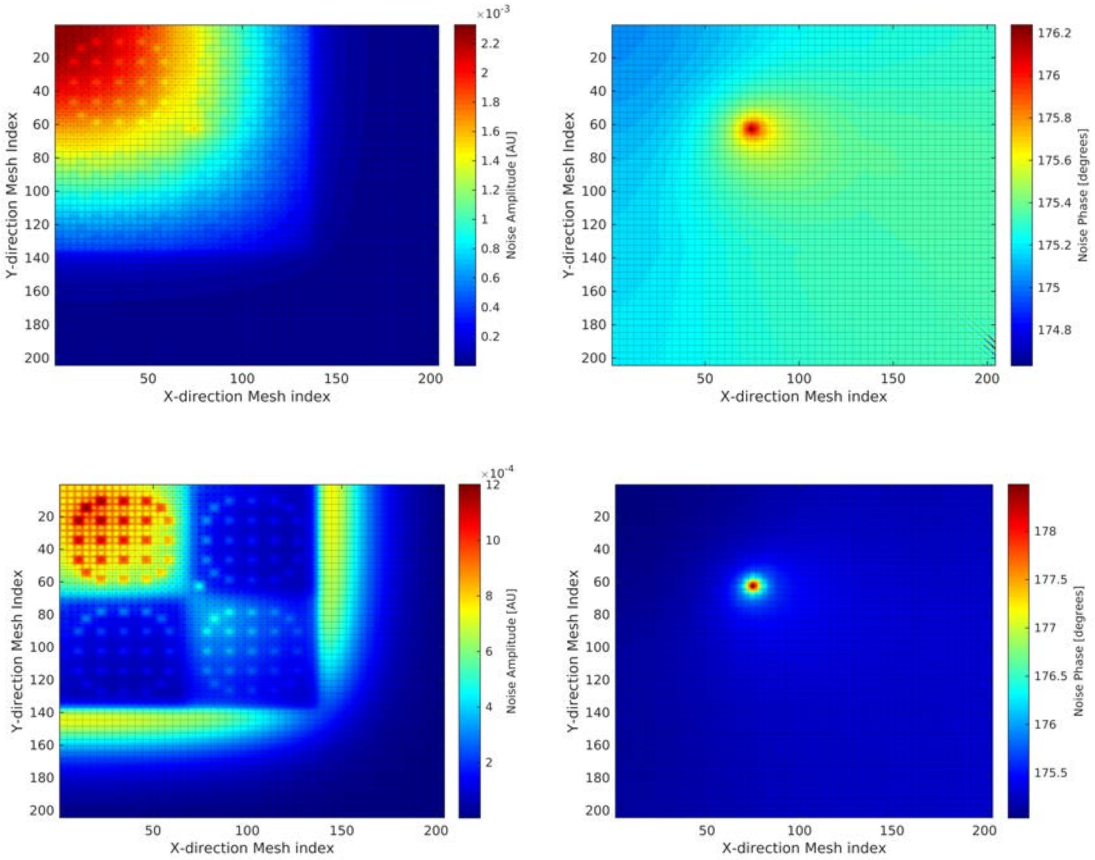

Figure 5.8 Neutron noise calculated with the S64 approximation in the C5G7 system; first energy group amplitude (top-left) and phase (top-right) and seventh energy group amplitude (bottom-left) and phase (bottom-right)

5.4.4 Fictitious source method

The neutron noise problem is solved combining the fictitious source method and the S16 approximation. The strength of the fictitious source is selected to be 0.8 and 0.9.

The analysis is focused on the neutron noise calculated in a column of computational cells along the lower part of the right boundary of the system, in the reflector region, where the S16 approximation predicts unphysical values of the noise phase. In Fig. 5.9, the real and imaginary parts of the neutron noise obtained from the fictitious source method, the normal S16, and the normal S64 are compared. The indices used in the x-axes of Fig. 5.9 correspond to the Y-direction mesh indices used in Fig. 5.8, the X-direction mesh being equal to 204.

The normal S16 calculation shows that the unphysical phase values are due to the large oscillations of the real and imaginary parts. By increasing the S_N order or by using the fictitious source method, the oscillations are significantly reduced. The mitigation effects achieved in the fictitious source calculations are more significant than the S64 calculation. The larger the strength of the fictitious source is, the more substantial improvement is gained.

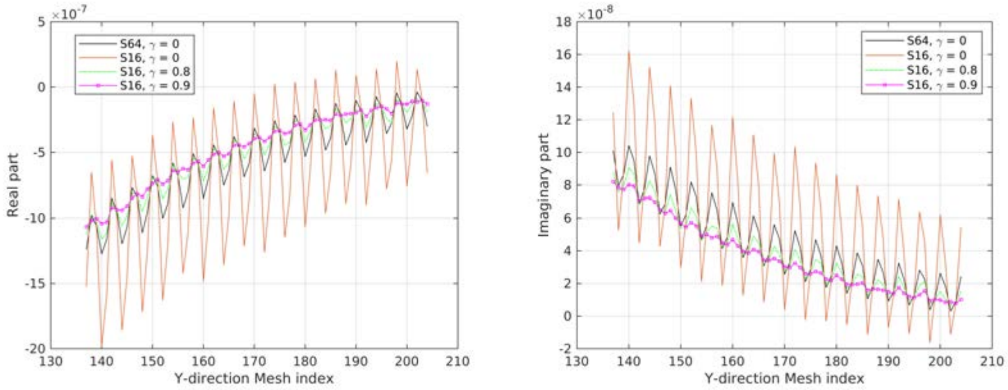

Figure 5.9 Effect of the different strength γ of the fictitious source on the S16 calculations; real (left) and imaginary (right) part of the neutron noise for the first energy group plotted along the right boundary of the system

In Fig. 5.10, the spatial distributions of the neutron noise for the first and seventh energy group, over the entire system, are shown for the $\gamma = 0.9$ calculation. Compared to Fig. 5.8, very similar results are obtained, and the phase takes physical, correct values.

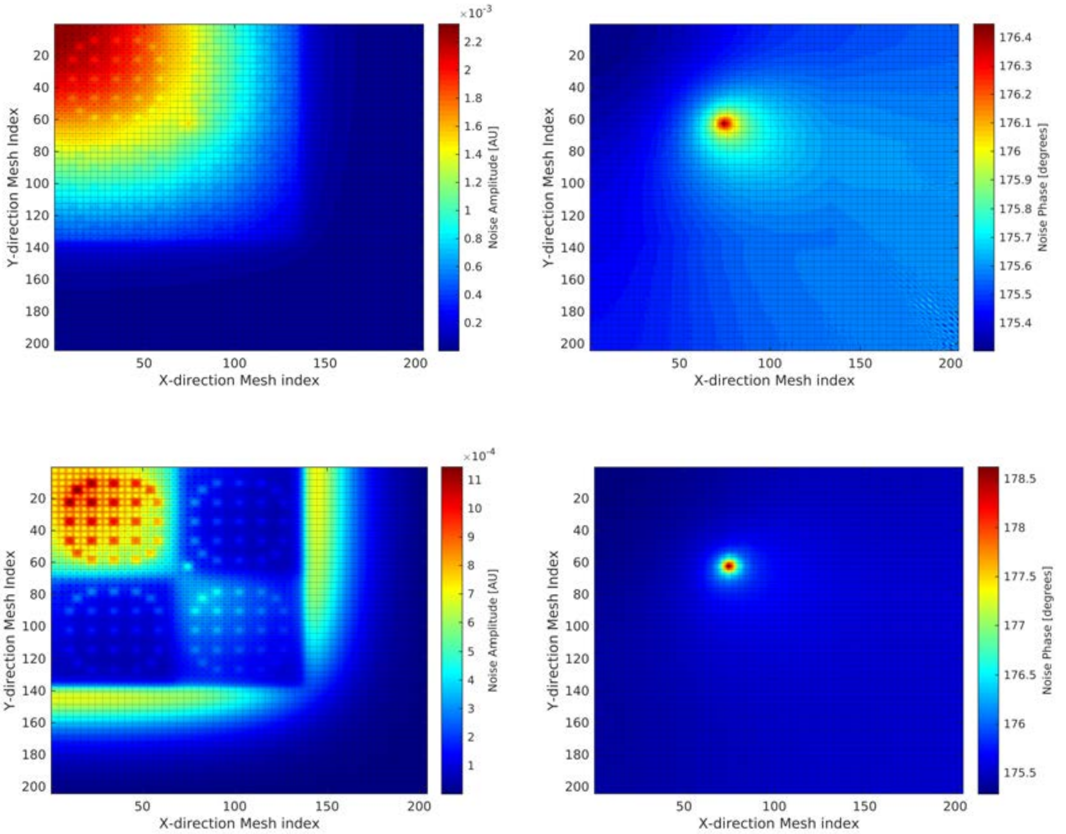

Figure 5.10 Neutron noise calculated using the S16 approximation and a fictitious source of strength $\gamma = 0.9$; first-energy group amplitude (top-left) and phase (top-right) and seventh-energy group amplitude (bottom-left) and phase (bottom-right)

5.4.5 Convergence of the scheme with fictitious source

Concerning the use of the fictitious source, tests are carried out to optimize the numerical performance of the solver for the simulation of the C5G7 neutron noise problem.

The fictitious source of strength $\gamma = 1.0$ causes extremely slow convergence rate, and it is estimated to require more than 1000 iterations. According to the experience in the C4V case, the choices such as $\gamma = 0.8$ or $\gamma = 0.9$ improve the convergence and are thus selected.

A certain number of ordinary full iterative loops before introducing the fictitious source into the solution scheme is necessary to avoid numerical instabilities. In the current case, the initial seven iterative loops are run without the fictitious source.

Given a convergence criterion with ε equal to 1×10^{-6}, the number of iterations and the wall clock time (using 2×10-core Intel Xeon E5-2630v3 processors) required for the convergence of the neutron noise calculations in the C5G7 system are summarized in Table 5.3.

Table 5.3 Number of iterations and wall clock time required for the C5G7 neutron noise calculations

SN	16			32	64
γ	0	0.8	0.9	0	0
Number of iterations	33	55	100	33	32
Wall clock time [hours]	~4.8	~8.7	~15.8	~12.4	~26.6

The increase of the fictitious source strength leads to slightly higher numbers of iterations, but these iterations take less computational time than the S64 calculation while attaining better mitigation effects. Therefore, the fictitious source method is shown to mitigate ray effect with a limited increase of the overall computational effort.

The maximum pointwise relative differences between the real and imaginary parts of the scalar neutron noise computed in two consecutive iterations are plotted in Fig. 5.11. The convergence of these calculations becomes smooth after some iterations.

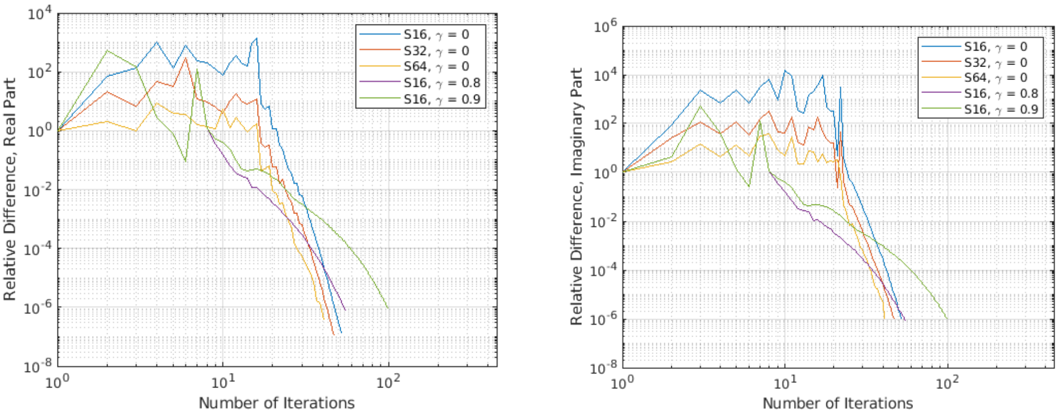

Figure 5.11 Convergence of the real (left) and imaginary (right) part of the scalar neutron noise for the C5G7 neutron noise calculations

Chapter 6

Simulation of numerical problems and experiments

In order to verify NOISE-SN, numerical problems and neutron noise experiments are simulated. In Section 6.1, NOISE-SN is compared with other neutron noise solvers using two neutron noise exercises defined in a simplified nuclear fuel assembly. In Section 6.2, NOISE-SN is used to simulate two neutron noise experiments. In Section 6.3, an example of the use of NOISE-SN to identify possible limitations of a low-order neutron noise method based on diffusion theory is reported. Part of this discussion is based on Paper II and V.

6.1 Comparison between NOISE-SN and other neutron noise solvers

Several neutron noise solvers based on stochastic or deterministic methods were developed in the CORTEX project [3, 50, 51]. Two numerical neutron noise exercises are defined in a 2-D simplified UOX fuel assembly and used to compare some of the solvers. The results are published in Paper II. Accordingly, NOISE-SN (developed in the framework of this thesis and in Paper II referred to as the Chalmers SN solver) is compared with:

- A stochastic solver in the Monte Carlo code TRIPOLI-4, developed by CEA [13, 52]
- A Monte Carlo solver, developed by KU – Kyoto University [14]
- The deterministic Integro-Differential Transport - IDT lattice solver embedded in APOLLO3, developed by CEA [12]
- The diffusion-based solver CORE SIM+, developed by Chalmers University of Technology [10]
- The diffusion-based solver FEMFFUSION, developed by UPV - Universitat Politècnica de València [53]

FEMFFUSION computes the solutions in the time domain while the others solve the neutron noise equation in the frequency domain.

6.1.1 Description of the benchmark problems

The simplified fuel assembly together with the reference computational spatial grid is shown in Fig. 6.1. The assembly contains 264 homogeneous square fuel pins, each with a size of

$0.7314\ cm \times 0.7314\ cm$, and 25 homogeneous water holes of the size $1.26\ cm \times 1.26\ cm$. The assembly is surrounded by a thin water blade with a thickness of $0.08\ cm$, and thus the size of the entire system is $21.58\ cm \times 21.58\ cm$. Reflective boundary conditions are applied to all four sides of the system. All the calculations are based on pre-generated two energy group nuclear cross sections and neutron velocities, and one family of precursor. The values for the nuclear data are available in Paper II.

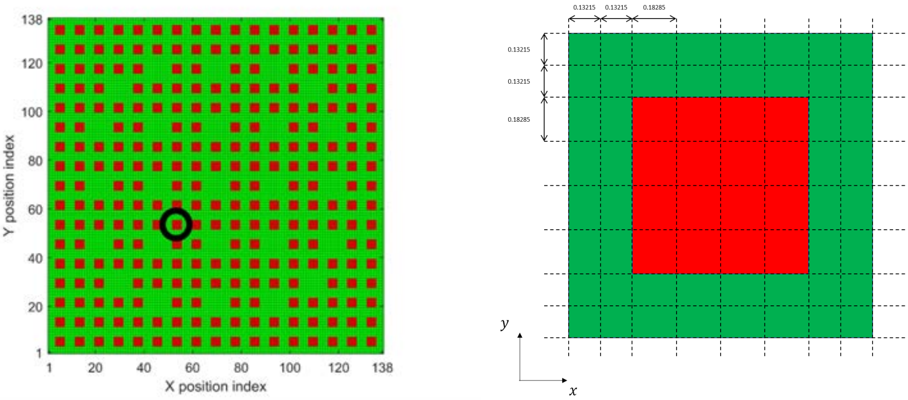

Figure 6.1 Simplified UOX fuel assembly (left) and the reference computational mesh for each fuel cell or water hole (right); fuel pins are in red, water region is in green, and the perturbed fuel pin is highlighted with a black circle

The two neutron noise exercises are defined as the perturbation of the properties of one fuel pin in the assembly, with the position being the same and shown in Fig. 6.1.

In exercise 1, a simple isotropic noise source is considered. The noise source is artificially given as $-1 + i$ in the thermal group, and the frequency is set to 3 Hz.

In exercise 2, the noise source is defined as fluctuations in all the macroscopic cross sections of the fuel pin as:

$$\Sigma_{t,g}(r,t) = \Sigma_{t,g,0}(r) + 0.041\Sigma_{t,g,0}(r)\cos(\omega_0 t) \tag{6.1}$$

$$\Sigma_{s,g\to g'}(r,t) = \Sigma_{s,g\to g',0}(r) + 0.034\Sigma_{s,g\to g',0}(r)\cos(\omega_0 t) \tag{6.2}$$

$$\Sigma_{f,g}(r,t) = \Sigma_{f,g,0}(r) + 0.021\Sigma_{f,g,0}(r)\cos(\omega_0 t) \tag{6.3}$$

The amplitudes of the fluctuations are arbitrarily chosen, and the frequency is fixed to 1 Hz, i.e., $\omega_0 = 2\pi$.

6.1.2 Static results

The static calculations of NOISE-SN make use of S32 P_N-T_N quadrature set and are accelerated with the CMFD method, in which one inner-two outer transport iterations are performed. Furthermore, the adCMFD equations are solved over the fine transport mesh (as presented in Fig. 6.1) for an optimized convergence rate. Only 9 iterations are required for convergence of the static calculation.

The calculated values for the effective multiplication factor are summarized in Table 6.1. NOISE-SN computed a value of k_{eff} that is close to the TRIPOLI-4 result taken as reference (the difference is 84 pcm).

Table 6.1 Comparison of the multiplication factor

Solvers	k_{eff}	Difference [pcm]
TRIPOLI-4®	0.99912 ± 8 pcm	Reference
KU Monte Carlo solver	0.99919 ± 7 pcm	7
APOLLO-3®	0.99784	-128
NOISE-SN	0.99996	84
CORE SIM+	1.01309	1397
FEMFFUSION	1.01367	1485

In Figs. 6.2 and 6.3, the static fluxes for both energy groups are plotted along the diagonal of the system, crossing the position of the perturbed fuel pin. Taking the TRIPOLI-4 results as the reference, the relative differences of the fluxes are also given in these figures. In the post-processing step, the static fluxes in both groups are normalized using the fast neutron flux computed in the first computational cell located at the left-bottom corner of the fuel assembly without the water blade. NOISE-SN predicts almost identical results as the other higher-order transport solvers. The maximum difference between the NOISE-SN solution and the reference is around 1%.

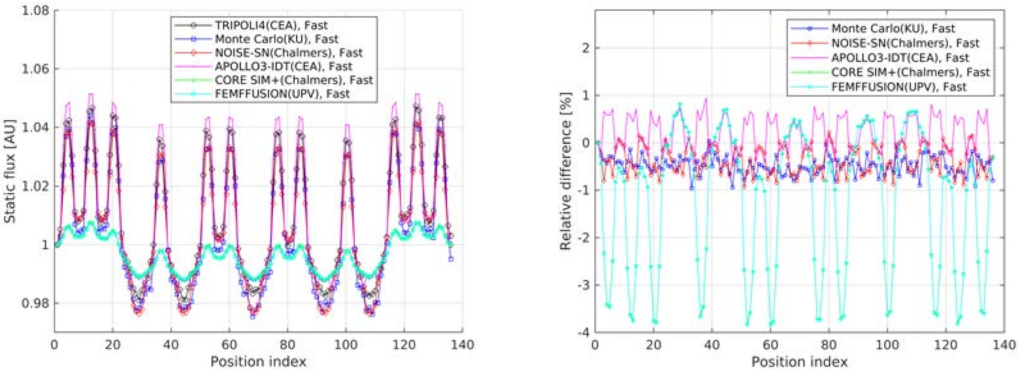

Figure 6.2 Fast static flux (left) and relative differences with respect to TRIPOLI-4 (right), along the diagonal of the fuel assembly crossing the perturbed fuel pin

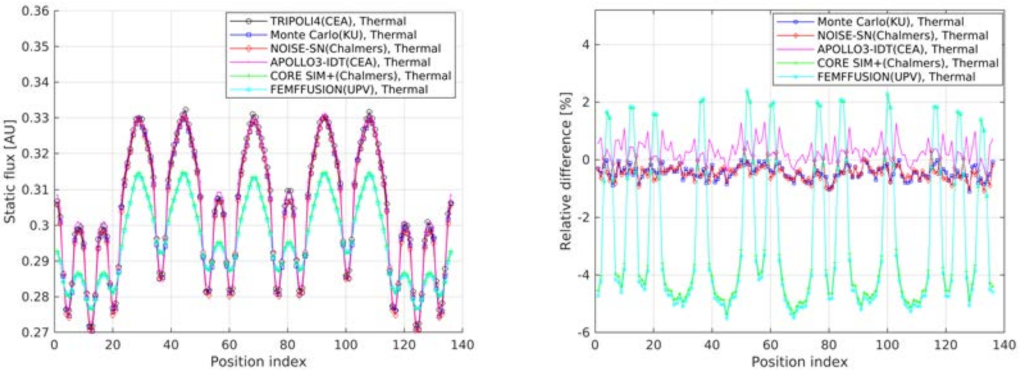

Figure 6.3 Thermal static flux (left) and relative differences with respect to TRIPOLI-4 (right), along the diagonal of the fuel assembly crossing the perturbed fuel pin

6.1.3 Neutron noise results

Consistently with the static calculations, the neutron noise calculations performed by NOISE-SN make use of S32 P_N-T_N quadrature set and are accelerated with the normal CMFD method with one inner - two outer transport iterations. The number of full iterations required for convergence is 9 and 10 for exercise 1 and 2, respectively. Although the reflective boundaries conditions are applied to all sides of the system, the CMFD accelerated scheme converged in a smooth manner, see the convergence of the real and imaginary parts for both exercises in Fig. 6.4.

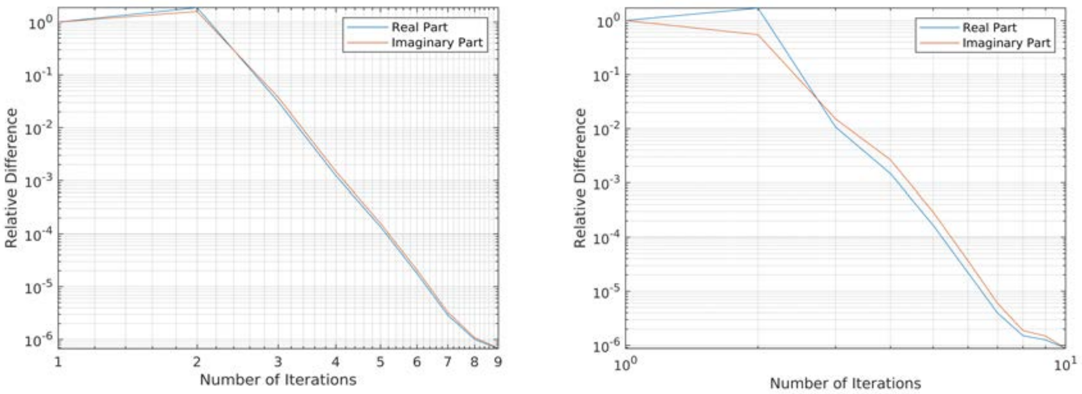

Figure 6.4 Convergence of the real and imaginary part in the neutron noise calculations; exercise 1 (left) and exercise 2 (right).

Similar to the static case, the neutron noise amplitudes in both groups are normalized to the amplitude in the fast group, computed in the cell located at the left-bottom corner. The water blade is again neglected in the comparison. In Paper II, the relative neutron noise (i.e., the normalized neutron noise amplitudes divided by the respective static fluxes) is shown so that the local effect of the noise source can be clearly seen.

Exercise 1

In Fig. 6.5, the results for exercise 1 are shown. The amplitude and phase are taken along the diagonal line that passes through the perturbed fuel pin. The amplitude follows the shape of the static flux while local peaks can be observed in the vicinity of the noise source location, i.e., around position index 50 (compared with Figs. 6.2 and 6.3).

NOISE-SN estimates amplitude and phase values that are in very good agreement with the other higher-order transport solvers. For the amplitude, the maximum difference between the NOISE-SN and the reference TRIPOLI4 solution is 0.7%, and it is found in the fast group. For the phase results, the maximum difference is less than 0.25% for both groups.

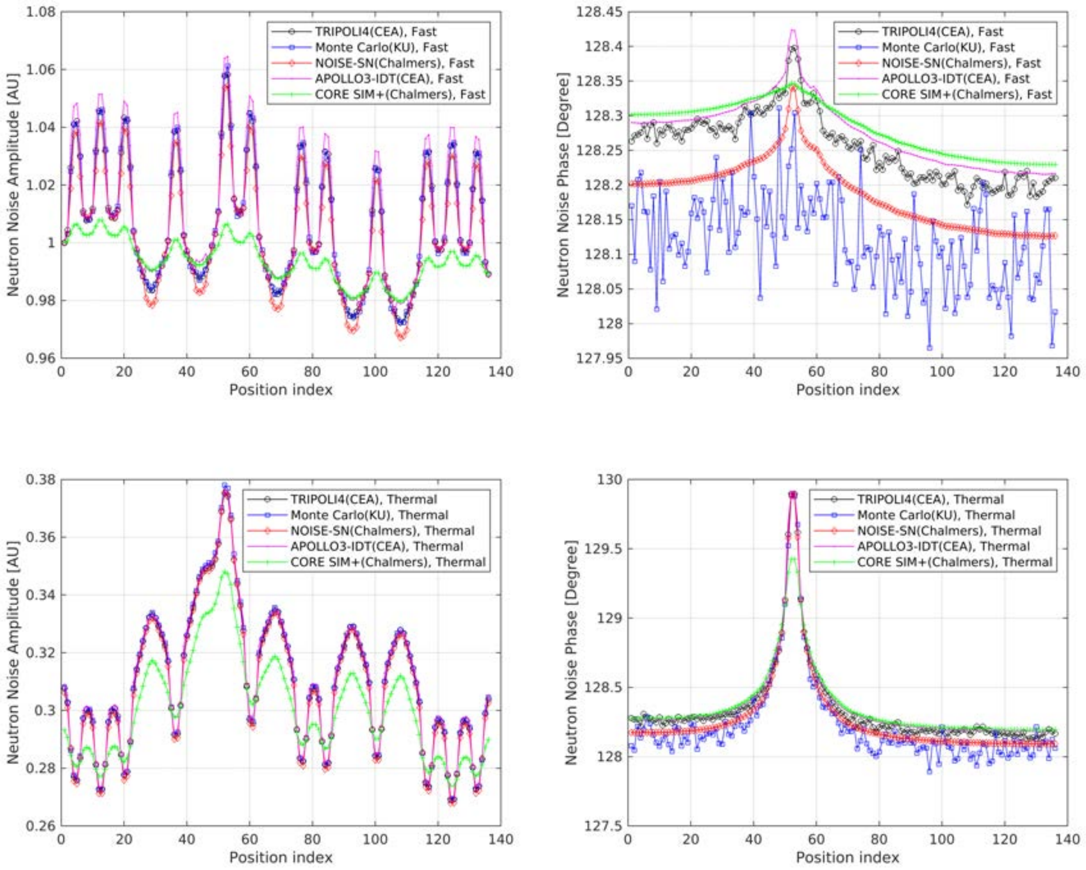

Figure 6.5 Neutron noise calculated for exercise 1: fast group amplitude (top-left) and phase (top-right), and thermal group amplitude (bottom-left) and phase (bottom-right)

Exercise 2

The solutions of exercise 2 along the diagonal crossing the perturbed fuel pin, are shown in Fig. 6.6. NOISE-SN and the other higher-order solvers predict close values of neutron noise. Similar to Exercise 1, the differences between NOISE-SN and the reference TRIPOLI-4 are less than 2% in amplitude and less than 0.2% in phase.

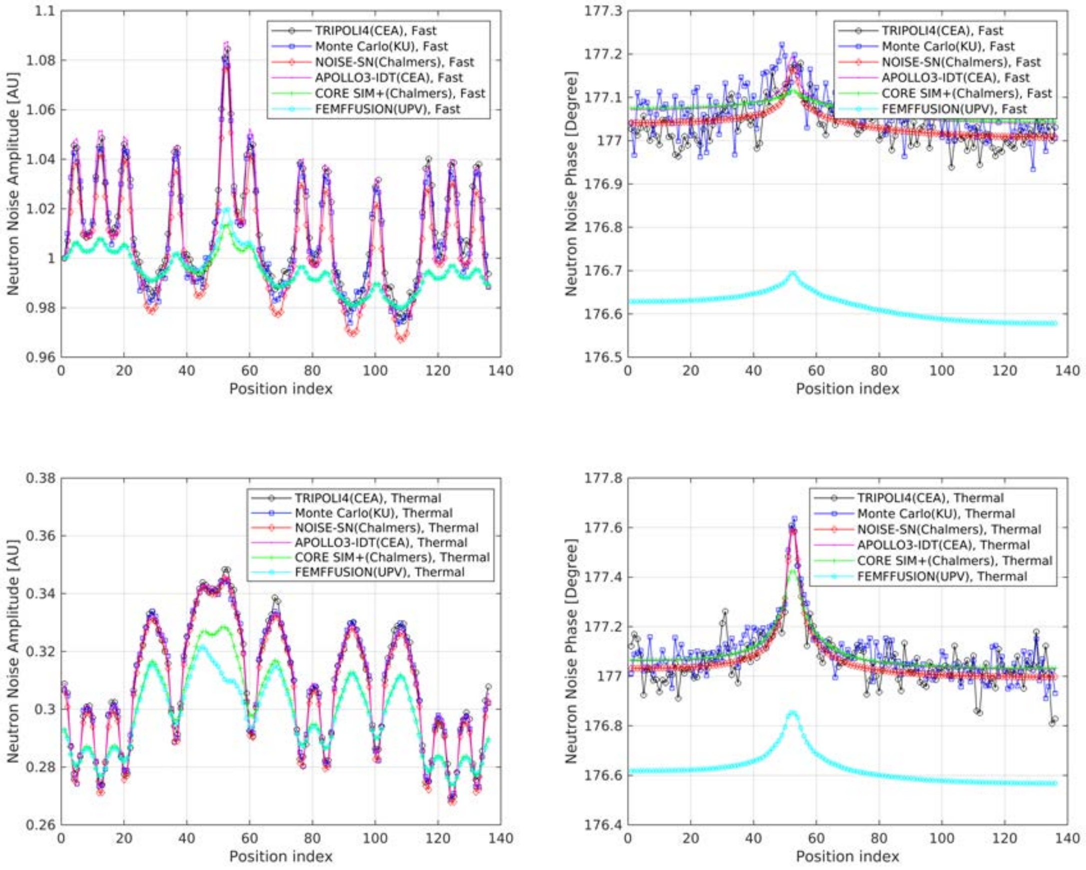

Figure 6.6 Neutron noise calculated for exercise 2: fast group amplitude (top-left) and phase (top-right), and thermal group amplitude (bottom-left) and phase (bottom-right)

6.2 Simulation of neutron noise experiments

In the CORTEX project, neutron noise experiments were performed in the CROCUS reactor at École Polytechnique Fédérale de Lausanne (EPFL). NOISE-SN is used to simulate two of these experiments and the results are compared with the experimental data.

6.2.1 COLIBRI neutron noise experiments in CROCUS

The CROCUS reactor is a pool type, light water moderated reactor [54]. The core shape is approximately cylindrical and has a diameter of about 59 cm and a height of 100 cm. The core is radially separated into two layers. The inner layer consists of 336 UO_2 fuel rods with a pitch of 1.837 cm, and the outer layer is loaded with 176 U metal fuel rods with a pitch of

2.917 cm. The reactor can be controlled by either the control rods or by adjusting the water level in the reactor.

Different campaigns of neutron noise experiments have been carried out in CROCUS. The solver NOISE-SN is used to simulate experiments 12 and 13 of the first COLIBRI campaign [55]. In these experiments, a cluster of 18 U metal fuel rods is oscillated via the COLIBRI device, with an amplitude of $+/-$ 2 mm and a frequency of 0.1 Hz in experiment 12 and 1 Hz in experiment 13. The top view of the CROCUS reactor and the positions of the vibrating rods are shown in Fig. 6.7. The reactor is equipped with neutron detectors to record the neutron flux variations with respect to time, see their locations in Fig. 6.7.

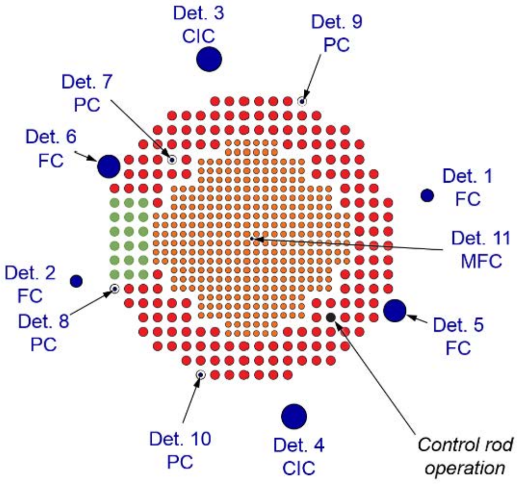

Figure 6.7 Top view of the reactor configuration and locations of the detectors, the vibrating fuel rods are shown in green (courtesy of EPFL) [53].

6.2.2 Modelling

A relatively coarse 3-D model of the CROCUS reactor is used for the simulations. The model consists of 4 homogeneous regions, i.e., the inner fuel region, the outer fuel region (where the cluster of vibrating fuel rods is located), the water reflector region, and the control rods. A set of two-energy group homogenized macroscopic cross sections is associated with each of the regions. The effective kinetic nuclear data are based on 8 families of delayed neutron precursors. The nuclear data are generated with the Monte Carlo code Serpent and provided by EPFL.

The system is discretized with 54 axial layers: the top 3 layers have a height of 1.76433 cm, and the other 51 layers have a height of 1.857 cm. The total height of the modelled system is thus 100 cm. The radial mesh is identical for each of the axial layer and is shown in Fig. 6.8. It consists of equally sized square cells with a side length of 1.4585 cm, except for the oscillating region, where a finer mesh is needed to model the perturbation. The overall computational spatial grid is $88 \times 108 \times 54$.

Given the model for these simulations, the cluster of vibrating fuel rods is described as one homogeneous region within the homogeneous outer fuel region. The vibrating region introduces a local perturbation in the macroscopic cross sections. Such a perturbation is modelled with the ϵ/d method [56]. According to this method, a fixed grid is used and Dirac-like perturbations are specified at the left and right boundaries of the vibrating region, which are perpendicular to the direction of the motion. For an accurate numerical approximation of the Dirac-like perturbations, the mesh must be very fine around the boundaries affected by the vibration, see Fig. 6.8.

If the left boundary is considered (see plot on the right in Fig. 6.8), the macroscopic cross sections associated with the cells adjacent on both sides are perturbed by a value equal to the differences between the macroscopic cross sections of the two regions separated by the boundary, i.e.:

$$\delta\Sigma_{\alpha,g,left} = \Sigma_{\alpha,g,Water\ Region} - \Sigma_{\alpha,g,Outer\ Fuel\ Region} \tag{6.4}$$

The same procedure is followed to perturb the macroscopic cross sections of the cells surrounding the right boundary, i.e.:

$$\delta\Sigma_{\alpha,g,right} = \Sigma_{\alpha,g,Outer\ Fuel\ Region} - \Sigma_{\alpha,g,Inner\ Fuel\ Region} \tag{6.5}$$

In the equations above, α denotes a generic macroscopic cross section since the vibration affects all types of cross sections.

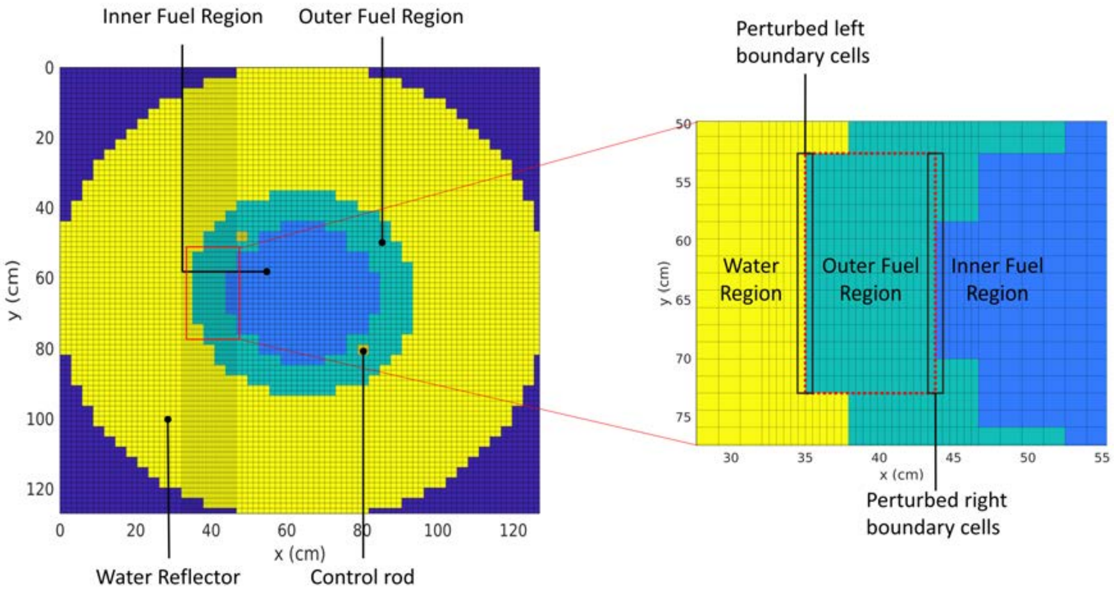

Figure 6.8 Radial mesh for the CROCUS reactor (left) and the locations of the perturbed computational cells (right)

The NOISE-SN simulations are performed using the S16 approximation and the P_N-T_N quadrature set. The static calculation is accelerated by adCMFD with one inner-two outer transport iterations. The frequency domain neutron noise calculations are performed with the normal CMFD acceleration with one inner-six outer iterations. Both static and neutron noise CMFD equations are discretized over the fine transport mesh.

6.2.3 Static calculations

For the static calculations, 25 full iterations are required for a convergence criterion of 10^{-6}. The effective multiplication factor computed with NOISE-SN is equal to 1.00208 and its difference with respect to the reference value [55] is +42 pcm. Figure 6.9 shows the radial distribution of the fast and thermal static fluxes at mid-elevation of the system and Fig. 6.10 shows the fluxes along the horizontal line that crosses the mid-elevation plane in the middle.

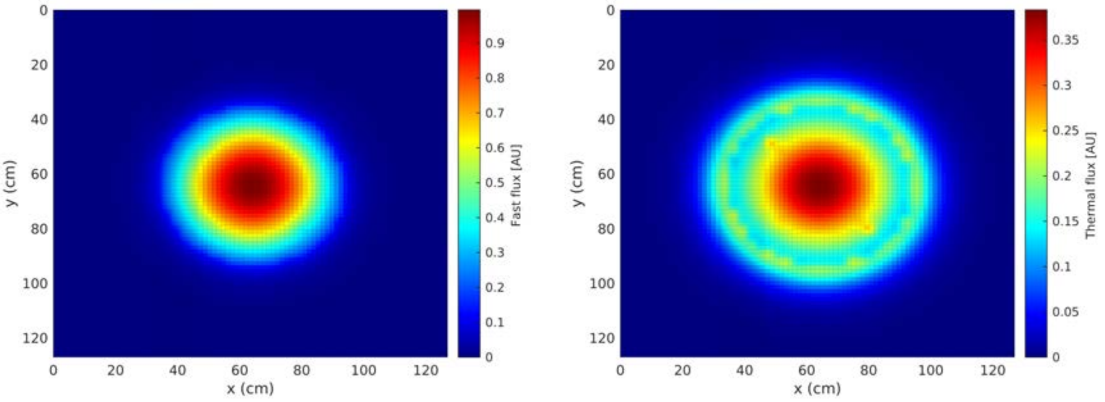

Figure 6.9 Fast (left) and thermal (right) static fluxes at mid-elevation.

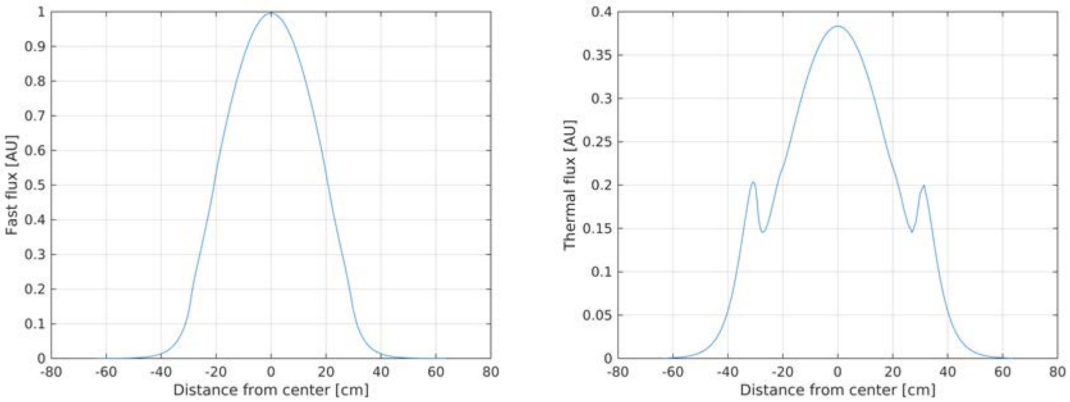

Figure 6.10 Fast (left) and thermal (right) static fluxes along the horizontal line that crosses the mid-elevation plane in the middle.

6.2.4 Neutron noise simulations

The neutron noise is calculated for experiments 12 and 13. In experiment 12 the amplitude of the vibration is $+/-$ 2 mm, and the frequency is 0.1 Hz. In experiment 13 the amplitude is $+/-$ 2 mm, and the frequency is 1.0 Hz.

The simulations require 31 and 29 iterations to reach convergence for experiments 12 and 13, respectively. Both simulations are run on 2×10-core Intel Xeon E5-2630v4 processors, and they take approximately 60 hours in terms of wall clock time.

For experiment 12, the noise calculated at mid-elevation is shown in Fig. 6.11. Due to the relatively small size of the reactor, the spatial distribution of the noise amplitudes follows the distribution of the static fluxes (compare Fig. 6.9 and plots on the left in Fig. 6.11). The phase of the thermal noise shows an out-of-phase behavior at the boundaries of the vibrating region, which is expected because of the oscillation of the fuel pins.

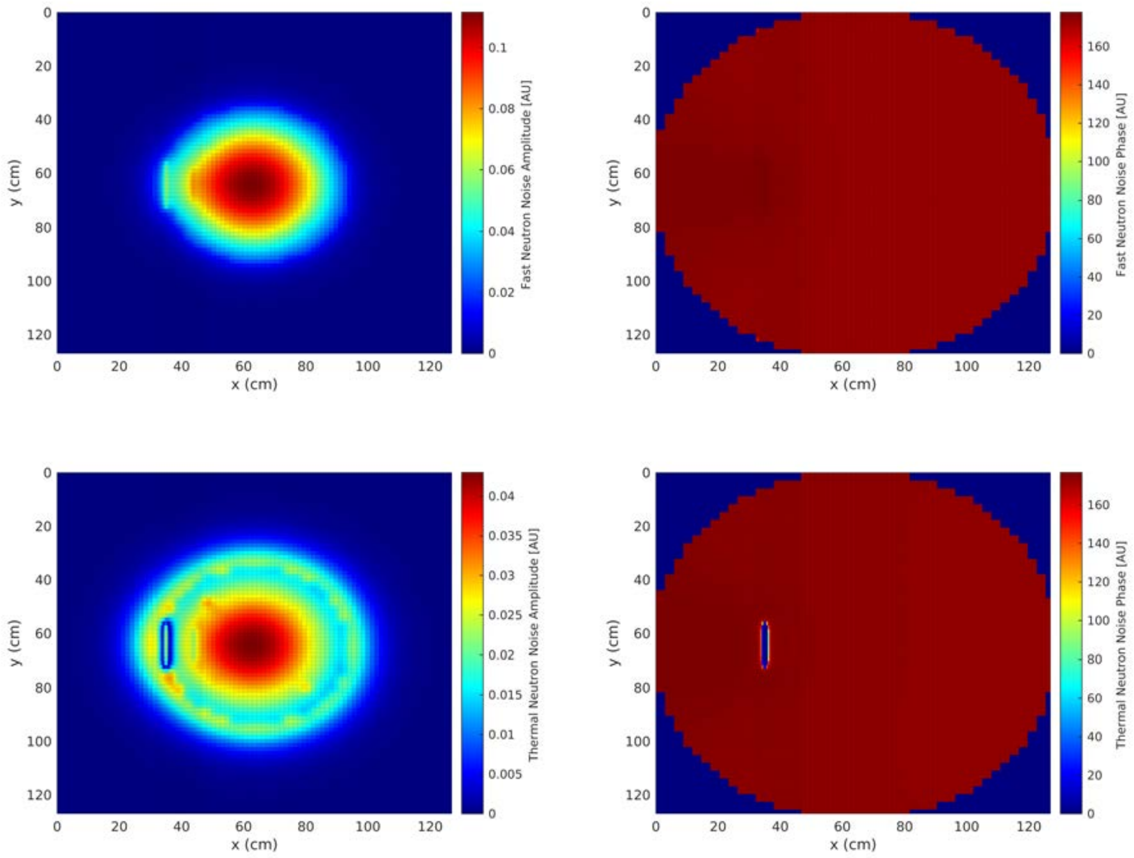

Figure 6.11 Experiment 12, neutron noise calculated at mid-elevation; fast amplitude (top-left) and phase (top-right) and thermal amplitude (bottom-left) and phase (bottom-right)

A similar spatial distribution and level of the noise is obtained in experiment 13. This is shown in Fig. 6.12, where the noise calculated in the two experiments is compared along the horizontal line that crosses the mid-elevation plane in the middle. This result is expected because the values of the frequency belong to the range corresponding to the plateau region of the zero-power transfer function of the reactor (see Section 2.4) and the static fluxes are the same for both experiments.

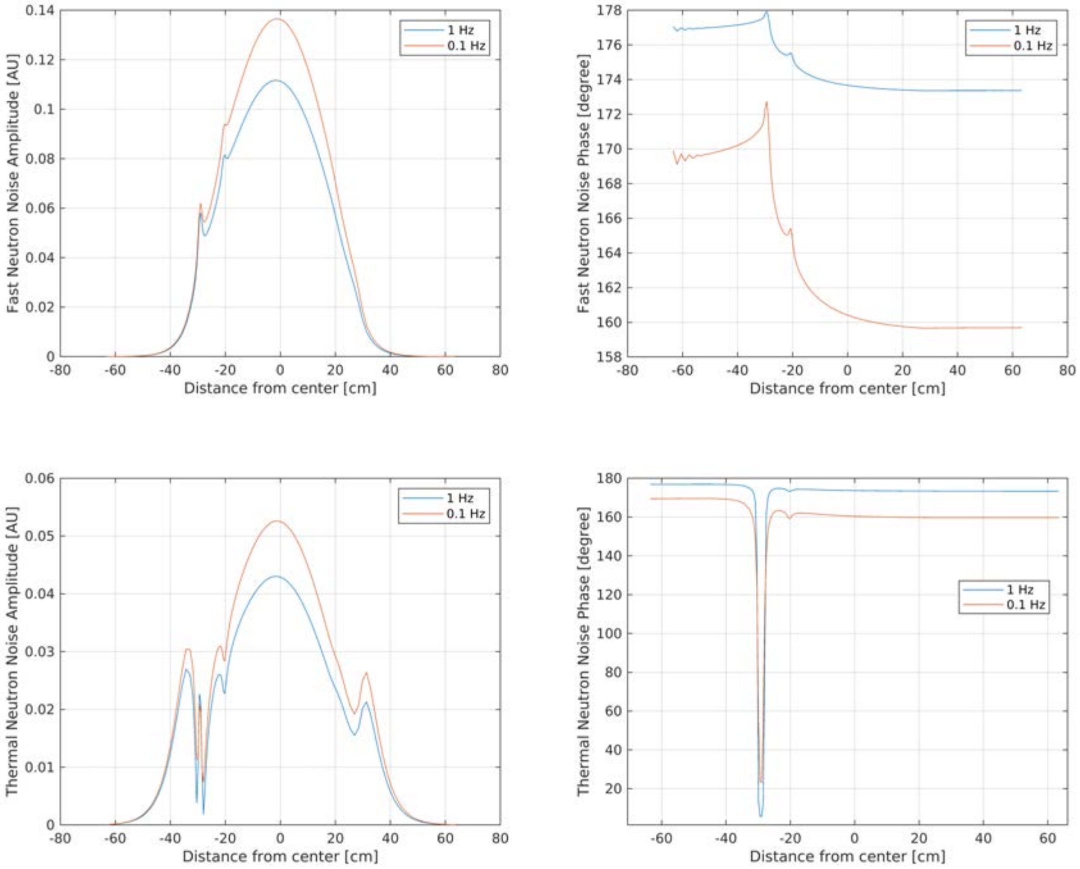

Figure 6.12 Comparison between experiments 12 and 13; fast (top) and thermal (bottom) noise along the horizontal line that crosses the mid-elevation plane in the middle.

6.2.5 Comparison with experimental results

The NOISE-SN results are compared to the experimental neutron noise, which is derived from the detector measurements in terms of Power Spectrum Density (PSD). If this quantity relates the signals of two different detectors, it is called Cross-Power Spectrum Density (CPSD). If only one single detector is considered, it is called Auto-Power Spectrum Density (APSD).

Detectors are not modelled in the NOISE-SN simulations. However, since the CROCUS detectors are mainly sensitive to thermal neutrons, PSD values are estimated from the thermal neutron noise and the thermal static flux calculated at the locations of the detectors, i.e.:

$$PSD_{i,j} = \left(\frac{\delta\phi_{th}}{\phi_{0,th}}\right)_i \left(\frac{\delta\phi_{th}}{\phi_{0,th}}\right)_j^* \tag{6.6}$$

The indices i and j refer to the detectors i and j (or their locations), respectively.

In the current study, the quantities of interest are the APSD amplitude for the generic detector i divided by the amplitude of the CPSD with respect to detector 5, and on the phase of the CPSD with respect to detector 5. The results for experiments 12 and 13 are shown in Figs. 6.13 and 6.14, respectively. In the x-axis, the detectors are ordered from the closest to the perturbation to the farthest. The uncertainties associated with the experimental data are also included.

The noise predicted with NOISE-SN is similar to the experimental neutron noise. The amplitude increases close to the vibrating region (detector 8 and 6) and decreases as the detector locations are further away. The phase with respect to detector 5 is small and the trend is relatively flat for both the calculations and the measurements. The simulations are in better agreement with the experimental data for Experiment 13, except for detectors 8 and 3. The location of detector 8 is very close to the perturbation and this may affect the accuracy of both the simulations and the measurements. The behavior of detector 3 may have been biased [53].

The results calculated with NOISE-SN have also been shown to be consistent with the results obtained from other neutron noise solvers. More details can be found in [53].

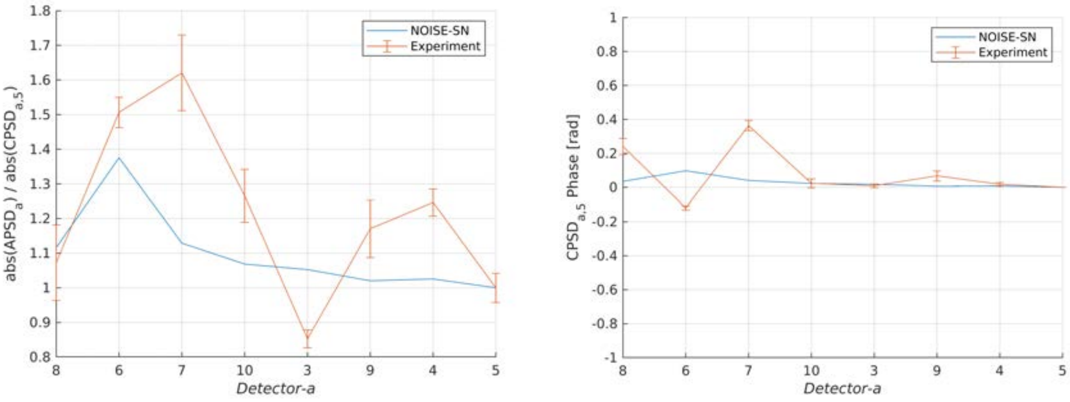

Figure 6.13 Experiment 12; relative noise amplitude (left) and noise phase (right)

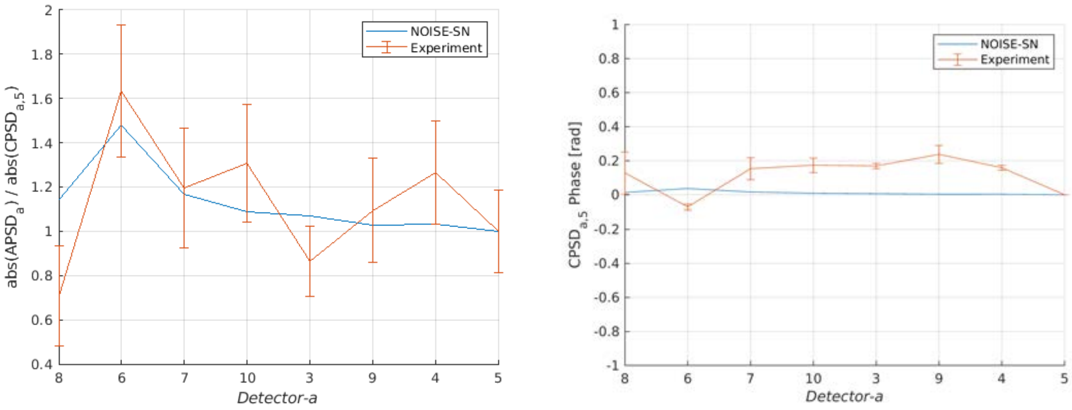

Figure 6.14 Experiment 13; relative noise amplitude (left) and noise phase (right)

6.3 Comparison with the diffusion-based solver CORE SIM+

The solver NOISE-SN and the diffusion-based solver CORE SIM+ [10] are compared over several numerical neutron noise problems (see Paper I, Paper II and Paper V). As an example, the neutron noise problem based on the C3 configuration and described in Section 4.3 is taken. The neutron noise source is defined as a perturbation of the macroscopic capture cross section in one fuel cell, with an amplitude of 5% and a frequency of 1 Hz.

The comparison can provide insights into possible limitations of the lower-order diffusion approximation. The results for the two neutron energy groups are similar, so only the thermal group in which the discrepancies are larger is discussed. The complete analysis can be found in Paper V.

For the NOISE-SN calculations, the S8 Level symmetric quadrature set is selected. As demonstrated in Chapter 5, the S8 approximation has very small ray effects and thus it can be considered accurate enough.

The calculations with both solvers are first performed using different computational spatial grids. The mesh is progressively refined; the coarser mesh consists of one node per each fuel cell/guide tube and the finer mesh has 8×8 equally sized square nodes per fuel cell/guide tube. The thermal neutron noise amplitude calculated in the central computational node of the perturbed fuel cell is plotted with respect to the different mesh sizes in Fig. 6.15. The results become mesh-independent for resolutions higher than 5×5 nodes per each fuel cell/guide tube. Then, the mesh with 5×5 square nodes per fuel cell/guide tube is used for the comparison between NOISE-SN and CORE SIM+.

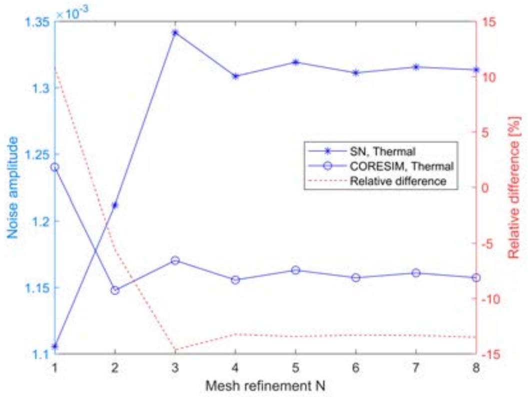

Figure 6.15 Effect of the spatial grid resolution on the amplitude of the thermal neutron noise at the location of the noise source

6.3.1 Static flux and neutron noise calculated with the 2 solvers

The two solvers are compared in terms of the thermal static flux and the thermal neutron noise amplitude, see Fig. 6.16. The general agreement is relatively good, although significant discrepancies are found.

Large differences are identified in the guide tube locations. The guide tubes introduce abrupt variations of the material properties of the system and these strong heterogeneities can be resolved better with higher-order transport methods than diffusion. In the case of the neutron noise, additional large differences are found at the location of the neutron noise source and its close surroundings. This is also an outcome of the benchmark exercises presented in Section 6.1, where the biggest deviations between higher-order and diffusion-based solvers arise near the neutron noise source, see, e.g., Fig. 6.6.

The relative differences for other locations in the system are very small, i.e., less than 3%. The phase predicted by both solvers are also very similar, with a maximum relative difference of 0.1%.

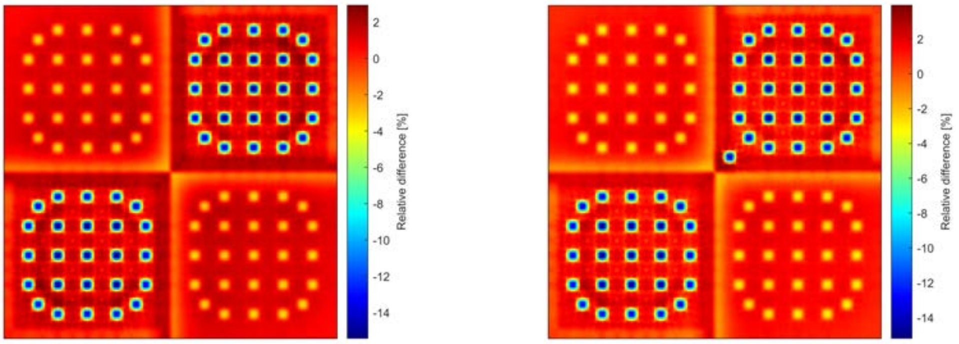

Figure 6.16 Spatial distribution of the relative differences between the two solvers, for the thermal neutron static flux (left) and for the thermal neutron noise amplitude (right)

6.3.2 Dependence on the frequency of the neutron noise source

To investigate further the relative differences between the two solvers, simulations are performed varying the frequency of the perturbation within the interval between 0.01 Hz and 100 Hz.

In Fig. 6.17, the thermal neutron noise amplitude and phase are shown for the central computational node of the perturbed fuel cell. For both solvers, the behavior of the neutron noise amplitude with respect to frequency is consistent with the zero-power reactor transfer function (see Section 2.4). The amplitude decreases as the frequency of the perturbation increases, except in a plateau region at intermediate frequencies where the amplitude is almost constant. The relative differences in the amplitude calculated at the location of the noise source increase significantly with higher frequencies, i.e., from ~8% at 0.01 Hz to ~24% at 100Hz. For frequencies in the plateau region, the relative differences do not vary significantly. In other system locations, similar trends are observed, but they are much weaker, indicating a relatively good agreement between NOISE-SN and CORE SIM+ (see details in Paper V).

The variation of the thermal noise phase with respect to frequency follows a bell shape, which is also consistent with the phase of the zero-power transfer function. In the plateau region, the relative differences are small (in absolute value, less than 1%). For higher or lower frequencies, the discrepancies increase slightly (about -3%). A similar behavior is observed for other locations in the system.

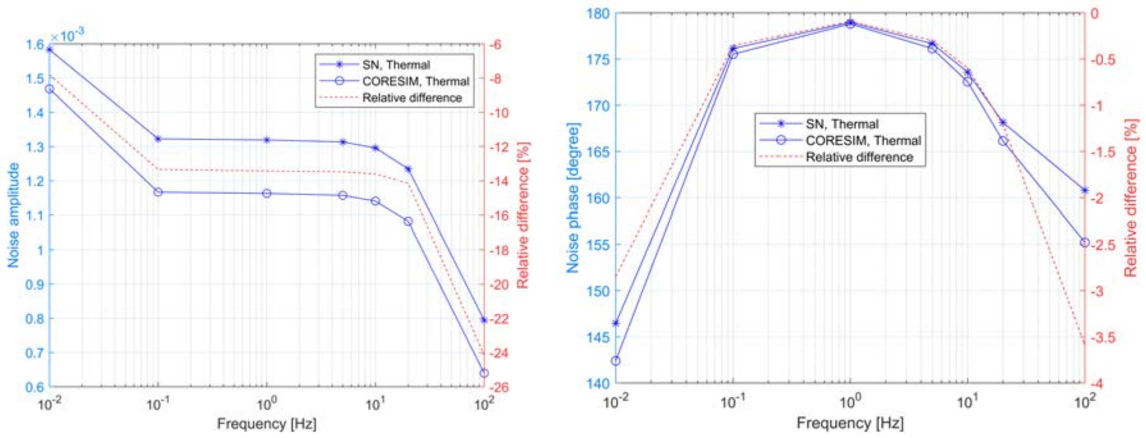

Figure 6.17 Thermal neutron noise amplitude (left) and phase (right) calculated with the two solvers and relative differences, at the location of the neutron noise source.

Chapter 7

Conclusions and recommendations for future work

The research presented in this doctoral thesis is summarized and conclusions are provided in Section 7.1. Possible recommendations for future work based on the results of the research are discussed in Section 7.2.

7.1 Summary and conclusions

In the work reported in this thesis, a higher-order method was investigated for the numerical solution of the frequency-domain neutron noise transport equation. For the purpose, the solver NOISE-SN was developed (see Paper I, and Chapters 3 to 5).

The solver NOISE-SN uses the discrete ordinates (S_N) method for the angular discretization of the equation, the diamond finite difference scheme for the spatial discretization, and the multi-energy group formalism for the energy discretization. The numerical algorithm is based on an inner-outer iterative scheme: the inner iterations provide estimates of the neutron flux/neutron noise with respect to the spatial and angular variables within each of the energy groups, while the outer iterations update the fission source and the overall scattering terms. The solver consists of a static and a dynamic module. The static module solves the static neutron transport equation and provides the steady-state, critical solution for the reactor system of interest. The dynamic module calculates the neutron noise in the frequency domain based on the static solution and the prescribed noise source which is given in terms of perturbations of macroscopic cross sections.

For the numerical acceleration of the algorithm (see Paper III, Paper IV, and Chapter 4), the Diffusion Synthetic Acceleration (DSA) method and different versions of the Coarse Mesh Finite Difference (CMFD) method were coded and tested using neutron noise problems defined in the two-dimensional, heterogeneous configurations C4V and C3, whose nuclear properties are described with two-energy group macroscopic cross sections. In the calculations of the neutron noise induced by an absorber of variable strength at the frequency of 1 Hz, the DSA method was shown to be stable and to reduce the number of iterations needed for convergence by a factor of 20 in comparison with the unaccelerated results. However, ~1200 iterations were required, which make the computational task still very time-consuming. The CMFD method has better performances and reduced the number of iterations to less than 100. Unstable convergence behavior of the CMFD method was observed in the case of C3 configuration. A careful selection of the degree of underrelaxation and number of transport inner-outer iterations was found to be important for the stabilization of convergence. The use of the linear prolongated CMFD method provided better convergence properties among the variants tested in this work. In addition, the CMFD method was demonstrated to be very effective for a wide range of frequencies, while the acceleration from the DSA method deteriorates as the frequency takes low values. Therefore, in the continuation of the work, mainly the CMFD method was used.

For the mitigation of ray effects that may arise from the angular discretization, the impact of the order of discrete ordinates and a fictitious source method were evaluated (see Paper I, and Chapter 5). For this purpose, a neutron noise problem was considered with an absorber of variable strength introduced in the two-dimensional, heterogeneous configuration C5G7 (whose macroscopic cross sections are given in 7 energy groups and the kinetic parameters are based on 8 families of delayed neutron precursors). The neutron noise calculations were found to be more prone to ray effects than the static calculations. For example, the S16 approximation that gives static results with minor numerical distortions, is not sufficient for the frequency-domain neutron noise calculations because of the effect of the neutron noise source and/or energy groups with low scattering. The ray effects cause numerical oscillations in the real and imaginary parts of the computed neutron noise, which in turn give unphysical fluctuations of the noise amplitude and incorrect values of the noise phase. By increasing the order of discrete ordinates, the ray effects may be reduced, but such calculations lead to a substantial increase in the computer memory requirements and in the computational time. As an alternative, a fictitious source method was implemented. As demonstrated with the calculations for the C5G7 neutron noise problem, the fictitious source method can provide a significant mitigation of the ray effects even when a relatively low order of discrete ordinates is applied. This approach has then the advantage of a lower computational cost. On the other hand, the addition of the fictitious source in the equations to be solved makes the convergence rate slower. To overcome this issue, tests were performed with different strengths of the fictitious source and with a number of initial ordinary transport iterations (CMFD-accelerated), and the results showed that convergence is improved.

To verify the correct implementation of the numerical models in NOISE-SN, numerical exercises and experiments were simulated (see Paper II, Section 6.1, and Section 6.2). The neutron noise calculated with NOISE-SN in the numerical exercises was compared to the results obtained from other higher-order transport solvers based on both deterministic and stochastic approaches, showing a good agreement. In addition, NOISE-SN was used to simulate COLIBRI neutron noise experiments where a cluster of fuel pins was oscillated in the research reactor CROCUS (EPFL, Switzerland). The calculations performed with the 3-D scheme of NOISE-SN and the estimations from the measurements capture similar characteristics of the neutron noise.

The solver NOISE-SN was also compared with the diffusion-based neutron noise solver CORE SIM+, to assess possible limitations of the diffusion approximation (see Paper I, Paper II, Paper V, and Section 6.3). Good agreement between the two solvers was found even though discrepancies may arise from the heterogeneities of the system and from the spatial and frequency effects of the perturbation (e.g., the differences may be more notable for perturbations at higher frequencies).

7.2 Recommendations for future work

Future work may be recommended as follows:

- The current NOISE-SN scheme relies on transport operators constructed solely with the static fluxes and the effective multiplication factor associated with the unperturbed configuration. However, perturbations in a reactor usually introduce reactivity variations, which are counterbalanced by, e.g., the control rods. Yet, the level of the neutron flux may change. Then the modelling of this effect requires to adjust the transport operator so that the regulating mechanisms can be reproduced and the resulting variations in the reference neutron flux can be taken in account [57].
- For the CMFD acceleration method, a convergence analysis can be performed to better understand the stable converging regime of the method and to tailor specific improvements for its stabilization in frequency-domain neutron noise calculations.
- The solution of the complex valued CMFD equations for problems with a large number of computational cells may be challenging. The application of efficient iterative methods (e.g., a GMRES method with preconditioning) for solving large linear systems associated with the CMFD equations would play a significant role in the overall performance of the neutron noise algorithm.
- The fictitious source method used in this thesis is limited to two-dimensional calculations and may lead to unacceptable slow convergence rates if complete elimination of ray effects is desired. Thus, the extension of the method to the three-dimensional case and alternative ray-effect mitigation methods that are less computationally expensive need to be studied.
- In this doctoral research, most numerical verification tests were performed using the scenario of an absorber of variable strength, since this neutron noise source is basic and can be used to build more realistic neutron noise sources. Then additional problems with more complex neutron noise sources need to be developed to further explore the numerical methods of NOISE-SN and to better understand neutron noise characteristics and their modelling.
- The calculations performed in this work rely on transport-corrected, isotropic scattering cross sections. An important aspect to be investigated is the effects of anisotropic scattering on neutron noise calculations. Therefore, suitable problems need to be defined and the modelling of anisotropic scattering in neutron noise calculations need to be evaluated.

References

[1] Nuclear Energy Agency, “The Role of Nuclear Energy in a Low-carbon Energy Future,” retrieved from https://www.oecd-nea.org/upload/docs/application/pdf/2019-12/nea6887-role-nuclear-low-carbon.pdf on October 16, 2021.

[2] I. Pázsit and C. Demazière, “Noise techniques in nuclear systems,” *Handbook of Nuclear Engineering*, pp. 1629-1737 (2010).

[3] C. Demazière, P. Vinai, M. Hursin, S. Kollias and J. Herb, “Overview of the CORTEX project”, *PHYSOR 2018 - Reactor physics paving the way towards more efficient systems,* Cancun, Mexico, April 22-26 (2018).

[4] I. Pázsit, N.S. Garis and O. Glöckler, “On the neutron noise diagnostics of pressurized water reactor control vibrations – IV: Application of neural networks,” *Nuclear Science and Engineering*, **124** (1), pp. 167-177 (1996)

[5] D.N. Fry, “Experience in reactor malfunction diagnosis using on-line noise analysis,” *Nuclear Technology*, **10** (3), pp. 273-282 (1971).

[6] D.N. Fry, R.C. Kryter and J.C. Robinson, “Analysis of neutron-density oscillations resulting from core barrel motion in a PWR nuclear power plant,” *Annals of Nuclear Energy*, **2** (2-5), 341-351 (1975).

[7] G. Kosály, L.J. Kostic, L. Miteff, G. Varadi and K. Behringer, “Investigation of the two-phase flow in a boiling water reactor using neutron-noise technique,” *Nuclear Engineering and Design*, **52** (3), pp. 357-370 (1979)

[8] I. Pázsit, “Dynamic transfer function calculations for core diagnostics,” *Annals of Nuclear Energy*, **19**(5), pp.303-312 (1992).

[9] C. Demaziere, “CORE SIM: A multi-purpose neutronic tool for research and education,” *Annals of Nuclear Energy*, **38**(12), pp.2698-2718 (2011).

[10] A. Mylonakis, P. Vinai and C. Demazière, “CORE SIM+: A flexible diffusion-based solver for neutron noise simulations”. *Annals of Nuclear Energy*, **155**, p.108149 (2021).

[11] M. Bahrami and V. Naser, “SN Transport Method for Neutronic Noise Calculation in Nuclear Reactor Systems: Comparative Study Between Transport Theory and Diffusion,” *Annals of Nuclear Energy*, **114**, pp. 236-244 (2018).

[12] A. Rouchon, M. Vadée Le Brun and A. Zoia, “Analysis and comparison of APOLLO3® and TRIPOLI-4® neutron noise solvers,” Proceedings of Physics of reactor 2020 (PHYSOR 2020), Cambridge, United Kingdom (2020).

[13] A. Rouchon, A. Zoia and R. Sanchez, “A New Monte Carlo Method for Neutron Noise Calculations in the Frequency Domain,” *Annals of Nuclear Energy*, **102**, pp. 465-475 (2017).

[14] T. Yamamoto, “Monte Carlo Method with Complex-valued Weights for Frequency Domain Analyses of Neutron Noise,” *Annals of Nuclear Energy*, **58**, pp. 72-79 (2013).

[15] C. Demazière, A. Tatidis and P. Vinai, “Monte Carlo-based dynamic calculations of stationary perturbations.” Accepted at *PHYSOR 2020 – Transition to a scalable future*, Cambridge, United Kingdom, March 29-April 2, 2020.

[16] G. I. Bell, and S. Glasstone, “Nuclear reactor theory (No. TID-25606),” US Atomic Energy Commission, Washington, DC, US, (1970).

[17] J.J. Hou, K.N. Ivanov, V.F Boyarinov and P.A. Fomichenko, “OECD/NEA benchmark for time-dependent neutron transport calculations without spatial homogenization,” *Nuclear Engineering and Design*, 317, pp.177-189 (2017).

[18] E. E. Lewis and W. F. Miller, “Computational methods of neutron transport.” (1984)

[19] K. Manalo, C.D. Ahrens and G. Sjoden, “Advanced quadratures for three-dimensional discrete ordinate transport simulations: A comparative study,” Annals of Nuclear Energy, 81, pp.196-206 (2015).

[20] G. Longoni, G “Advanced quadrature sets and acceleration and preconditioning techniques for the discrete ordinates method in parallel computing environments,” PhD thesis, University of Florida: Gainesville, FL (2004).

[21] A. Hébert, “Multigroup Neutron Transport and Diffusion Computations,” *Handbook of Nuclear Engineering*, pp. 753-909 (2010).

[22] M. Bando, T. Yamamoto, Y. Saito and T. Takeda, “Three-dimensional transport calculation method for eigenvalue problems using diffusion synthetic acceleration,” *Journal of Nuclear Science and Technology*, **22**(10), pp. 841-850 (1985).

[23] E.W. Larsen, “Unconditionally stable diffusion-synthetic acceleration methods for the slab geometry discrete ordinates equations. Part II: Numerical Results,” *Nuclear Science and Engineering*, **82**(1), pp. 64-70 (1982).

[24] Y. Y. Azmy and E. W. Larsen, “Fourier analysis of the diffusion synthetic acceleration method for weighted diamond-differencing schemes in cartesian geometries,” *Nuclear Science and Engineering*, **95**(2), pp. 106-115 (1987).

[25] M. Adams and E. Larsen, “Fast Iterative Methods for Discrete-Ordinates Particle Transport Calculations,” *Progress in Nuclear Energy*, **40**(1), pp. 3-159 (2002).

[26] A. Zhu, Y. Xu and T. Downar, “Fourier Convergence Analysis of the Infinite Homogenous Multigroup Time-Dependent Boltzmann Transport Equation Using Discrete Ordinates Formulation,” *Nuclear Science and Engineering*, **186**(1), pp. 23-36 (2017).

[27] H. Yi, “A neutron noise solver based on a discrete ordinates method,” Licentiate Thesis, Department of Physics, Chalmers University of Technology (2020).

[28] Z. Zhong, T. J. Downar, Y. Xu, M. D. DeHart and K. T. Clarno, “Implementation of two-level coarse-mesh finite difference acceleration in an arbitrary geometry, two-dimensional discrete ordinates transport method,” *Nuclear science and engineering,* **158**(3), pp.289-298 (2008).

[29] J. Y. Cho, K. S. Kim, H. J. Shim, J. S. Song, C. C. Lee and H. G. Joo, “Whole core transport calculation employing hexagonal modular ray tracing and CMFD formulation,” *Journal of nuclear science and technology,* **45**(8), pp.740-751 (2008).

[30] M. J. Lee, H. G. Joo, D. Lee and K. Smith, “Investigation of CMFD accelerated Monte Carlo eigenvalue calculation with simplified low dimensional multigroup formulation,” Proceedings of Physics of reactor 2010 (PHYSOR 2010), Pittsburgh, Pennsylvania, USA (2010).

[31] L. Jain, M. Prabhakaran, R. Karthikeyan and U. Kannan, “Convergence analysis of the non-linear CMFD schemes for acceleration of multi-group fixed source neutron transport calculations,” *Annals of Nuclear Energy,* **153**, p.108041 (2021).

[32] A. Zhu, Y. Xu, A. Graham, M. Young, T. Downar and L. Cao, “Transient methods for pin-resolved whole core transport using the 2D-1D methodology in MPACT,” Proceedings of Mathematics and Computation Applied to Nuclear Science and Engineering 2015 (M&C 2015), Nashville, Tennessee, USA, pp.19-23 (2015).

[33] K. P. Keady and E. W. Larsen, “Stabilization of Sn K-Eigenvalue Iterations Using CMFD Acceleration,” Proceedings of Mathematics and Computation Applied to Nuclear Science and Engineering 2015 (M&C 2015), Nashville, Tennessee, USA, pp.19-23 (2015).

[34] Q. Shen, Y. Xu and T. Downar, “Stability analysis of the CMFD scheme with linear prolongation,” *Annals of Nuclear Energy*, **129**, pp.298-307 (2019).

[35] J. Y. Cho, K. S. Kim, H. J. Shim, J. S. Song, C. C. Lee and H. G. Joo, “Whole core transport calculation employing hexagonal modular ray tracing and CMFD formulation,” *Journal of nuclear science and technology,* **45**(8), pp.740-751 (2008).

[36] M. Jarrett, B. Kochunas, A. Zhu and T. Downar, “Analysis of stabilization techniques for CMFD acceleration of neutron transport problems,” *Nuclear Science and Engineering,* **184**(2), pp.208-227 (2016).

[37] A. Zhu, M. Jarrett, Y. Xu, B. Kochunas, E. Larsen and T. Downar, 2016. ”An optimally diffusive Coarse Mesh Finite Difference method to accelerate neutron transport calculations,” *Annals of Nuclear Energy*, **95**, pp.116-124, 2016.

[38] D. Wang and S. Xiao, “A linear prolongation approach to stabilizing CMFD,” *Nuclear Science and Engineering*, **190**(1), pp.45-55 (2018).

[39] C. Cavarec, J.F. Perron, D. Verwaerde, and J. West, “Benchmark Calculations of Power Distribution Within Assemblies (No. NEA-NSC-DOC--94-28),” Nuclear Energy Agency (1994).

[40] K. D. Lathrop, K.D, “Ray effects in discrete ordinates equations” *Nuclear Science and Engineering*, **32**(3), pp.357-369 (1968).

[41] J. Tencer, “Ray effect mitigation through reference frame rotation,” *Journal of Heat Transfer*, **138**(11) (2016).

[42] T. Camminady, M. Frank, K. Küpper and J. Kusch, “Ray effect mitigation for the discrete ordinates method through quadrature rotation,” *Journal of Computational Physics*, **382**, pp.105-123 (2019).

[43] I. K. Abu-Shumays, “Angular quadratures for improved transport computations.,” *Transport Theory and Statistical Physics*, **30**(2-3), pp.169-204 (2001).

[44] L. L. Briggs, W. F. Miller Jr and E. E. Lewis, 1975. “Ray-effect mitigation in discrete ordinate-like angular finite element approximations in neutron transport,” *Nuclear Science and Engineering*, **57**(3), pp.205-217 (1975).

[45] J. Jung, H. Chijiwa, K. Kobayashi and H. Nishihara, “Discrete ordinate neutron transport equation equivalent to PL approximation,” *Nuclear Science and Engineering*, **49**(1), pp.1-9 (1972).

[46] K. D. Lathrop, “Remedies for ray effects,” *Nuclear Science and Engineering*, **45**(3), pp.255-268 (1971).

[47] W. F. Miller Jr and W. H. Reed, “Ray-effect mitigation methods for two-dimensional neutron transport theory,” *Nuclear Science and Engineering*, **62**(3), pp.391-411 (1977).

[48] M. A. Smith, E. E. Lewis and B. C. Na, “Benchmark on deterministic 2-D MOX fuel assembly transport calculations without spatial homogenization,” *Progress in Nuclear Energy*, **45**(2-4), pp.107-118 (2004).

[49] J. J. Hou, K. N. Ivanov, V. F. Boyarinov and P. A. Fomichenko, “OECD/NEA benchmark for time-dependent neutron transport calculations without spatial homogenization,” *Nuclear Engineering and Design*, **317**, pp. 177-189 (2017).

[50] A. Vidal-Ferràndiz et al, "CORTEX D1.3: Modelling of the neutron flux response to vibrating fuel assemblies," retrieved from https://cortex-h2020.eu/wp-content/uploads/2021/03/CORTEX_D1_3_Modelling_of_the_neutron_flux_response_to_vibrating_fuel_assemblies_V1.pdf on November 25, 2021.

[51] P. Vinai et al, "CORTEX D1.4: Development and comparison of high order solvers for reactor noise analysis" retrieved from https://cortex-h2020.eu/wp-content/uploads/2021/09/CORTEX_D1_4_Development_and_comparison_of_highorder_solvers_for_reactor_noise_analysis_V1.pdf on November 25, 2021.

[52] A. Rouchon, W. Jarrah and A. Zoia, "The new neutron noise solver of the Monte Carlo code TRIPOLI-4®," Proceedings of Mathematical and Computational Methods Applied to Nuclear Science and Engineering (M&C 2019), Portland, OR, USA, August 25–29, 2019, pp. 332-341 (2019).

[53] A. Vidal-Ferràndiz, A. Carreño, D. Ginestar, C. Demazière and G. Verdú, "A time and frequency domain analysis of the effect of vibrating fuel assemblies on the neutron noise," *Annals of Nuclear Energy*, **137**, pp. 107076 (2020).

[54] J. M. Paratte, R. Früh, U. Kasemeyer, M. A. Kalugin, W. Timm, and R. Chawla, "A benchmark on the calculation of kinetic parameters based on reactivity effect experiments in the CROCUS reactor," *Annals of Nuclear energy*, **33**(8), pp.739-748 (2006).

[55] P. Vinai et al, "CORTEX D2.5: Final validation report," retrieved from https://cortex-h2020.eu/wp-content/uploads/2021/09/CORTEX_D2_5_Final_validation_report_V1.pdf on October 16, 2021.

[56] I. Pázsit, and J. Karlsson, "On the perturbative calculation of the vibration noise by strong absorbers," *Annals of Nuclear Energy*, **24**(6), pp.449-466 (1997).

[57] A. Rouchon, and R. Sanchez, "Analysis of vibration-induced neutron noise using one-dimension noise diffusion theory," *ICAPP 2015-International Congress on Advances in Nuclear Power Plants*, Nice, France, May 2015.